

Isolated Propeller Aeroacoustics at Negative Thrust

An Experimental Study

by

Richard Rong



Isolated Propeller Aeroacoustics at Negative Thrust

An Experimental Study

by

Richard Rong

to obtain the degree of Master of Science in Aerospace Engineering
at the Delft University of Technology,
to be defended publicly on Thursday February 9, 2023 at 01:00 PM.

Student number:	4227832	
Supervisor:	Dr. ir. T. Sinnige	
Thesis committee:	Prof. Dr.-Ing. G. Eitelberg,	TU Delft
	Dr. ir. T. Sinnige,	TU Delft
	Dr. W. Yu,	TU Delft
	J. Goyal,	TU Delft

An electronic version of this thesis is available at <http://repository.tudelft.nl/>.

Acknowledgments

I want to thank the committee members for their time and effort in assessing my thesis report about isolated propeller noise at negative thrust. I would also like to express my appreciation to my daily supervisor, Tomas Sinnige, for his extensive personal and professional guidance and support throughout the research process. He has given the necessary feedback for me to successfully finalize my degree at TU Delft. I am also grateful to Roberto Merino Martinez for his assistance with signal processing and Biagio della Corte for conducting the wind tunnel experiments.

I would also like to take this opportunity to thank my family, friends, and partner for their persistent support and encouragement throughout this journey. Without them, this thesis would not have been possible. Thank you for always being there for me, believing in me, and giving me the support I needed to complete this mission.

Last but not least, I would like to acknowledge the support and resources provided by the institution, which allowed for the successful completion of this research. My time at this university was a pleasure, and I am glad I had the opportunity to meet the people I met over the last few years.

Summary

In recent years, there has been renewed interest in propeller research due to environmental concerns. It is anticipated that the number of propeller-driven aircraft will increase, driven by climate-related concerns. Propellers are known for their low-speed efficiency and coupling capabilities with electric motors. The utilization of regenerative energy during deceleration has been demonstrated to be beneficial for automobiles and has the potential to be applied to propeller-driven aircraft. This technology allows for the recharging of batteries and could increase the overall efficiency of the propulsion system by utilizing the regenerated energy in other flight maneuvers. The negative thrust mode of propellers has several additional advantages, including weight reduction, improved safety, and increased maneuverability.

The issue of propeller noise has existed for a long time, and this becomes more important when negative thrust mode emits more noise than at forward thrust, especially if negative thrust is expected to be used during landings in populated areas. When operated at negative thrust conditions, the performance of conventional propellers is suboptimal because they are designed for forward thrust. This suboptimal operation can lead to boundary layer separation, increasing broadband noise due to pressure fluctuations on the blades and making it potentially more dominant over rotational noise.

To assess the relative importance between an isolated propeller's tonal and broadband noise sources under positive and negative thrust conditions, an experimental study was conducted using a scaled propeller setup in a low-turbulence wind tunnel (LTT) at the Low-Speed Wind Tunnel Laboratory at Delft University of Technology. The research framework is divided into three main parts: the experiment for harvesting propeller data, processing, and analyzing the data.

Aeroacoustic measurements were taken using a microphone array with 58 GRAS 40PH analog microphones placed in the test section wall at a distance of 1025 mm from the rotational axis of the TUD-XPROP propeller model. An external six-component balance measured forces and moments to determine the thrust force of the propeller, and a pulse sensor was used to determine the exact rotational velocity of the shaft. For the change in positive and negative thrust, the advance ratio was varied across different wind speeds using the rotational speed at Reynolds numbers ranging from $Re_c^{0.7R} = 0.8 \cdot 10^5$ to $Re_c^{0.7R} = 1.9 \cdot 10^5$.

By varying the rotational speed to vary the advance ratio, the tests at positive thrust have higher tip Mach numbers than tests at negative thrust. They range from $M = 0.16$ to $M = 0.35$. These values are significantly lower than actual flight conditions where the Mach number reaches up to 0.8 or higher. This should be considered when the results are interpreted. In the field of aeroacoustics, the local Mach number is regarded as the most crucial similarity parameter. When scaling the tip Mach number up to actual flight conditions, the power of the noise will increase due to the increased loading. This means the noise measured at negative thrust will increase more than at positive thrust when scaled to the same tip Mach number.

Signal processing methods were used to analyze the data and quantify tonal and broadband noise sources. The fast Fourier transformation (FFT) converts a signal from the time domain to the frequency domain. The frequency domain is used to gain insight into the signal from the spectral point of view instead of the time domain. The frequency spectra show a significant increase in the noise levels at high frequencies. The blade element momentum (BEM) analysis was used to determine the presence of laminar separation bubbles (LSB), as they are likely to occur at low Reynolds numbers. An LSB is known to generate high-frequency noise. In real-flight conditions (at high Reynolds numbers), the LSB would not occur. Therefore, the data that is affected by the LSB should not be considered for real-flight conditions when analyzing the data.

Phase averaging is a processing technique that amplifies the rotational noise with respect to other noise sources. This was used to isolate the tonal component of the propeller noise in the data. The phase averaging results were unsatisfactory due to interfering noise sources of the wind tunnel and the motor and drive train. To minimize the unwanted noise sources, an inverse beamforming technique was applied. Due to the beamforming resolution being dependent on the wavelength of the noise sources, beamforming had more effect on the test data at positive thrust. The blade passing frequencies at negative thrust were lower than at positive thrust. Therefore, the beamforming resolution was higher for the data at positive thrust conditions.

A high-pass filter was implemented on the beamformed data to eliminate the predominant low-frequency noise sources from the wind tunnel. Additionally, a low-pass filter was applied to ignore the impact of the LSB on the sound level measurements in the high-frequency region. The isolated tonal and broadband components were obtained by subtracting the spectra of the wind tunnel and motor noise from the propeller-on measurement data. The broadband noise levels were deducted from the tonal components to calculate each component's overall sound pressure level. This calculation was performed through a logarithmic summation of the spectrum.

From the results of the isolated overall sound pressure level of the broadband propeller noise component, it can be concluded that the broadband noise component of the propeller significantly increased at negative thrust mode compared to the positive thrust mode. The diagnostic BEM analysis has shown that the blades at negative thrust mode show fully separated boundary layers. This separation causes turbulence on the blades and emits a higher level of broadband noise due to random pressure fluctuations. The tonal propeller components were often masked by interference from wind tunnel and motor noise and could not be isolated using the before-mentioned signal processing methods.

Building upon the work and discussion presented in this thesis, there are some recommendations for future work that could enhance understanding of the negative thrust regime of propellers. To maintain similarity in a model propeller, keeping a constant tip Mach number and advance ratio is recommended, which can be done by adjusting blade pitch for positive and negative thrust modes. This way, the beamforming resolution at the angular frequency will be equal for all test conditions. Additionally, motor noise was found to vary with speed, but keeping a constant rotational speed would reduce this variability.

The studies on propeller noise have historically focused on the prediction of tonal noise components, frequently disregarding the contribution of broadband propeller noise. However, the results of the present experiment suggest that broadband noise assumes greater prominence at negative thrust conditions. Therefore, it is necessary to include propeller noise at negative thrust in future experiments. It is essential to conduct further experimental studies to evaluate the relative importance of tonal and broadband noise components in this regime as part of the effort to make aviation climate neutral by 2050.

Contents

Acknowledgments	iii
Summary	v
List of Tables	ix
List of Figures	xi
Nomenclature	xv
I Introduction	1
1 Introduction	3
1.1 Thesis Objective	4
1.2 Thesis Question	4
1.3 Thesis Outline	5
II Background	7
2 Propellers at Negative Thrust Condition	9
2.1 Propeller Characteristics	9
2.1.1 Vortices and Swirl	9
2.2 Potential Use of Negative Thrust Condition	10
2.3 Propeller Aerodynamics at Negative Thrust.	11
3 Propeller Noise Characteristics	15
3.1 Fundamental Sound Sources	15
3.1.1 Monopole	16
3.1.2 Dipole	16
3.1.3 Quadrupole	16
3.2 Rotational Noise	17
3.2.1 Loading Noise	18
3.2.2 Thickness Noise	18
3.3 Broadband Noise	19
3.4 Directional Propeller Noise.	20
3.5 Propagation Effects.	20
3.5.1 Noise Propagation	21
3.5.2 Atmospheric Attenuation	21
3.5.3 Frequency and Amplitude Modulation	22
3.6 Propeller Aeroacoustics at Negative Thrust.	23
4 Aeroacoustic Experiments on Propellers	25
4.1 Similarity and Scaling Parameters	25
4.1.1 Mach number and Reynolds number	25
4.1.2 Dimensional Analysis.	27
4.2 Effect of Propeller Thrust in a Wind Tunnel	27
III Methodology	29
5 Experimental Setup	31
5.1 Wind-Tunnel Facility	31
5.2 Propeller Model and Geometry	32

5.3	Measurement Techniques	32
5.3.1	Six-Component External Balance	32
5.3.2	Microphone Specifications and Placement	33
5.4	Test Conditions	34
5.4.1	Similarity of Test Conditions	37
6	Data Processing	39
6.1	Noise Signal in Time Domain	40
6.2	Microphone Sensitivity and Calibration	41
6.3	Angular Frequency	42
6.4	Fourier Transformation	42
6.4.1	Fast Fourier Transform	43
6.4.2	Aliasing, Picket Fence, and Scallop Loss	43
6.4.3	Spectral Leakage, Window Functions, and Overlap	43
6.5	Frequency Analysis	44
6.6	Blade Element Momentum Analysis	46
6.7	Phase Averaging	47
6.8	Beamforming	48
6.9	Broadband and Tonal Components	50
IV	Results and Discussion	51
7	Results and Discussion	53
7.1	Thrust Coefficient	53
7.2	Frequency Spectra	54
7.3	Blade Element Momentum Analysis	56
7.4	Phase Averaged Noise Levels	57
7.5	Noise Data from Inverse Beamforming	58
7.6	Overall Sound Pressure Levels	62
V	Conclusion and Recommendations	65
8	Conclusion	67
9	Recommendations	69
	Bibliography	71
VI	Appendices	75
A	Frequency Spectrum	77
A.1	Frequency Spectra run 1	77
A.2	Frequency Spectra run 2	79
B	Phase Average	83
C	Beamforming	87

List of Tables

5.1	Test Matrix for Run 1.	36
5.2	Test Matrix for Run 2.	36
5.3	Test Matrix for Run 3.	36
5.4	Test Matrix for Run 4.	36
5.5	Test Matrix for Run 5.	36
7.1	Test matrix of the selected test conditions derived from Table 5.1.	53

List of Figures

2.1	Typical propeller efficiency curves as a function of advance ratio [14].	9
2.2	Effect of negative propeller thrust on braking distance on a landing run [37].	10
2.3	Brake weights of disc and propeller [24].	11
2.4	Velocity triangles at a propeller blade section in positive thrust condition (a) and negative thrust condition (b) [63].	12
2.5	Comparison of forwarding and reverse thrust, adapted from [60].	13
3.1	Elementary sources of sound [43].	16
3.2	Different types of aerodynamic noise [43].	17
3.3	Schematic diagram of the steady and oscillating components of the impulses by a single propeller blade [55].	17
3.4	Steady and oscillating components of the impulses by two propeller blades [55].	17
3.5	Effect of the number of blades at different tip speeds on noise levels for constant power [55].	18
3.6	Aerodynamic loads acting on propeller blades [1].	19
3.7	Theoretical noise patterns for rotors, propellers, and fans [43].	20
3.8	Atmospheric conditions affecting sound rays [44].	21
3.9	Spectrogram of the noise emitted by a propeller-driven aircraft [61].	22
4.1	Effect of Reynolds number on propeller efficiency for different advance ratios [62].	26
5.1	Drawing of the Low-Speed Wind Tunnel Laboratory at Delft University of Technology.	32
5.2	Schematic drawing of the side view (left) and the front view (right) of the model setup and microphone positions.	33
5.3	Picture of the model setup and the microphone array on the wall and floor.	33
5.4	Microphone wall and floor array positions with its number, seen from behind the wall.	34
5.5	Thrust coefficient curves of the TUD-XPROP for blade pitch angles $\beta = 15^\circ$ and $\beta = 30^\circ$	35
5.6	Similarity parameters tip Mach number and Reynolds number for thrust setting where $V = 30$ m/s.	38
6.1	A flowchart presenting an overview of the various signal processing methods employed, along with their inputs and outputs.	39
6.2	Time signal of microphone 1 and its root-mean-square of run 1 (left) and run 2 (right).	40
6.3	Spectrograms of average signals for run 1 (a), close-up of run 1 (b), run 2 (c), and a close-up of run 2 (d) over 30 seconds.	40
6.4	Microphone calibration factors for a 1 kHz tone at 94 dB.	41
6.5	Comparison between raw data and calibrated data in the frequency domain for run 1 test 2 mic 1.	41
6.6	Example of a 1P signal with its located peaks (left) and the angular frequency (right).	42
6.7	Perspectives of the time domain and the frequency domain [57].	42
6.8	Spectral leakage effect where f_{in} equals an integer multiple of δf (left) and f_{in} does not equal an integer multiple of Δf (right).	43
6.9	Hamming window applied on a signal with 0% window overlap [39].	44
6.10	Example averages of spectra for wall and floor microphones for run 1 test 2.	45
6.11	Frequency spectra for positive, zero and negative thrust for $V = 30$ m/s, averaged over all microphones ($\Delta f = 1$ Hz).	45
6.12	XFOIL screenshot of a C_p distribution for viscous (solid line) and inviscid (dashed line) analysis of the TUD-XPROP blade simulated in the conditions of run 2 test 2 at 0.4 r/R.	47

6.13 XFOIL screenshot of a C_p distribution for viscous (solid line) and inviscid (dashed line) analysis of the TUD-XPROP blade simulated in the conditions of run 1 test 8 at 0.4 r/R.	47
6.14 Phase averaged data of all microphones for one test case with one microphone signal highlighted and its pressure RMS value.	48
6.15 Beamforming effect on the target signal (a) and the interfering signal (b) [42].	49
6.16 Non-beamformed and beamformed frequency spectrum for the positive thrust regime for $V = 30$ m/s ($\Delta f = 1$ Hz).	49
7.1 Normalized thrust coefficient derived from the six-component external balance.	54
7.2 Normalized frequency spectra for $V = 30$ m/s ($\Delta f = 1$ Hz).	55
7.3 Frequency spectra ($\Delta f = 1$ Hz) of motor measurements (top), and normalized spectrum (bottom).	56
7.4 Pressure distribution for different thrust settings and blade sections where $V = 30$ m/s.	57
7.5 Phase average signal of microphone no. 1 for each regime for $V = 30$ m/s.	58
7.6 Interpolated contour plot of phase-averaged sound pressure levels of every microphone for $V = 30$ m/s with color bars showing a 5 dB range.	58
7.7 Beamforming maps for $V = 30$ m/s with the ROI indicated with the dashed line for frequencies nearest to the first, fifth, and tenth BPF at both thrust regimes.	59
7.8 Different situations at each BPF of the total measurements with respect to the motor noise and wind tunnel noise.	60
7.9 12 BPF harmonics of beamformed spectra for positive, zero and negative thrust ($\Delta f = 1$ Hz).	61
7.10 Resulting broadband and tonal propeller noise components at each regime after subtraction of wind tunnel noise and motor noise for $V = 30$ m/s ($\Delta f = 16$ Hz).	62
7.11 Overall sound pressure levels of different components and helical Mach number for different thrust settings.	63
A.1 Frequency spectrum of run 1 test 2, wind tunnel noise, motor noise, and background noise averaged over all microphones ($\Delta f = 1$ Hz).	77
A.2 Frequency spectrum of run 1 test 3, wind tunnel noise, motor noise, and background noise averaged over all microphones ($\Delta f = 1$ Hz).	77
A.3 Frequency spectrum of run 1 test 4, wind tunnel noise, motor noise, and background noise averaged over all microphones ($\Delta f = 1$ Hz).	77
A.4 Frequency spectrum of run 1 test 5, wind tunnel noise, motor noise, and background noise averaged over all microphones ($\Delta f = 1$ Hz).	78
A.5 Frequency spectrum of run 1 test 6, wind tunnel noise, motor noise, and background noise averaged over all microphones ($\Delta f = 1$ Hz).	78
A.6 Frequency spectrum of run 1 test 7, wind tunnel noise, motor noise, and background noise averaged over all microphones ($\Delta f = 1$ Hz).	78
A.7 Frequency spectrum of run 1 test 8, wind tunnel noise, motor noise, and background noise averaged over all microphones ($\Delta f = 1$ Hz).	78
A.8 Frequency spectrum of run 1 test 9, wind tunnel noise, motor noise, and background noise averaged over all microphones ($\Delta f = 1$ Hz).	79
A.9 Frequency spectrum of run 1 test 10, wind tunnel noise, motor noise, and background noise averaged over all microphones ($\Delta f = 1$ Hz).	79
A.10 Frequency spectrum of run 2 test 1, wind tunnel noise, motor noise, and background noise averaged over all microphones ($\Delta f = 1$ Hz).	79
A.11 Frequency spectrum of run 2 test 2, wind tunnel noise, motor noise, and background noise averaged over all microphones ($\Delta f = 1$ Hz).	79
A.12 Frequency spectrum of run 2 test 3, wind tunnel noise, motor noise, and background noise averaged over all microphones ($\Delta f = 1$ Hz).	80
A.13 Frequency spectrum of run 2 test 4, wind tunnel noise, motor noise, and background noise averaged over all microphones ($\Delta f = 1$ Hz).	80
A.14 Frequency spectrum of run 2 test 5, wind tunnel noise, motor noise, and background noise averaged over all microphones ($\Delta f = 1$ Hz).	80

A.15	Frequency spectrum of run 2 test 6, wind tunnel noise, motor noise, and background noise averaged over all microphones ($\Delta f = 1$ Hz).	80
A.16	Frequency spectrum of run 2 test 7, wind tunnel noise, motor noise, and background noise averaged over all microphones ($\Delta f = 1$ Hz).	81
A.17	Frequency spectrum of run 2 test 8, wind tunnel noise, motor noise, and background noise averaged over all microphones ($\Delta f = 1$ Hz).	81
A.18	Frequency spectrum of run 2 test 9, wind tunnel noise, motor noise, and background noise averaged over all microphones ($\Delta f = 1$ Hz).	81
A.19	Frequency spectrum of run 2 test 10, wind tunnel noise, motor noise, and background noise averaged over all microphones ($\Delta f = 1$ Hz).	81
B.1	Phase averaged sound pressure levels for run 1.	84
B.2	Phase averaged sound pressure levels for run 2.	85
C.1	12 BPF harmonics of beamformed spectra for each test case of run 1 ($\Delta f = 1$ Hz). . . .	87
C.2	12 BPF harmonics of beamformed spectra for each test case of run 2 ($\Delta f = 1$ Hz). . . .	88
C.3	Resulting broadband and tonal propeller noise components after subtraction of wind tunnel noise and motor noise for run 1 ($\Delta f = 16$ Hz).	89
C.4	Resulting broadband and tonal propeller noise components after subtraction of wind tunnel noise and motor noise for run 2 ($\Delta f = 16$ Hz).	90

Nomenclature

Acronyms

BPF	blade passing frequency
FFT	fast Fourier transform
IBF	inverse beamforming
LSB	laminar separation bubble
LTT	low-turbulence tunnel
MATLAB	MATrix LABoratory - a numeric computing environment
NG	noise gain
OSPL	overall sound pressure level
RMS	root mean square
ROI	region of integration
rpm	revolutions per minute
rps	revolutions per second
SPL	sound pressure level
TF	transfer factor

Greek Symbols

α	angle of attack	[°]
B	pitch angle	[°]
Δf	frequency resolution	[Hz]
λ	wavelength	[m]
μ	efficiency	[-]
μ	viscosity coefficient	[-]
ω	angular velocity	[Hz]
Π	thrust-specific sound pressure level	[-]
ρ	air density	[kg/m ³]
θ	angle	[°]

Roman Symbols

B	number of blades	[-]
C	coefficient	[-]
c	speed of sound	[m/s]

D	propeller diameter	[<i>m</i>]
f	frequency	[<i>Hz</i>]
J	advance ratio	[–]
L	length	[<i>m</i>]
M	Mach number	[–]
N	number of data points	[–]
n	rotational speed	[<i>Hz</i>]
P	power	[<i>W</i>]
p	pressure	[<i>Pa</i>]
R	propeller radius	[<i>m</i>]
r	radius	[<i>m</i>]
Re	Reynolds number	[–]
S	surface area	[<i>m</i> ²]
St	Strouhal number	[–]
T	thrust	[<i>N</i>]
t	time	[<i>s</i>]
V	flow velocity	[<i>m/s</i>]
W	acoustic power	[<i>W</i>]

Subscripts

0	reference
1P	pulse signal
∞	freestream condition
c	normalized coefficient
d	drag
eff	effective
h	helical
L	lift
l	local
P	power
q	torque
r	rotational
T	thrust
wt	wind tunnel



Introduction

1

Introduction

In aeronautics, a propeller consists of multiple rotating wings that convert rotational power into propulsive power. The earliest use of blades to generate lift or thrust dates back to a Chinese children's toy known as the 'bamboo dragonflies', which originated in the fourth century AD [33]. This toy, consisting of feathers (blades) attached to a stick that was rolled between the hands on a vertical axis, demonstrated the principles of aerodynamic lift and thrust. The resulting rotation generated an aerodynamic lift, allowing the toy to take off when released. Inspired by the same concept, the Wright brothers used propellers based on the same principles to power the Wright flyer for the first controlled, powered, heavier-than-air flight in 1903 [4]. The successful powered flight of the Wright flyer significantly reduced skepticism surrounding the feasibility of manned, heavier-than-air flights. The Wright brothers had the advantage of applying their knowledge of wings to the development of the modern aircraft propeller, unlike earlier engineers such as H. Giffard in 1852 [5], C. Ader [21] in 1890, and F. von Zeppelin [22]. These earlier engineers could not achieve the same level of success as the Wright brothers in pioneering propellers in aviation.

For multiple decades, propellers were an extensively used method of propulsion in aviation [38]. The propeller has undergone slight modifications in terms of material, pitch, weight, and blade shapes, but the noise generation mechanism has not changed throughout time [38]. The growth of development related to aviation around 1905 was followed by World War I, which showed that aircraft could be more beneficial than most could imagine [6]. The world's first jet-powered aircraft flight was in 1939, led by H. von Ohain [13]. A German aircraft manufacturing company, Heinkel Flugzeugwerke, helped Ohain develop the plane as they focused on state-of-the-art technology for high-speed aircraft [51].

World War II illustrated that jet engines were in the vanguard of aviation development. At this time, speed was the driving element in the development of aviation. Aircraft flew higher and faster over time, taking the penalty for fuel consumption for granted. Due to the introduction of turbojets and turboprops, the development of propellers decelerated. Both have a wide range of freestream Mach numbers and are, therefore, still the primary propulsion method in aviation. However, propeller propulsion regained interest after about twenty years [66], due to the first and second oil crises in the 1970s. As oil prices inclined, previously accepted high fuel consumption in exchange for speed became an issue. New aircraft designs promised significant improvements in fuel consumption and operational costs. High-speed turboprops would also have improved performance at high cruise speed compared to a high bypass ratio turbofan [66]. However, the disadvantage was that the design involved unshrouded propellers that radiate higher noise levels [11], while the aversion from the public against the noise created by aircraft was already increasing over the years [43]. The more the commercial activity of aviation in heavily populated areas increased, the more the importance grew of gaining knowledge about aircraft noise sources [43]. The complexity of the noise radiation of rotational components makes the study scientifically challenging and socially relevant.

Regenerative energy utilization during deceleration has been demonstrated to be beneficial for automobiles. This technology, which allows for the recharging of batteries, can also be applied to propeller-

driven aircraft [47]. The regenerated energy could be utilized in other flight maneuvers, thereby increasing the overall efficiency of the propulsion system. However, the negative thrust condition is sub-optimal for conventional propeller blades. This can result in various negative effects, such as boundary layer separation, increased drag forces, and reduced thrust. These effects also impact the aeroacoustic performance, as boundary layer separation can lead to broadband noise generation. This is particularly disadvantageous as the regenerative mode is expected to be utilized in densely populated areas [27].

1.1. Thesis Objective

Assessing the relative importance of noise sources for isolated propellers at negative thrust conditions is of significant interest. This is because if the dominant noise source differs from that of a propeller in the forward thrust regime, it would be valuable to understand the reasons behind this shift in dominance. This knowledge could be utilized to reduce propeller noise in this regime. The collected test data can also serve as a means of validating numerical predictions [27]. Implementing negative thrust in combination with electrical motors for propellers presents opportunities to save and regenerate electricity for future aircraft. This would increase the practicality of commercial electric aircraft and accelerate the adoption of electrified aircraft. This research is a part of FUTPRINT50. FUTPRINT50 is an international cooperation funded by the EU [2]. The FUTPRINT50 project aims to make aviation climate-neutral by 2050, and understanding the noise sources at negative thrust conditions is a step toward achieving this goal. Therefore, the research objective of this thesis is as follows:

”To assess the relative importance of an isolated propeller’s tonal and broadband noise sources under positive and negative thrust conditions through an experimental approach. This involves conducting an experimental study on a propeller set up in a wind tunnel and applying various signal processing techniques to analyze the data.”

Conducting a wind tunnel test represents a valuable addition to the existing literature on this topic. Wind tunnel testing allows for the collection of physical data and the ability to test a wide range of variations of multiple variables within a relatively short time, compared to numerical methods. It is unclear which noise type or source is dominant at negative thrust conditions. Therefore, it is necessary to consider linear noise types and non-linear ones, such as broadband noise. Non-linear calculations require significantly more computational resources and are not practical for evaluating large variations. Additionally, the data obtained from wind tunnel testing can validate this regime’s numerical methods.

1.2. Thesis Question

The study of propeller noise at negative thrust conditions has not been thoroughly investigated. A literature review reveals that negative thrust has been found to increase aircraft safety and braking efficiency and reduce maintenance and operational expenses. However, there are indications that the dominant sound sources may differ from the forward thrust regime for conventional propellers due to the presence of separated boundary layers [27]. To date, proper noise measurements of propellers under this condition have not been collected, even though experimental data is essential for validating numerical calculations used to predict noise, which is currently only validated in the conventional regime. Therefore, the main research question for this thesis is:

”How do propeller noise sources vary in relation to positive and negative thrust settings for an existing isolated forward thrust propeller?”

It is anticipated that the number of propeller-driven aircraft will increase in the future. This increase is driven by climate-related concerns, such as sustainability, the favorable coupling capabilities of propellers with electric motors, and their high fuel efficiency. To address the critical elements of the main research question, several sub-questions have been formulated to define the research strategy further. These include:

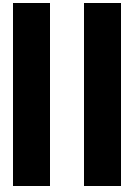
1. What relevant test conditions impact the variation of tonal and broadband noise due to the thrust setting of isolated propellers?

2. How can the similarity with real-life conditions be ensured during scaled aeroacoustic experiments?
3. What signal processing methods can be used to decompose and quantify different propeller noise sources?

This research can be divided into three main parts: the experiment for harvesting relevant propeller data, the processing, and the analysis of the data.

1.3. Thesis Outline

This thesis is divided into nine chapters. In Chapter 1, the topic of the thesis is introduced, and the problem statement, objective, and research questions are presented. Chapters 2 to 4 provide background information on the subjects discussed in the thesis, including general theories on propellers and their aeroacoustic characteristics, different types of noise, and the regenerative mode of a propeller. These chapters also provide information on experimental studies on the aeroacoustics of propellers. Chapters 5 and 6 describe the facility and tools used for the experiments and the test conditions and methods for processing the results. The results of the experiments are analyzed and discussed in chapter 7. Finally, chapters 8 and 9 contain the conclusions drawn from the findings and recommendations for future research.



Background

2

Propellers at Negative Thrust Condition

2.1. Propeller Characteristics

Propellers have been a method of propulsion for aircraft since the first flight in the world. The rotational blades attached to an axle are known from other vehicles or systems, such as boats, fans, and pumps. However, this section will discuss only aircraft propellers (also called airscrews).

Most propellers are optimized to generate forward thrust to drive the aircraft. A blade uses its rotational velocity combined with its freestream velocity the same way a wing uses the free stream velocity. The effective speed will develop a low-pressure area on the front side of the blade and a high-pressure area on the rear side. The resultant load of the pressure distribution has a thrust and torque component or a lift and drag component. As we have read in the introduction, propellers induce a small increment in velocity for a large mass of air, making them efficient propulsion methods. The efficiency drops at high Mach numbers (see Figure 2.1). Therefore, conventional propellers are more suitable for operations at lower Mach numbers [38]. The following sections will explain some essential propeller characteristics involved in studying propeller noise effects.

2.1.1. Vortices and Swirl

Just like wings, propeller blades also induce vortices. This is an effect of a lifting surface and is called lift-induced vortices. Due to the created pressure distribution, high pressure occurs on one side of the blade, while low pressure occurs on the other. A result of this is that the airflow rolls up around the blade where the pressure difference meets. This phenomenon appears at the end of the spanwise direction of the blades, the trailing edge, and the tip at the end of the chordwise direction of the blades. Different methods exist to decrease the appearance of vortices, as they are related to induced drag.

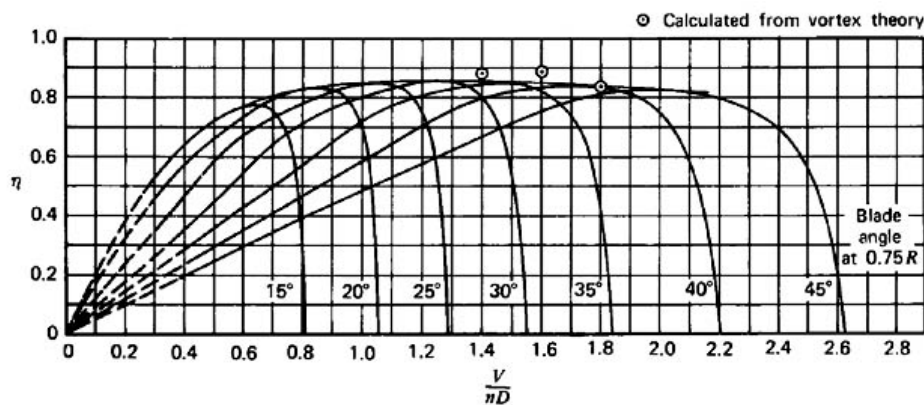


Figure 2.1: Typical propeller efficiency curves as a function of advance ratio [14].

Swirl behind a propeller contributes to the loss of efficiency of a propeller, as the energy used to create this swirl does not contribute to the thrust [38]. Sometimes, counter-rotating propellers are applied to reduce swirl. This is a second propeller just behind the first one, rotating in the opposite direction. The idea behind this method is that the second propeller cancels out the swirl created by the first propeller. By applying this method, the efficiency can be increased up to 10% [48].

2.2. Potential Use of Negative Thrust Condition

It has been proven beneficial for cars to regenerate energy during deceleration. The same technology used by cars to recharge batteries can also be applied to propeller aircraft [47]. The regenerated energy provided by this technology can then be used in other flight maneuvers. Regaining energy also reduces the net energy consumption of the flight. The energy saved can perhaps extend the possibilities for emergency landings. The technology to recharge batteries, however, applies to electric propulsion methods. Batteries still have low energy densities compared to kerosene or hydrogen. The advance of regenerating propellers will not be enough to close the gap. Although a vast amount of studies have been done on electric propulsion in aviation in the last decades [50], the first all-electric commercial aircraft took off recently in 2019 [20].

Another advantage for propeller-driven aircraft to operate at reverse thrust conditions is the possibility of aerodynamic braking. Aerodynamic braking has numerous benefits compared to conventional aerodynamic or mechanical braking systems. The need for extra braking capacity becomes more significant as the take-off weight rises through time, and the mechanism used to propel the propeller system has already conveniently been designed to withstand large thrust forces. An additional braking system could increase the overall braking power of the aircraft.

Several experimental studies show that propellers can serve as very powerful brakes [24, 35, 37]. One showed that propellers could generate more braking power with a lower terminal velocity compared to traditional dive flaps [37]. Figure 2.2, based on the same experimental study, shows a 32 percent saving in the length of the landing runway because of the use of negative propeller thrust. Another experimental study resulted in more than 55% reduction of stopping distance with two propellers at negative thrust on a B32 and a nearly 60% reduction with four propellers [24]. The usefulness of propeller braking is intensified on wet or icy runways, where disk brakes have less braking capacity, while aerodynamic propeller braking performs equally without loss of effectiveness. Other air brakes, such as spoilers, increase aerodynamic drag for braking purposes. However, these systems lose effectiveness at lower speeds, e.g. during landing, and cause severe buffeting [37].

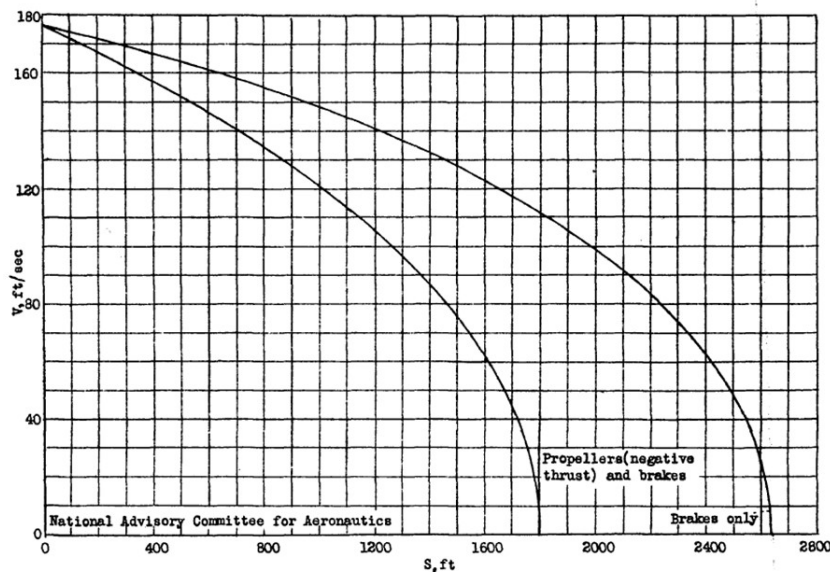


Figure 2.2: Effect of negative propeller thrust on braking distance on a landing run [37].

Propeller braking can provide additional safety for an aircraft by providing a different braking mechanism in case of a mechanical failure of the disc brakes or wet and icy runways. Extra braking capacity also allows for the reduction of disc brake weight. The application of reverse thrust on a 45,000 kg B32 aircraft led to a weight reduction of nearly 200 kg [24]. Propeller brakes can also significantly affect the tire and brake wear, wheel size, maintenance, and the length of landing run [24, 35, 60]. Shorter landing runs will become feasible as the disc and propeller brakes can perform simultaneously. This dramatically increases the number of possible emergency landing locations.

Negative propeller thrust is a very suitable system to use for braking purposes, with only a little additional weight or systems. Adding aerodynamic braking to the aircraft's braking capacity can save weight in the landing gear and increase safety and comfort with lower maintenance time and cost. In the experimental study on a B32, the additional weight of the implementation of reverse thrust was much smaller than the weight savings for smaller disc brakes, see Figure 2.3 [24]. Additionally, this will lead to a reduction in brake wear in the tires and discs. Thus, less maintenance is required.

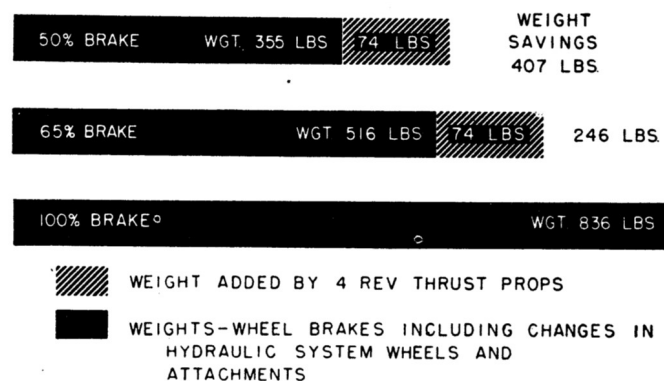


Figure 2.3: Brake weights of disc and propeller [24].

The additional thrust mode could also offer possibilities to improve control surface effectiveness, although strong reverse thrust can create turbulence over control surfaces as well [24]. For example, opportunities arise for additional controllability when different advance ratios are applied to distributed propellers. The aerodynamic behavior affected by the disturbed lift distribution is something that has to be taken into account. The addition of negative thrust could also be used for taxiing backward. This is interesting as it could decrease operating costs while the weight penalty is minor for thrust reversal possibilities [66].

2.3. Propeller Aerodynamics at Negative Thrust

The aerodynamics of the propeller change as the operating conditions change. Propellers are optimized to generate thrust forward and have different aerodynamic characteristics at negative thrust conditions. This condition allows regenerating energy, for example, during descent. In the conventional propulsive mode or at positive thrust condition, the velocity triangles and loads are shown in Figure 2.4a. The rotational direction of the blades is to the right, and the free-stream velocity points downwards in the figure. To generate negative thrust, the angle of attack has to be reduced to be negative [63]. The angle of attack is established by the blade pitch angle β and the ratio of the free stream velocity V_∞ and the rotational velocity. This ratio of the two velocity components is usually expressed as the advance ratio J , see Equation 2.1. A negative angle of attack can be achieved for a fixed blade pitch by increasing the advance ratio. A symmetric airfoil without camber is considered a simplification for the explanation. For an asymmetric airfoil, a negative angle of attack would not necessarily result in a negative thrust. A larger negative angle would eventually lead to a negative thrust coefficient with a negative thrust. The advance ratio J is increased by increasing free-stream velocity V_∞ or decreasing rotational speed n . Once the advance ratio is increased until the effective velocity V_{eff} has a negative angle α with respect to the chord line, the pressure distribution has changed with negative thrust and negative torque due to negative lift forces, as a result (see Figure 2.4b). This operation mode allows for restoring energy.

The propellers in this condition can be compared to a wind turbine. Instead of using the wind to harvest energy, the aircraft's kinetic and potential energy are used.

$$J = \frac{V_\infty}{nD} \quad (2.1)$$

The negative thrust condition is a sub-optimal condition for conventional propeller blades. Less optimized blades could result in several effects, such as turbulence and separation of the boundary layer or increased drag forces and lower thrust. These effects will also affect the aeroacoustic performance, as separation might induce more broadband noise. An increase in noise generation would be disadvantageous, as the regenerative mode is expected to be used in densely populated areas.

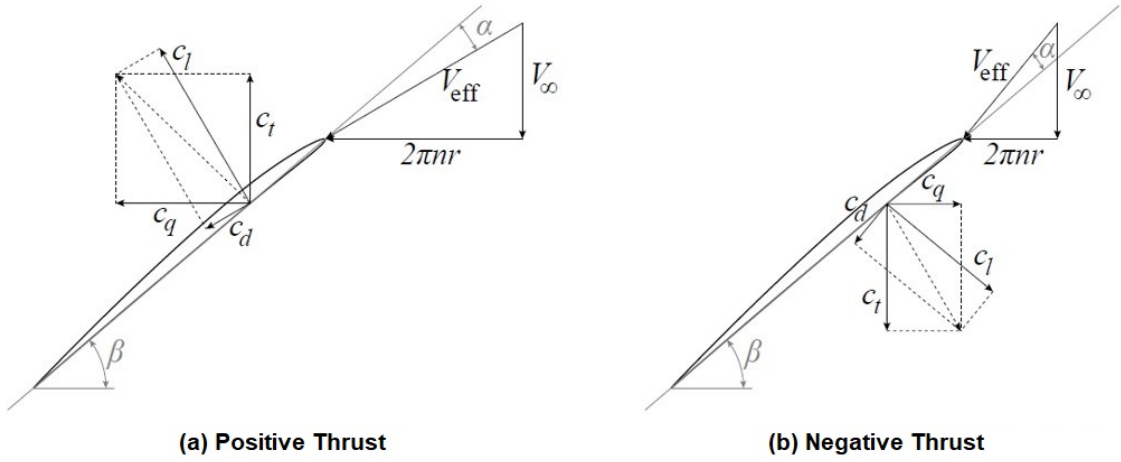


Figure 2.4: Velocity triangles at a propeller blade section in positive thrust condition (a) and negative thrust condition (b) [63].

The thrust coefficient can describe the performance characteristics of a propeller (Equation 2.2), power coefficient (Equation 2.3), and propeller efficiency (Equation 2.4) [62].

$$C_T = \frac{T}{\rho_\infty n^2 D^4} \quad (2.2)$$

$$C_P = \frac{P}{\rho_\infty n^3 D^5} \quad (2.3)$$

$$\eta = J \frac{C_T}{C_P} \quad (2.4)$$

The advance ratio is commonly used as an independent parameter to determine propellers' performance, which is often expressed in nondimensionalized parameters. The sub-optimal performance of the propeller design at reverse thrust becomes clear when forward thrust and reverse thrust are compared to airspeed [60]. As shown in Figure 2.5, thrust decreases with increasing velocity for forwarding thrust, and thrust increases with increasing velocity for reverse thrust. Breaking performances of reverse thrust conditions get as near as approximately 83% of forwarding thrust at zero velocity.

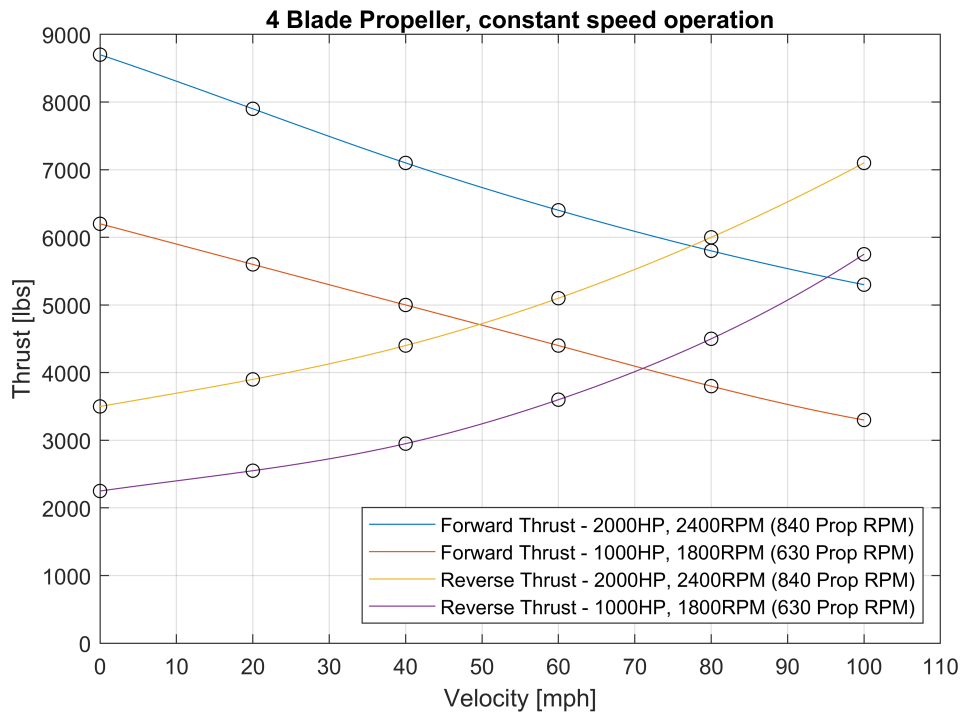


Figure 2.5: Comparison of forwarding and reverse thrust, adapted from [60].

3

Propeller Noise Characteristics

The aerodynamic noise of propellers has always been the primary noise source of propeller-driven aircraft [55]. Aerodynamic noise can be described as radiation of sound caused by the relative motion between airflow and a solid body, which would be the blades of a propeller [43]. This section will discuss the different sound sources, generally known as fundamental sound sources. More propeller specifically, noise is usually categorized into two types: tonal noise and broadband noise [17, 43]. The relative importance depends strongly on the design of the blades and the operating conditions [38].

3.1. Fundamental Sound Sources

Fundamental sound sources are divided into monopoles, dipoles, and quadrupoles. These are the elementary solutions of the equations of motion from the classical acoustic theory of minor disturbances to gas at rest [17, 43]. Any of the three sound sources can be either steady or unsteady and be responsible for harmonic or random noise radiation [17]. The latter two will be discussed in the following sections. Gutin [30] was one of the first ones to study noise analytically [17]. Garrick and Watkins (1953) have made much progress in predicting the behavior of the acoustic field [25]. However, Lighthill [46] formed the basis of the currently used methods for propeller noise prediction [18]. The basic equation for sound propagation is shown in Equation 3.1, where pressure equals the non-homogeneous wave equation. The estimations have a reasonable correlation with empirical data at lower harmonics. The predictions tend to underestimate [17] at higher harmonics.

$$\frac{\delta^2 p}{\delta t^2} - c^2 \frac{\delta^2 p}{\delta x_i^2} = \frac{\delta Q}{\delta t} - \frac{\delta F_i}{\delta x_i} + \frac{\delta^2 T_{ij}}{\delta x_i \delta x_j} \quad (3.1)$$

The terms on the left side are familiar from the wave equation, with p being the pressure perturbation. c is the speed of sound and x_i the displacement coordinates. The right side of the equation consists of three terms that resemble the monopole, dipole, and quadrupole sources. Most literature refers to the monopole and the quadrupole sources as negligible source types [17]. Multiple experiments show that quadrupole sources have an insignificant contribution to the overall noise at low tip Mach number.

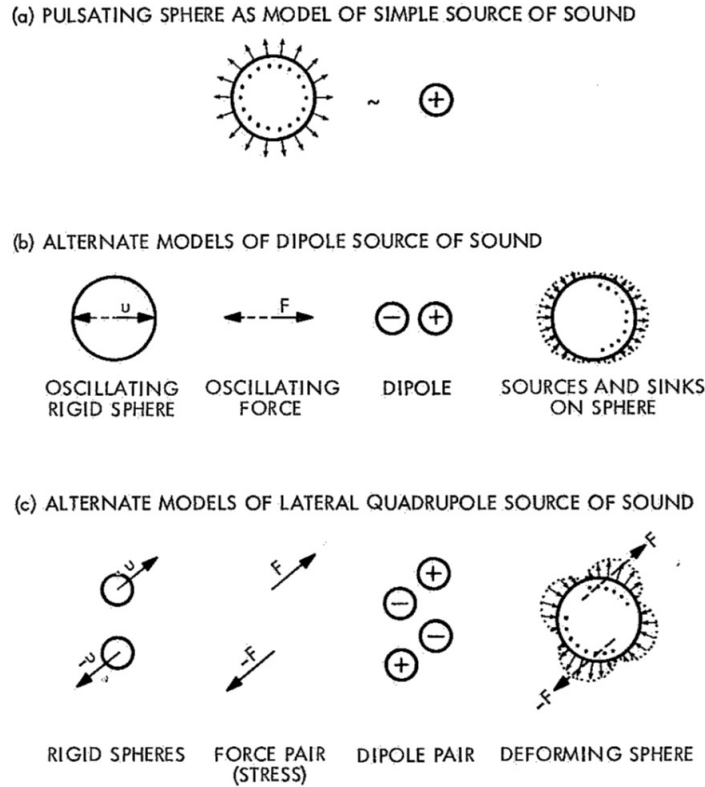


Figure 3.1: Elementary sources of sound [43].

3.1.1. Monopole

The monopole is the most straightforward type of the three, which can be seen as a pulsating sphere, alternately contracting and expanding, shown in Figure 3.1a. This simple source continues radiating sound waves as a point source in all directions. Only a point of outflow exists from which the flow can vary. An unboxed speaker is an excellent example of a monopole sound source.

3.1.2. Dipole

The second sound source is called a dipole. A dipole does not only vary in magnitude but in direction as well. It contains a momentum resulting in an oscillating sphere as shown in Figure 3.1b. An example of a dipole propeller sound source is loading noise. This will be discussed in detail in the following sections. Dipole sources are usually the essential sources at subsonic conditions and low frequencies [17]. Most studies on propeller noise focused on this sound source because of its predominance characteristic. The importance of this sound source has been acknowledged since the work of Gutin [17].

3.1.3. Quadrupole

The final type of noise source can be seen as a pair of dipoles, with each dipole having opposite forces as shown in Figure 3.1c [43]. This results in a quadrupole depicted as a sphere deforming in four directions. Quadrupole sound sources cause nonlinear effects and nonlinear propagation. This non-linearity results in long computing times when prediction techniques are used [53]. Also, multiple studies have shown that quadrupole sound sources do not significantly contribute to the overall propeller noise. Solutions show an increase of 2 or 3 dB due to quadrupole effects [36, 65], and up to 5 dB in the supersonic regime [53]. These tests were all performed in the forward thrust regime.

Due to the high computation times and the low significance of these quadrupole sound sources, the nonlinear component is often neglected in predictions. Noise from jet engines is an example of a sound source of quadrupole nature [43].

3.2. Rotational Noise

Aerodynamic propeller noise can be divided into two primary forms of noise radiation: periodic noise and broadband noise [17, 43, 55]. Rotational noise is a form of periodic noise and can again be divided into thickness and loading noise. These noise sources are overviewed in Figure 3.2.

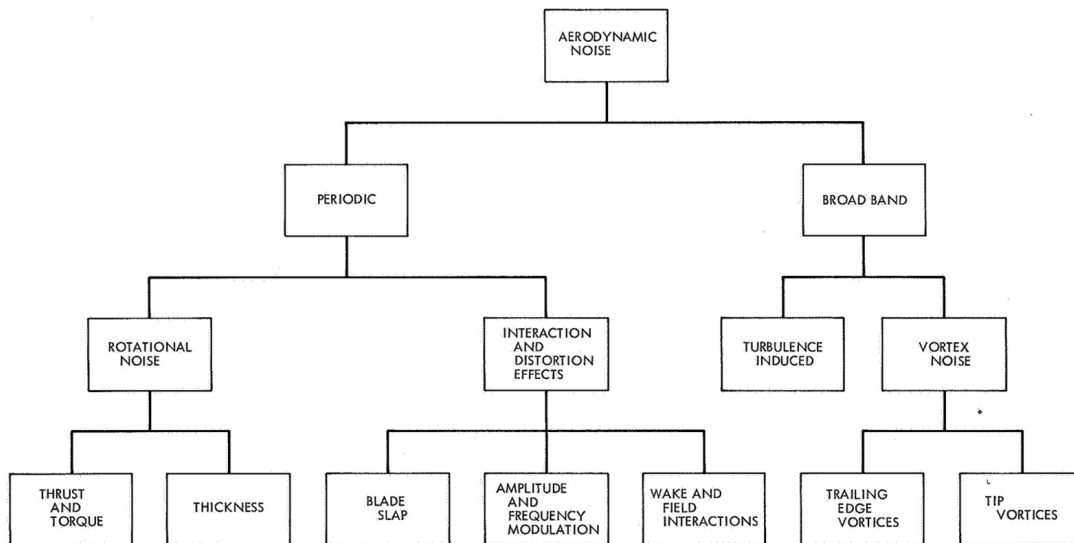


Figure 3.2: Different types of aerodynamic noise [43].

Rotational or tonal noise is the noise radiated as an effect of the rotation of the propeller blades. Contrary to broadband noise, rotational noise is narrow-banded radiation. Rotational noise can be recognized by looking at the discrete frequencies at the harmonics, which are multiples of the blade passing frequency [43], shown in Equation 3.2. Suppose one point is considered in the propeller disk. In that case, rotating blades will pass this point with the blade passing frequency, calculated by multiplying the rotational velocity by the number of blades in Equation 3.2. As the blade passes through a fixed point, the air is pushed away by the volume of the blade, causing pressure disturbance and radiating sound waves [17]. This occurs every time the blade passes at the blade passing frequency. The disturbance of the air is schematically shown in Figure 3.3, the resulting sound shown to be a periodic waveform. The oscillating components portrayed in this figure are oscillations with frequencies that are multiplications of the fundamental frequencies [17]. Thus, a rotating blade causes multiple harmonics, which are directly correlated to the base frequency of the blade [55].

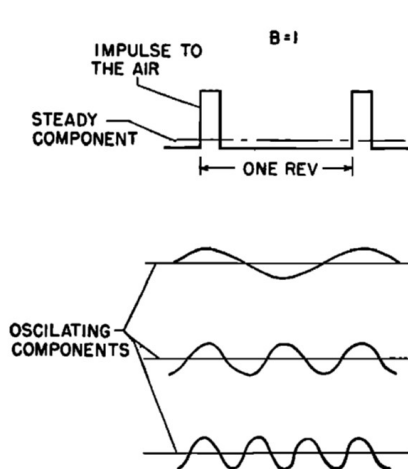


Figure 3.3: Schematic diagram of the steady and oscillating components of the impulses by a single propeller blade [55].

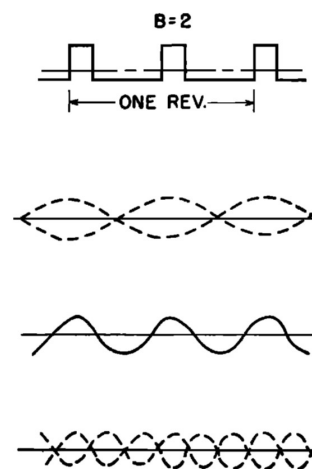


Figure 3.4: Steady and oscillating components of the impulses by two propeller blades [55].

In the case of a second blade, The blade passing frequency doubles, and cancellation between these two blades occurs for every other harmonic. The other harmonics, on the other hand, amplify each other and become twice as large. The thrust force is doubled with an extra blade at a constant speed. If constant thrust is assumed as shown in Figure 3.4, the harmonics that are not canceled out by each other will have equal amplitude and frequency as the harmonics with one blade [55]. As the amplitude stays the same and every other harmonic cancel out, the resulting noise is reduced. This means that adding blades results in noise reduction for constant power [55]. However, as shown in Figure 3.5, the addition of blades also causes another type of noise to increase, vortex noise. Vortex noise is an example of broadband noise and will be discussed extensively in section 3.3.

$$BPF = nB \quad (3.2)$$

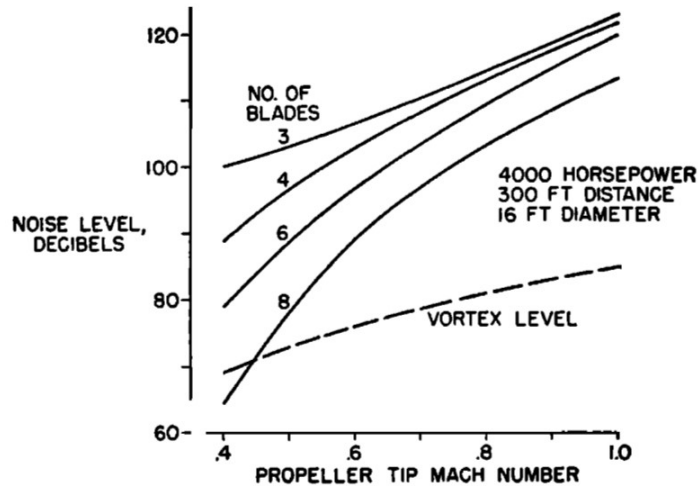


Figure 3.5: Effect of the number of blades at different tip speeds on noise levels for constant power [55].

3.2.1. Loading Noise

Loading noise sources result from forces that act on the blades due to the created pressure distribution. The blades are initially designed to produce a pressure variation to create a lifting or thrust force. This pressure distribution is constant from the blade's perspective when a uniform flow is assumed [43], and can be split up into lift and drag (the components perpendicular and aligned to the zero lift line, see Figure 3.6) or thrust and torque forces (the components normal to and in the plane of the disc area of the propeller), as described in Figure 3.2. As the forces on the blades are constant when a uniform flow is assumed, this noise source is considered a steady loading noise [38, 53]. From an observer in a fixed point, the disturbance of the surrounding fluid oscillates with the blade passing frequency. Therefore, loading noise can be described as a dipole sound source type. Loading noise on propellers can be seen as a mesh of dipole sources pulsating at blade passing frequency [43]. Gutin (1948) gave the first complete definition of steady loading noise on propeller blades [53].

3.2.2. Thickness Noise

Another example of rotational propeller noise is thickness noise. Thickness noise is noise as an effect of the volume of the blades and is one of the primary propeller noise sources [38]. However, Deming suggested that loading noise was larger than thickness noise for conventional propellers [53, 55]. Marte et al. (1970) and Diprose (1955) explain that thickness noise is insignificant compared to loading noise at speeds below sonic, but it can gain dominance at higher tip speeds [43, 53]. As each blade has a finite volume, every time the blade approaches a fixed point in the earlier considered propeller disc area, a volume of air is continuously displaced or extracted at that point and then injected again when the blade exits the point [38, 43, 53]. This can be considered a pulsating monopole source, oscillating at blade passage frequency.

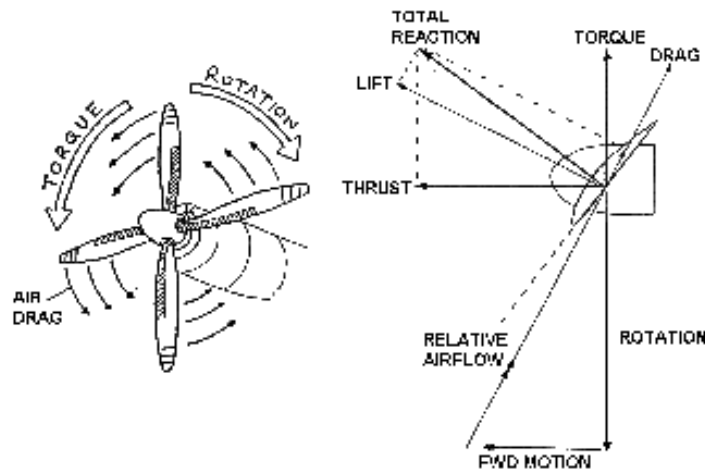


Figure 3.6: Aerodynamic loads acting on propeller blades [1].

Lowson (1965) showed that thickness noise could not be categorized as just a monopole sound source, as it contains different components that account for different noise sources [53]. According to Lowson, convection due to mass displacement causes a dipole effect, and acceleration causes a quadrupole effect. Generally, loading and thickness noise represents the linear components in the noise field, while the non-linear, quadrupole effects gain importance when flow disturbance becomes more significant [53]. This shows that categorizing a noise type as a sound source is not always uncomplicated.

The strength of the source depends on the rate of mass displacement, determined by the geometry of the propeller blade [43]. The more volume a blade has, the larger the displacement of mass, and the more thickness noise is radiated. The frequency of thickness noise is related to the blade passing frequency, similar to loading noise. The airfoil shape and the geometry, such as blade width, have importance at higher harmonics but do not affect the amplitude of the radiated thickness noise much at low harmonics [55]. The volume of the blades is constant for different operating conditions. If the propeller operates at zero lift condition or zero thrust, the blades will still radiate periodic noise due to their volume. Loading noise in such conditions will minimize as the loads decrease. However, even though the lift is zero, drag loads will still be present.

3.3. Broadband Noise

Rotational noise can be seen as the component radiated by the blades in inviscid flows. They appear as sharp peaks in the spectral analysis [17]. The component that is added when the flow is introduced to viscosity is considered to be the broadband component [17, 43]. Broadband noise shows random characteristics in the spectral analysis over a wide range of frequencies. This includes flow separation, turbulent boundary layers, vortices, and blade wakes. Generally, experiments focus on tonal noise primarily, but for the total noise levels, broadband noise can have a significant contribution [41]. The significance of this noise type in the regime of negative thrust remains unclear. Deming's work was elaborated by Yudin and added the basis of the currently used analytical definition of vortex noise [17]. Section 3.6 will discuss how broadband noise could become more significant in the noise field at negative thrust conditions.

Vortex noise is an example of broadband noise and can be considered the dominant source of broadband noise. This noise source can be split into two types of vortex noise, trailing edge noise and tip noise [55]. Trailing edge noise is a blade self-noise and originates from the dispersal of the turbulent boundary layer at the trailing edge of the blade [62]. Tip noise originates from the shedding of vortices in the flow at the tip of the blades [43] and contributes mainly to the high-frequency broadband noise [15]. Blades that operate in the tip vortices or unsteady blade wakes from a previous passing blade cause unsteady noise [43], resulting in broadband frequency noise sources. Adding blades will increase the interference between the blades with the tip vortices from the preceding blades as the blade passing

frequency increases at a constant rotational speed. Tip vortices or wakes will then have less time to exit the operating area of the upcoming blade. The third source of broadband noise is turbulence-induced noise. This is caused by turbulence in the airflow, which affects the flow at the leading edge of the blade [62].

3.4. Directional Propeller Noise

Every noise source has its noise patterns as shown in Figure 3.7. These are theoretical noise patterns that are not always representative of empirical data. The lobes of a dipole noise source are distinguishable, as are the four lobes of a quadruple noise source. The conditions in which propeller blades operate, such as uniformity of the flow, also affect the polar distribution of these sources.

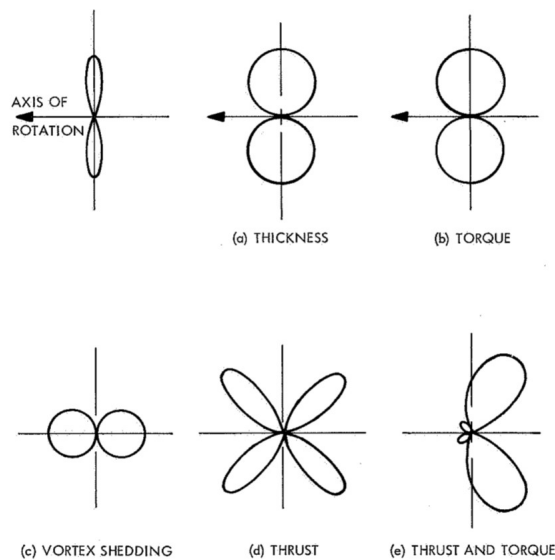


Figure 3.7: Theoretical noise patterns for rotors, propellers, and fans [43].

The sound source influences the directivity of noise, but also interference effects can affect the radiation of noise at certain angles. If noise's directivity is not considered, one might derive incorrect conclusions by measuring noise at one point or angle. Block (1986) found that pusher configuration propellers were quieter than the tractor configuration, as the pylon caused a decrease in propeller noise at a small range of angles compared to the pusher configuration. Still, an increase in every other direction [11].

Theoretically, propellers in a homogeneous space will show a symmetric noise radiation pattern around the axis of rotation, see Figure 3.7. This would suggest that the noise pattern is not affected by the direction of rotation. In reality, the inflow direction and variation in pressure distribution due to interference of the wing, for example, will cause an effect on the direction of the rotation [55].

3.5. Propagation Effects

Sound travels, and as it travels, its properties change through time. The forces or disturbances caused by the propeller blades to the air propagate through space and then arrive at the observer. This section will discuss the way noise propagates through air. The distinction is made between near-pressure fields and distant pressure fields [55]. The near pressure field is close to the propeller up to a couple of diameters of the propeller disc. Further away from the source is considered the distant pressure field. The initial amplitude of the pressure fields is dependent on the forces exerted by the blades. Still, more factors other than the blades affect the propagation and attenuation of sound waves.

3.5.1. Noise Propagation

The geometric distance between the sound source and the observer is one of the main reasons for the sound loss in flux intensity, the gradual weakening of sound over a distance. The further away the observer is from the source, the lower the intensity of the sound waves become. If a homogeneous point source is considered, the sound pressure varies inversely as the square of the distance when it arrives at the observer [43, 55]. This estimation is valid for observers in the far field where 6 dB is lost every time the distance between the source and observer doubles [43].

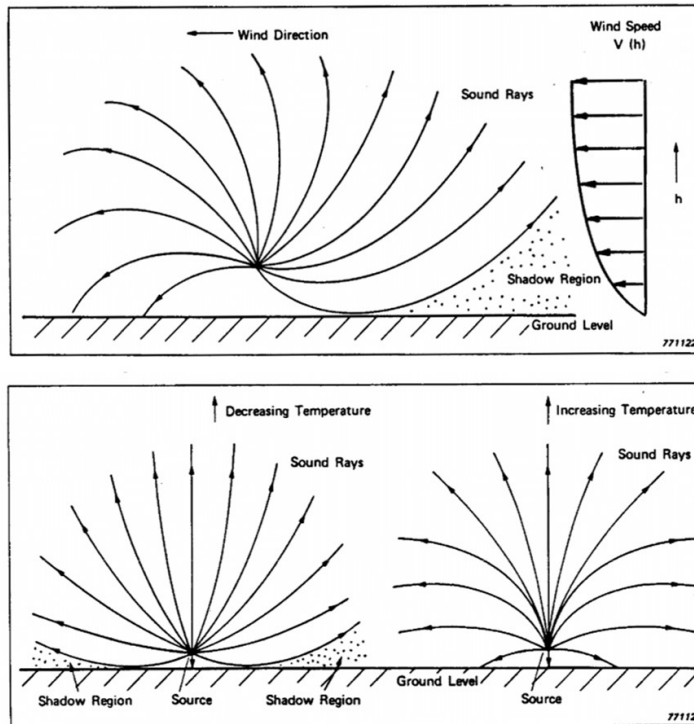


Figure 3.8: Atmospheric conditions affecting sound rays [44].

3.5.2. Atmospheric Attenuation

Two other factors that make sound waves lose energy while propagating are due to the atmosphere. The first is classical absorption. Energy is assimilated through heat conduction, radiation, viscosity, and diffusion [43]. The loss varies with the square of the frequency of the sound wave. Thus, sound wave components of harmonics at higher frequencies have more considerable atmospheric attenuation than the lower harmonic components. A design of propellers with radiations dominating the higher frequencies would take advantage of the classical absorption. However, the human ear is less sensitive to lower frequency sound waves [55].

$$\frac{\cos\theta_2}{c_2} = \frac{\cos\theta_1}{c_1} \quad (3.3)$$

The second factor is attenuation as a function of humidity and frequency which involves molecular relaxation in the air [43]. Energy loss due to the molecular relaxation in the air is more crucial than classical absorption, as the effect is more significant in humans' frequency range. Other atmospheric conditions that affect the magnitude and direction of the sound waves are wind, turbulence, temperature, and humidity, as shown in Figure 3.8 for wind and temperature. This figure shows that sound rays in a real atmosphere are not straight. This is due to the refraction of sound rays between different media. Snell's law calculates the incoming and outgoing angles of the refracted sound rays between two media in Equation 3.3. It shows that the speed of sound affects the angles between two media. This causes curved sound rays in a real atmosphere where the speed of sound changes over distance. This effect is shown in the bottom drawing of Figure 3.8. The wind has the same effect as the speed of

sound changes with wind speed. The refraction will depend on the direction of the wind and the direction of the noise propagation shown in the top drawing of Figure 3.8. Both effects can create shadow regions where no sound rays arrive.

3.5.3. Frequency and Amplitude Modulation

The Doppler effect modulates the frequency of the radiated sound waves. The Doppler effect results from the relative movements between the sound source and the observer. The impact of the relative movement influences the observed frequency as shown in Equation 3.4.

$$f = f_0 \frac{c + v_o}{c - v_s} \quad (3.4)$$

Where the observed frequency f_o equals the formula including the source frequency f_0 , speed of sound c , speed of the observer v_o , and the speed of the source v_s . This equation shows that the frequency decreases for movements that result in a greater distance between the source and the receiver, while the opposite happens when the observer and source move towards each other [8]. The aircraft moves towards a fixed observer and away from the observer during a flyover. The frequency of the emitted sound will be different than the observed frequency due to the Doppler effect [43]. The frequency shift is visible in Figure 3.9.

The fundamental frequency of propeller blades also differs in resulting vector direction and magnitude for a propeller blade moving away from the observer than a blade approaching the observer. The blade moving away from the observer has a negative resulting vector of a smaller magnitude than the blade moving towards the observer with a positive larger resulting vector [55]. Because of the difference in magnitude, they do not cancel each other out entirely. The retreating blade cancels the approaching blade partly. It is interesting to note that shielding noise by a wing, for example, could cause an increase in the observed noise when the canceling vector is shielded. If it is attempted to shield propeller noise, it should shield the approaching propeller sound waves. The approaching blade causes much higher pressure changes than a blade moving away. When the tip speed is doubled from $M_t = 0.62$ to $M_t = 1.25$, the blades make more than six times as much sound at constant thrust [55]. Therefore, higher tip speeds radiate relatively more noise than blades at lower tip speeds. With the increase in the number of blades, lowering the tip speeds is an effective measure to decrease propeller-radiated sound. Lower tip speeds result in more thrust-efficient propellers as the efficiency reduces at higher rotational speeds. According to Brown et Al. (1971), however, these measures to lower propeller noise do not seem to be effective in reality [17], while Hanson (1980) concludes they are effective, but more for financial reasons and efficiency or weight reduction [34].

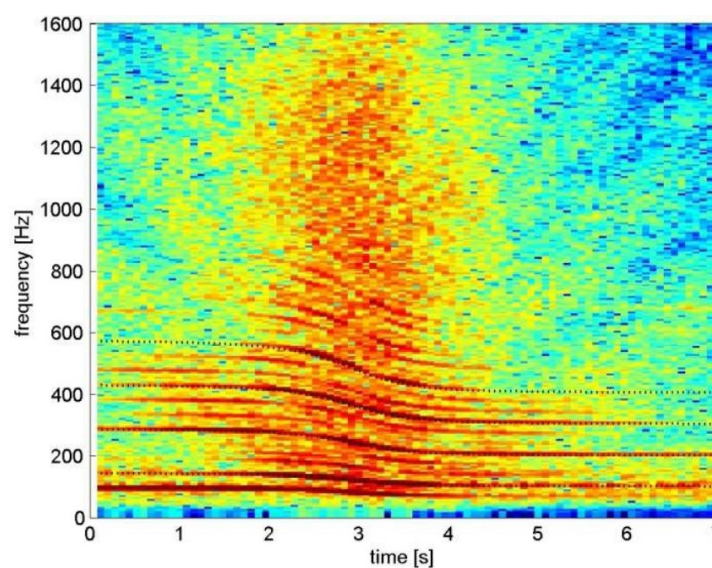


Figure 3.9: Spectrogram of the noise emitted by a propeller-driven aircraft [61].

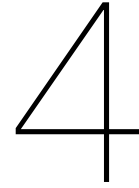
3.6. Propeller Aeroacoustics at Negative Thrust

The problem of aircraft noise became more pronounced as propeller power increased with the arrival of jet engines. Also, the increase of flights in densely populated areas makes the study to decrease aircraft noise radiation more relevant. At negative thrust conditions, different noise sources might be dominant compared to forwarding thrust conditions, as the geometry of the propellers is mainly optimized for efficiency at conventional operating conditions. The sub-optimal airfoil in negative thrust conditions is more susceptible to flow separation, which causes a source of broadband noise. One of the abilities of the negative thrust condition is to decrease the velocity during landing while recharging the battery, a critical operation regarding sound annoyance, as descent usually occurs in densely populated areas.

The vast majority of the literature discusses the noise of propellers in the conventional forward thrust condition. Many researchers have looked into the radiated noise of propellers in forwarding thrust conditions, as the produced noise became a rising problem with the increase of propeller-mounted aircraft in densely populated areas [17, 18, 31, 38, 43, 55]. Extensive studies have been performed on the prediction of propeller noise as well as the collection of empirical data in the forward thrust regime. In general, the final objective was often to decrease the propulsion noise.

In the latest study by Goyal et al. [27], it is stated that aerodynamic and aeroacoustic characteristics are significantly distinct for propellers in forwarding thrust conditions compared to negative thrust conditions. Goyal (2021) has made numerical approaches to predict propeller noise in both regimes but concludes that the relevance of broadband noise in the negative thrust regime is still unclear.

When conventional propellers operate at reversed thrust conditions to regenerate energy, the loads tend to cancel out, and the loading noise becomes lower than forward thrust propulsion. However, the thickness noise increases, and broadband noise may gain significance due to the separation of the boundary layer as an effect of the sub-optimal blade design in this condition. Separation of the boundary layer will induce a turbulent wake with pressure fluctuations that generate noise over a wide range of frequencies. In an experimental study, this separation could be accurately simulated to show the importance of broadband noises at negative thrust conditions compared to forwarding thrust conditions.



Aeroacoustic Experiments on Propellers

4.1. Similarity and Scaling Parameters

4.1.1. Mach number and Reynolds number

During wind tunnel experiments, one always tries to simulate real flight conditions within a controlled setting. However, due to limitations, real-life conditions can not always be simulated precisely. Due to size limitations, for example, a scaled model is often used to simulate the effect of loads on the real-size model depending on the wind tunnel size. The scaling of a model influences how the fluids act on the model's surface. Aerodynamic performances change when flight conditions are not matching, while it is essential to maintain similarity for an experimental study. Two main similarity parameters are the Reynolds number and the Mach number. Reynolds number (Equation 4.1) is a parameter representing the ratio of inertial forces to viscous forces. The Mach number (Equation 4.2) relates to the compressibility of the fluid. Compressibility effects become more significant at higher Mach numbers.

$$Re = \frac{\rho VL}{\mu} \quad (4.1)$$

Where ρ is the density, V is the velocity, and μ is the viscosity coefficient. L indicates the characteristic length of the problem, and c is the speed of sound.

$$M = \frac{V}{c} \quad (4.2)$$

To maintain similarity between real-life conditions and experimental cases, it is essential to match the Reynolds, and Mach numbers between the two [32]. If the two similarity parameters correspond to each other in an experiment, the relative dominance of forces on the model is as to be expected in real life. This method is based on the principle of similitude, which states that if two systems are similar in terms of dimensionless numbers, they are similar in terms of behavior. The relationship between how the aerodynamic forces change with the fluid's viscosity is very complex. The behavior of the boundary layer on a surface is highly dependent on the fluid's viscosity, which is an essential effect for studies in aerospace applications. The scaled thickness of the boundary layer is inversely correlated with the Reynolds number. The boundary layer changes the effective shape of the model, which results in different performances. If the boundary layer continues to grow, it can separate from the surface, causing unsteady flow conditions. The drag of an object is also highly dependent on viscosity.

Real flights occur at high Reynolds numbers, and scaled models in atmospheric conditions will not have the same Reynolds number. Some wind tunnels can compensate for the difference by pressurizing the wind tunnel or by altering the fluid's viscosity. Sometimes the tripping technique is used to induce boundary layer transition at low Reynolds numbers. However, there is a risk of over-correction with this technique. Propeller performance highly depends on the Reynolds number [9]. This is also shown in Figure 4.1, where the propeller efficiency increases significantly with the Reynolds number, especially at high advance ratios. Matching the Reynolds number in a laboratory is challenging, depending on the

facility. The freestream velocities are often lower, and the model is often scaled. The experiments in this thesis will have a Reynolds number ranging from $Re_c^{0.7R} = 0.8 \cdot 10^5$ to $Re_c^{0.7R} = 1.9 \cdot 10^5$, much lower than real-life conditions with a full-scale propeller which has a range up to $Re_c^{0.7R} = 1.0 \cdot 10^6$ or higher. A lower Reynolds number shows a decrease in propeller efficiency for the entire range of advance ratio. This is a result of the thicker boundary layer at lower Reynolds numbers [7]. A thicker boundary layer increases the drag while lift forces decrease. This results in a more significant decrease in thrust than torque and, thus, reduced propeller efficiency.

Mach number is essential as the compressibility effects are related to the Mach number. The Mach number is the ratio between the aircraft's velocity and the speed of sound. In subsonic wind tunnels, compressibility effects are usually neglected, as the Mach numbers are low. At low Mach numbers, the density is assumed to be constant. The energy of the air molecules rises when the Mach number rises, with local pressure increase as an effect. Compressibility effects cannot be ignored when velocities approach the speed of sound or higher. Disturbances cause shock waves at these high Mach numbers. The tip Mach number is the most critical parameter for aeroacoustics as it approaches the speed of sound the fastest. The tip Mach number strongly affects the generated sound levels by the blades. Propeller noise is characterized by amplitude and frequency. The frequency of discrete tones will occur at the BPF and its multiples or harmonics. The pressure disturbances are related to the aerodynamic pressure distribution of the propellers. Therefore, the Mach number is the most critical similarity parameter in aeroacoustics.

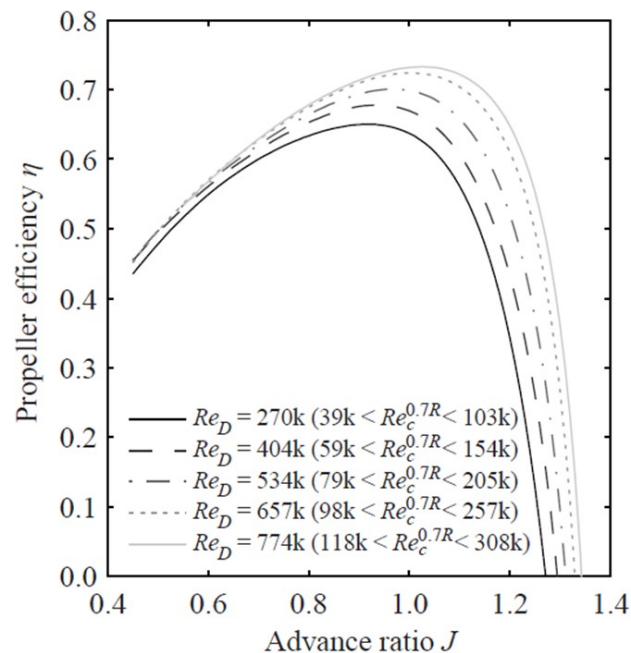


Figure 4.1: Effect of Reynolds number on propeller efficiency for different advance ratios [62].

The local Mach number on a propeller blade is given by Equation 4.3 at a blade section. The Mach number should be similar to the full scale to ensure similarity in tonal noise when equal loading is assumed. By keeping this similarity parameter equal to a full-scale propeller, it can be assumed that the relative wavelength with respect to the model's dimensions and its noise levels will remain similar [16]. For a scaled model, r is scaled down. Therefore the angular frequency, ω , has to be scaled up for a constant speed of sound. The magnitude of the radiated propeller noise of the model scales inversely proportional with the distance at which the sound waves are recorded, which means that a scale model of 1:2 will emit the same noise level at a certain distance as the full-scale model at half that distance and twice the frequency. Broadband noise, unlike tonal noise, exhibits a complex relationship between frequency and scaling. This is because the scaling of broadband noise is influenced by factors such as the interaction with the boundary layer, which can vary with frequency. Despite this complexity, the

general relationship between frequency and scaling remains constant for broadband noise.

$$M_t = \sqrt{M_\infty^2 + \left(\frac{\omega r}{c}\right)^2} \quad (4.3)$$

The Mach number scaling of propeller noise can be derived using the theory proposed by Hanson in [34], or by Lighthill in [46]. This approach considers the lifting surface, such as the propeller blade, to produce noise proportional to the Mach number's sixth power. This scaling relationship accounts for the contributions of dipole and quadrupole sources in the noise generation process [26].

4.1.2. Dimensional Analysis

Dimensional analysis is an established methodology for comparing quantities with their respective base units. These base units play a crucial role in propeller design and are essential in evaluating performance outcomes. In propeller noise, the blade passing frequency (BPF) is frequently employed to normalize frequency according to the Strouhal number, a non-dimensional metric. The Strouhal number is the ratio of the sound frequency to the velocity of the motion multiplied by the characteristic length of the system. By normalizing frequencies to the BPF, the Strouhal number remains constant for scaled experiments when operated at equivalent advance ratios as the full-scale propeller. Consequently, it is common practice in the literature on propeller noise to express the amplitude as a function of the multiples of the BPF [12], where the Strouhal number is defined as Equation 4.4. This approach allows a more direct comparison between a propeller's noise and its blades' rotation frequency.

$$St = \frac{f}{B \cdot \omega} \quad (4.4)$$

In aeroacoustics, noise amplitudes are frequently reported regarding sound pressure level (SPL) in decibels, a logarithmic measure. The definition of SPL is shown in Equation 4.5, where the measured pressure data is normalized with the reference pressure, p_0 . The reference pressure of 20 μPa is based on the threshold of human hearing, and thus, an SPL of 0 dB corresponds to the lowest sound level that human ears in the air can perceive.

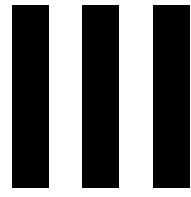
$$SPL = 20 \log_{10} \frac{p_{rms}}{p_0} \quad (4.5)$$

However, the human threshold is not a scalable parameter. This makes a direct comparison of data between different scales challenging. Geng et al. (2021) have made an effort to define a physics-based scaling approach for propeller noise to obtain scalability for the amplitude based on the thrust instead of the threshold of human hearing [26]. The dimensionless Π (Equation 4.6) was defined to evaluate the effect of the disk loading on the acoustics. Using this definition, it is possible to express the propeller noise in terms of scaled frequency and amplitude. This makes scaling the mounted propeller to a full-size propeller in real flight more straightforward.

$$\Pi = 20 \log \frac{p_{rms} \cdot D^2}{T} \quad (4.6)$$

4.2. Effect of Propeller Thrust in a Wind Tunnel

Thrust and drag can be corrected for tests where momentum or sources and sinks occur in the wind tunnel [23]. A propeller is theoretically a plane in the test section that adds momentum to the flow. The error in thrust and drag comes from the fact that flow velocity increases by adding the propeller's momentum. This additional momentum is at normal conditions, not present in the wind tunnel [23]. Two models are usually used to correct this effect. The effect of a propeller operating in forwarding thrust conditions (momentum source) is the opposite of one operating at negative thrust conditions (momentum sink). The correction confides on obtaining an equivalent free stream velocity for the given thrust, where the thrust is estimated from the momentum equation for the free stream on the one hand and the combination of pressure and momentum consideration in the closed wall wind tunnel on the other [23].



Methodology

5

Experimental Setup

The framework of the research is divided into three main parts, the harvesting of propeller data, the experiment, and the processing and analysis of the data. This section will include specifications of all the materials used to perform the acoustic measurements. Furthermore, it will explain the different test conditions and the test matrices used during the experiment. The measurement challenge of the thesis is to assess the relative importance of tonal and broadband noise types generated by propeller noise sources in the negative thrust regime. The results will be compared to the noise sources generated by propellers in forward thrust as a reference. Noise generated by the propeller is dividable into two categories: harmonic noise and broadband noise. The motor, wind tunnel fan, and other wind tunnel systems can cause unwanted noise sources and vibrations. Each of these noise sources can interfere with the wanted signal.

The effect of negative thrust on propeller noise is quantified in terms of thickness noise, loading noise, and broadband noise with respect to those noise types in forward thrust. At negative thrust mode, the boundary layer separation might play a significant role in the shift of the relative importance of the noise types due to the detachment of the flow on the lower surface of the airfoil, causing a turbulent wake. Other aerodynamic effects, such as laminar separation bubbles (LSB), are likely to occur at low Reynolds numbers [28]. The Reynolds number of the tests ranges from $0.5 \cdot 10^5$ to $2.0 \cdot 10^5$. The possible presence of laminar separation bubble noise should therefore be kept in mind for propellers operating at low Reynolds numbers. Laminar separation bubbles are known to cause high-frequency noise [28]. The propeller at negative thrust conditions will operate at sub-optimal conditions with conventional propellers, as they are optimized for forward thrust settings.

5.1. Wind-Tunnel Facility

The acoustic experiments have been carried out in the low-turbulence wind tunnel (LTT) at the Low-Speed Wind Tunnel Laboratory at Delft University of Technology. This is an atmospheric closed-throat single-return type of tunnel of which the closed-wall test section has an octagonal cross-section of 1.80 x 1.25 meters and a length of 2.60 meters. The top and bottom parts of the test section have flushed turntables for the attachment of the model. The wind tunnel has a fan with six blades, driven by a 525 kW DC motor with a maximum free-stream velocity at the test section of 120 m/s. The corners of the wind tunnel have been installed with corner vanes to guide the flow through the corners while maintaining constant flow characteristics. These vanes feature a cooling system to regulate the temperature of the flow [3]. The turbulence intensity of a wind tunnel section shows how constant the wind speed is in the wind tunnel with respect to the mean wind speed [40]. The turbulence intensity of this wind tunnel varies from 0.015% at 20 m/s to 0.07% at 75 m/s. These are high-quality flows due to the large contraction ratio of 17.8:1. The contraction area of a wind tunnel increases the flow velocity at the test section and contributes to a uniform flow. Buoyancy can be neglected due to the diverging test section that reduces the longitudinal pressure gradient. The diverging test section and the other described components of the wind tunnel are well shown in Figure 5.1. For acoustic measurements, it has to be considered that the tunnel is a closed- and hard-wall test section without acoustic lining for acoustic absorption, which

is undesired for carrying out acoustic experiments. Therefore, acoustic experiments will experience reflections of the noise source from the model and noise and vibrations from the wind tunnel system.

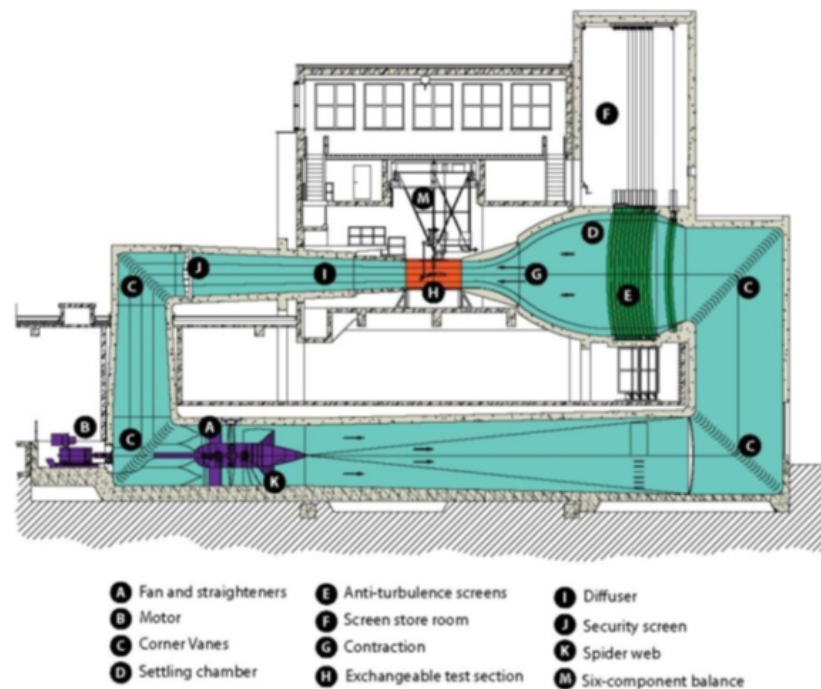


Figure 5.1: Drawing of the Low-Speed Wind Tunnel Laboratory at Delft University of Technology.

5.2. Propeller Model and Geometry

The TUD-XPROP propeller is used as the propeller model. The TU Delft propeller represents earlier models of a typical turboprop propeller. It has up to six blades that are independently assembled to the hub. They have no sweep and can be mounted to the hub at any blade pitch angle. For the acoustic measurements, the blade pitch angle is set to 30° . The blades are made of carbon fiber, and the propeller has a diameter of $\varnothing 0.4064$ m. The propeller hub has a diameter of $\varnothing 0.122$ m. The local thickness-to-chord ratio of the airfoil sections varied from 5% mm near the tip to 36% at the hub. The local blade pitch angle was set to 30° at 70% of the radial distance, varying from 22° at the tip to 57° at the hub. A schematic drawing of the setup is shown in Figure 5.2. The propeller is attached to the nacelle with the electric motor, which is water-cooled, at the rear of the nacelle in front of the support beam. The distance from the propeller disc plane to the heart of the motor is 470 mm, and it has a length of 107 mm. The motor shaft is attached to the propeller shaft using a shaft coupling. The nacelle is attached to the support beam, which is covered by a removable 3D-printed fairing. The support beam (650 mm from the propeller plane) passes through the top turntable of the wind tunnel test section and connects to the external six-component balance above the test section, see Figure 5.1. The angle of attack for this model is fixed, while the sideslip angle can be varied by rotating the turntable to any angle.

5.3. Measurement Techniques

5.3.1. Six-Component External Balance

The force balance is a primary measurement device for the wind tunnel. External six-component balances are used to measure aerodynamic forces and moments on the model in three axes (x, y, and z) with high precision, using strain gauges. An element in the gauge is stretched, and the force is computed with the resistance and current that runs through the gauge element using Ohm's law [52]. This information is then forwarded to the control room of the wind tunnel. The balances are called external, as they are positioned outside the test model in the wind tunnel. The support beam of the model is directly assembled to the external balance above the test section. Therefore, the systems are not

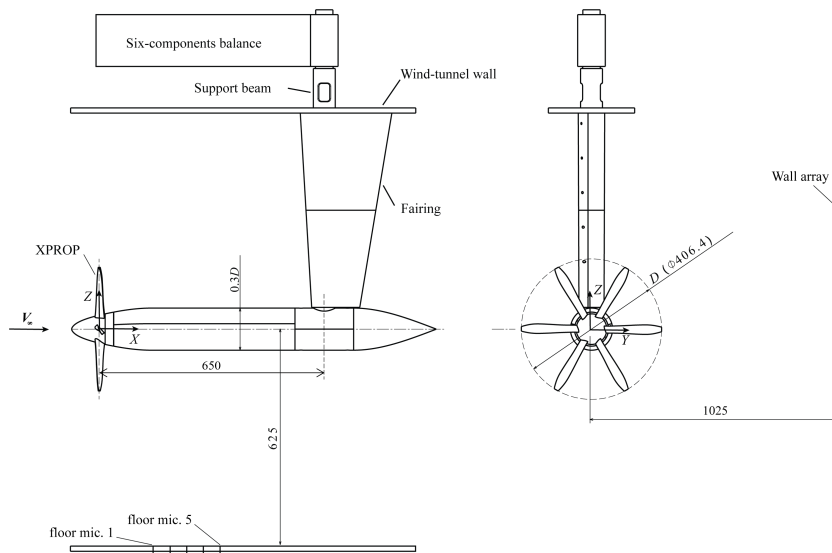


Figure 5.2: Schematic drawing of the side view (left) and the front view (right) of the model setup and microphone positions.

interfering with the flow field. Before every measurement during the experiment, zero measurements are performed to remove forces and moments on the external balance that are not of aerodynamic nature. This is done to cancel out external factors that act on the balance, which are not aerodynamically induced forces or moments. Examples of these factors include the model's weight or stresses in cables.

5.3.2. Microphone Specifications and Placement

Two microphone arrays were placed in the test section as shown in Figure 5.3, one in the side wall perpendicular to the propeller plane and a linear array on the floor aligned under the rotational axis of the propeller. The wall array consists of 58 G.R.A.S. 40PH analog free-field microphones with a diameter of 7 mm, a frequency range between 10 and 20 kHz, and a maximum SPL of 135 dB. The floor array consists of 5 microphones. The position of the combined 63 microphones is shown in Figure 5.4. The wall array is located at a distance of 1025 mm in the y-direction from the center of the propeller hub, outside the flow. This was done by placing a Kevlar fiber wall between the flow and the microphones. The floor microphones are placed directly below the propeller and flushed with the test section's floor. An out-of-flow placement of the microphones will increase the distance from the noise source to the microphones, but it has the advantage that it does not disturb the flow with self-noise, which is another unwanted noise source.

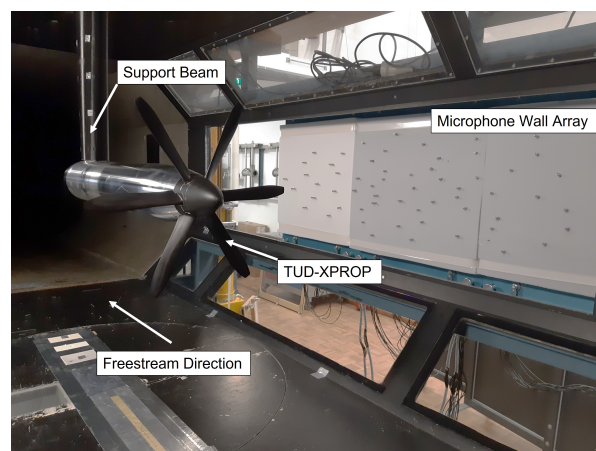


Figure 5.3: Picture of the model setup and the microphone array on the wall and floor.

The microphones are positioned on an acoustic array with a width and height of 1.349 m and 0.402 m, respectively. The floor array is aligned with the flow direction in the center of the propeller installed in the bottom turntable of the test section at a distance of 625 mm in the z-direction from the hub. The 63 microphones were covered with a layer of Kevlar fiber cloth during the acoustic experiments. This acts as a wall and separates the test section from the area where the microphones are placed. According to multiple studies, acoustic measurements using Kevlar test screens experience a significant loss in noise levels [49]. It is not proven that it also changes the acoustic composition of the sound waves. The microphones record the pressure difference as a voltage. This voltage can be converted to pressure units after applying the calibration of the microphones, meaning that the low-frequency range of the measurements is near-field. At the same time, the high-frequency region could be considered far-field.

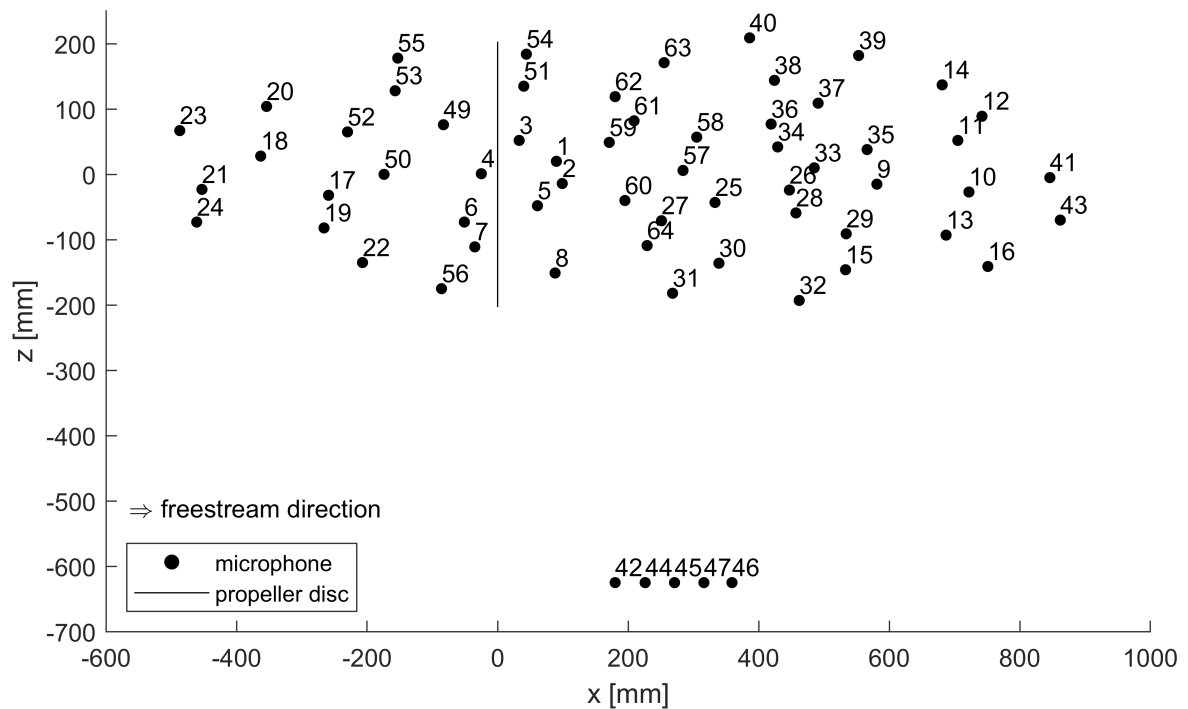


Figure 5.4: Microphone wall and floor array positions with its number, seen from behind the wall.

All microphones were placed at least 0.422 m away from the propeller blades. While the definition of far-field is not set in stone, a rule of thumb exists that far-field starts at approximately one wavelength, λ , from the source. Following this rule of thumb, frequencies below 800 Hz for the floor microphones and 550 Hz for the wall microphones are considered near-field for the nearest microphones.

5.4. Test Conditions

The design of the test setup and the test or the test matrix was pre-determined and not adapted to the purpose of acoustic measurements. The propeller noise can be contaminated or even masked by motor noise, vibrations of the test rig and wind tunnel structure, and tunnel wall reflections of the test section, as the wind tunnel is not acoustically treated. The wind tunnel is operated at 20 and 30 m/s wind speeds for acoustic measurements. These possible wind speeds could offer positive and negative thrust settings. To observe the aeroacoustic effect of the propeller in negative and positive thrust settings, the advance ratio (see Equation 5.1) was varied between 0.6 and 2.0, where V_∞ is the axial flow velocity in meters per second, n the angular frequency of the propeller in hertz, and D the diameter of the propeller in meters. These advance ratios correspond to the thrust settings ranging from $C_T = -0.35$ to 0.3, see Figure 5.5.

$$J = \frac{V_\infty}{nD} \quad (5.1)$$

The Reynolds number for these tests varies between $0.8 \cdot 10^5$ and $1.9 \cdot 10^5$, where the kinematic viscosity, ν , is $1.46 \cdot 10^{-5}$. Measurements were taken of the propeller motor without blades to quantify the sound levels of the propulsion system. These are the noise levels of the motor without loading. Wind tunnel noise was measured for each wind speed without propellers and the background noise without propeller noise or noise from the electric propulsion or the wind tunnel system. It is crucial to measure these sources that are not propeller related to identify them as external noise sources in the propeller noise measurements. All acoustic measurements lasted for 30 seconds, the sample time of the acoustic data. Acoustic measurement of a large duration translates directly into a higher possible resolution data in the frequency domain [59]. The angle of attack was fixed at 0° for every run. The angle of the sideslip was constant at 0° as well. The number of blades was six during all the runs.

Table 5.1 shows the test matrix for the first run. Test number 1 of run 1 measured the background noise. The wind tunnel and propeller were off during the background noise test. For the other tests of run 1, the flow speed was kept constant at 30 m/s, and the advance ratio was varied from 0.8 to 2.0 by varying the angular frequency of the propeller and keeping the wind speed constant. For run 2, in Table 5.2, the wind speed was constant at 20 m/s, and the advance ratio was varied from 0.6 to 2.0 in the same way as in run 1. The data from these two first runs will contain the propeller noise. Runs 3 and 4 are measurements of the propulsion system of the propeller without propeller loading, mainly the motor noise and possibly vibrations. The motor spins without blades or blade loading at different angular frequencies in runs 3 and 4 correspond with the speeds done in runs 1 and 2, respectively. During these measurements, there was no wind speed. Finally, in Table 5.5, sound measurements were performed at different wind speeds with the model but with no assembled blades or propulsive noise. Test 3 and 1 from run 5 correspond to the wind speeds of the tests in run 1 and 2, respectively. The propeller has six blades, and the wind tunnel fan has six blades. The blade passing frequency of the propeller and the wind tunnel fan can be calculated using its revolutions per second multiplied by the number of blades. The pitch angle of the blades is 30° for every test. Figure 5.5 shows that $J < 1.4$ has positive thrust coefficients, and for $J \geq 1.4$, thrust coefficients are negative with a pitch of 30 degrees. Therefore, the propeller in test numbers 1-4 (2-4 for run 1) generates a positive thrust force, and test numbers 5-10 generate a negative thrust force in both runs 1 and 2.

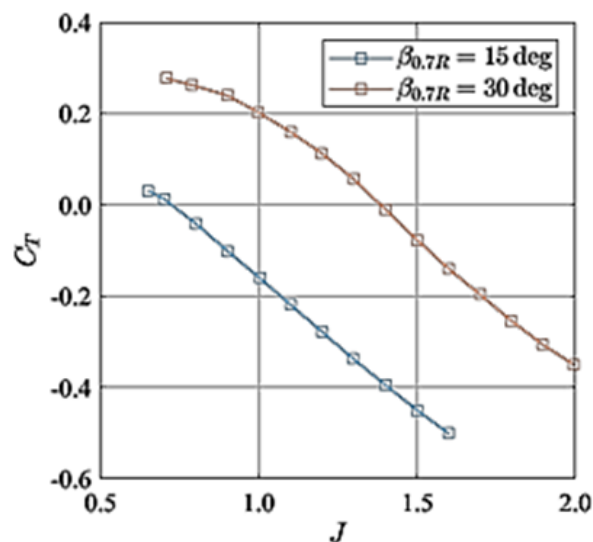


Figure 5.5: Thrust coefficient curves of the TUD-XPROP for blade pitch angles $\beta = 15^\circ$ and $\beta = 30^\circ$.

Table 5.1: Test Matrix for Run 1.

Run 1 (30 m/s)				
Test no.	V [m/s]	J [-]	rps _{prop} [Hz]	rps _{wt} [Hz]
1	0	-	0	0
2	30	0.8	92.27	5.7
3	30	1.0	73.82	5.8
4	30	1.2	61.52	5.9
5	30	1.4	52.73	5.9
6	30	1.6	46.14	6.0
7	30	1.7	43.42	6.0
8	30	1.8	41.01	6.0
9	30	1.9	38.85	6.0
10	30	2.0	36.91	6.0

Table 5.2: Test Matrix for Run 2.

Run 2 (20 m/s)				
Test no.	V [m/s]	J [-]	rps _{prop} [Hz]	rps _{wt} [Hz]
1	20	0.6	82.02	3.8
2	20	0.8	61.52	3.9
3	20	1.0	49.21	4.0
4	20	1.2	41.01	4.0
5	20	1.4	35.15	4.0
6	20	1.6	30.76	4.1
7	20	1.7	28.95	4.1
8	20	1.8	27.34	4.1
9	20	1.9	25.90	4.1
10	20	2.0	24.61	4.1

Table 5.3: Test Matrix for Run 3.

Run 3 (30 m/s)		
Test no.	V [m/s]	rps _{motor-1P} [Hz]
1	0	123.03
2	0	92.16
3	0	73.76
4	0	61.52
5	0	52.73
6	0	46.14
7	0	43.42
8	0	41.01
9	0	38.85
10	0	36.91

Table 5.4: Test Matrix for Run 4.

Run 4 (20 m/s)		
Test no.	V [m/s]	rps _{motor-1P} [Hz]
1	0	82.02
2	0	61.52
3	0	49.21
4	0	41.01
5	0	35.15
6	0	30.76
7	0	28.95
8	0	27.34
9	0	25.90
10	0	24.61

Table 5.5: Test Matrix for Run 5.

Run 5		
Test no.	V [m/s]	rps _{wt} [Hz]
1	20	4.02
2	25	4.97
3	30	5.92
4	40	7.78
5	50	9.65

5.4.1. Similarity of Test Conditions

In the field of aeroacoustics, the local Mach number is considered the most important similarity parameter [16]. The Reynolds number is an important similarity parameter for aerodynamic performance. The similarity can be shown by determining the scalable tip Mach number and the Reynolds number at each test condition. By comparing the similarity of these parameters at each test condition, it is possible to gain insight into how the experiment relates to a full-scale propeller in real-life conditions and to assess the extent of scaling required for comparison with actual flight conditions.

The helical tip Mach number of a propeller is a combination of the rotational speed of the propeller and the freestream velocity or speed with respect to the surrounding air in the wind tunnel. The Mach number is calculated using the formula presented in Equation 4.2. The helical tip Mach number is then calculated in Equation 5.2. The Reynolds number is defined in Equation 4.1.

$$M_h = \sqrt{M_\infty^2 + M_T^2} = \sqrt{M_\infty^2 + \left(\frac{\omega \cdot r}{c}\right)^2} \quad (5.2)$$

The helical tip Mach number and the Reynolds number at each test condition are calculated and illustrated in Figure 5.6. It is observed that tests at higher thrust coefficients exhibit higher Mach numbers than tests at lower thrust coefficients, as the rotational speed varied to achieve the variation in thrust. Scaling in tip Mach number significantly impacts the amplitude of the generated noise, and in the current setup, it also affects the frequency. The tip Mach numbers in the current study vary from 0.16 at negative thrust to 0.35 at positive thrust. However, it is important to note that full-scale propellers in actual flight operate at much higher tip Mach numbers, with values reaching up to 0.8 or higher. Thus, all the test conditions fall short of the actual flight Mach numbers.

The test conditions with higher thrust coefficients (lower advance ratio) are found to be closer to the actual flight Mach numbers than those with lower thrust coefficients. This implies that the sound levels of those conditions are more representative of the full-scale propeller at the scaled distance and frequency, assuming similar loading and propeller geometry. The tip Mach number has a strong positive correlation with the magnitude of the radiated noise [54]. When scaling the tip Mach number up to actual flight conditions, the power of the noise will increase due to the increased loading. This means the noise measured at negative thrust will increase more than at positive thrust when scaled to the same tip Mach number. At Mach numbers higher than 1, shock waves can occur, which were not simulated in this experiment. Additionally, higher tip Mach numbers can also increase the tip-vortex interaction, which is a significant source of broadband noise.

To achieve a more accurate representation of actual flight conditions, it is recommended to maintain a constant tip Mach number throughout the tests in future studies. The varied tip Mach number in the current study makes the extent to which the frequencies are scaled differently for every thrust setting. Recommendations for increasing the similarity in Mach number between the test and actual flight conditions can be found in chapter 9 of this report.

The Reynolds number is a crucial parameter that determines the degree of viscous effects around the blades, affecting the loading on the propeller. In the current study, the Reynolds number also varied between the test conditions, thus influencing the propeller's performance. The Reynolds numbers vary from $Re_c^{0.7R} = 0.8 \cdot 10^5$ at negative thrust to $Re_c^{0.7R} = 1.9 \cdot 10^5$ at positive thrust. It should be noted that these values are significantly lower compared to actual flight conditions. Under these conditions, viscous forces dominate, leading to higher drag due to increased surface friction, negatively impacting the propeller's performance.

At lower Reynolds numbers, the boundary layer around the blades is relatively thicker, resulting in an increased probability of flow separation. This can lead to an increase in broadband noise. However, when the Reynolds number is scaled up to real-life conditions, the boundary layer becomes relatively thinner, and flow separation is delayed. The blades' loading increases, leading to an increase in tonal propeller noise generation.

The data presented in chapter 7 are non-A-weighted noise levels. As the frequency shifts with respect to full-scale propellers, it is not appropriate to apply A-weighting directly. Instead, it is recommended that the data should be scaled first, and the A-weighting should be applied subsequently. This approach ensures that the A-weighting is applied correctly and accurately reflects the noise characteristics of the propeller. It is important to note that this process is not trivial in this case, as the Mach number differs for each condition. Recommendations for future research that make it easier to use the data for scaling purposes are provided in chapter 9 of this report.

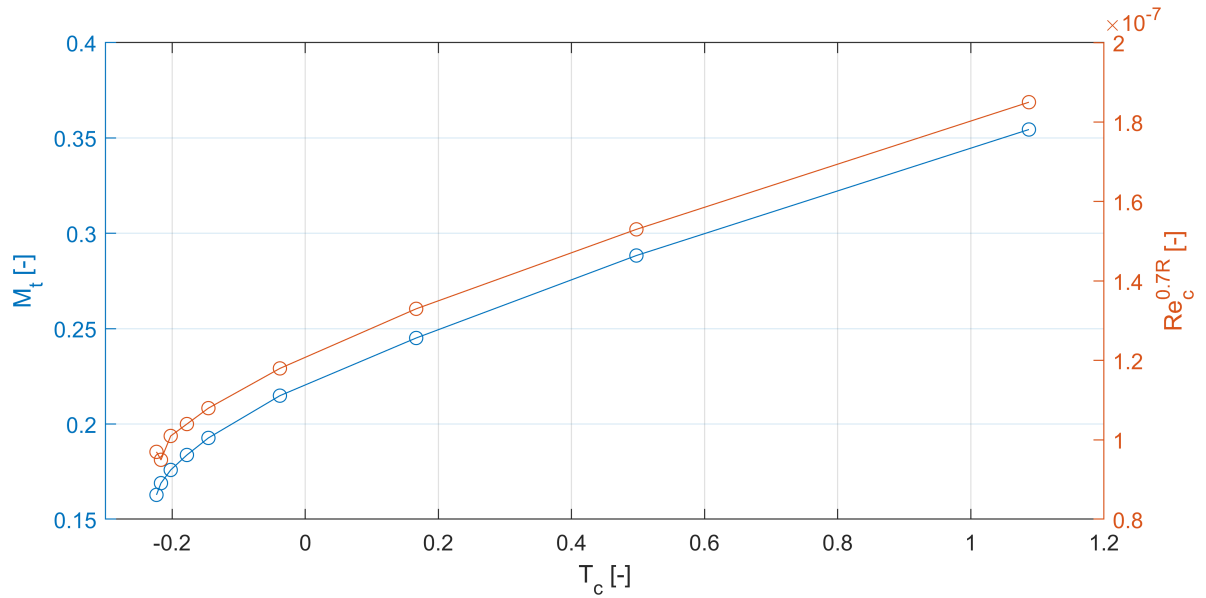


Figure 5.6: Similarity parameters tip Mach number and Reynolds number for thrust setting where $V = 30$ m/s.

6

Data Processing

Aeroacoustic wind tunnel tests can become quite challenging when one noise source is to be analyzed, given that microphones record every noise source generated by the entire system in the environment. Signal processing will help isolate the wanted signal, but this is a complex process and not always successful. The wind tunnel affects sound waves and their propagation toward the microphones, and background noise and reflections can disturb the signal. Figure 6.1 presents a flowchart that provides an overview of the processing methods discussed in this chapter. The data that was provided by the wind tunnel experiments are shown as inputs for the signal processing methods in blue.

This section covers the methodology of the third part of the research framework, the data processing. The data will be processed using Matlab. Matlab is the most suitable for this purpose, as it contains ready-to-use packages for processing the data. It also has the ability to show the results graphically. During data processing, the main objective is to isolate and quantify the dominant noise sources or to quantify the change of those noise sources with the variation of the thrust mode.

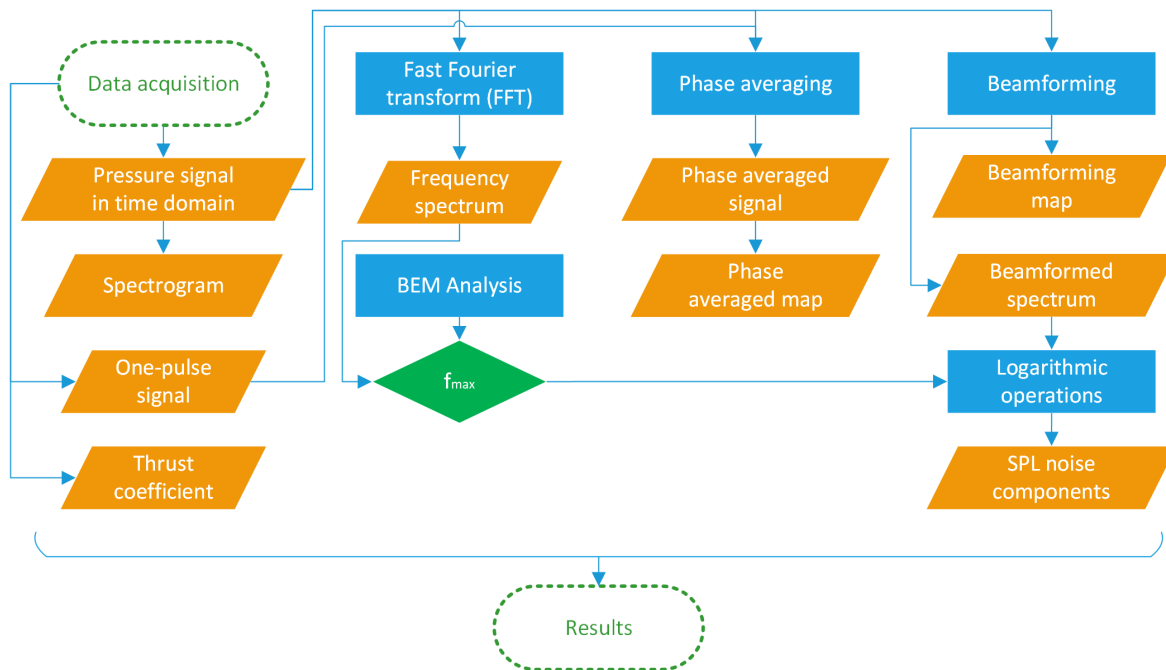


Figure 6.1: A flowchart presenting an overview of the various signal processing methods employed, along with their inputs and outputs.

6.1. Noise Signal in Time Domain

The data resulting from the acoustic measurements are raw and are time-domain-based data. The recordings can be directly plotted as shown in Figure 6.2. The plot shows an example of one of the microphones for two test settings, run 1 test 2 ($V_\infty = 30$ m/s, $J = 0.8$) mic 1 and run 2 test 1 ($V_\infty = 20$ m/s, $J = 0.6$) mic 1. The recorded sound pressure was measured over 30 seconds with a sampling frequency of $51.2 \cdot 10^3$ Hz. The signal from run 1 has a larger amplitude than from run 2. This is expected as the wind speed is larger, and with a constant advance ratio, the angular frequency is higher. This results in higher amplitude sound waves from both the wind tunnel and the propeller. The root-mean-square pressure value is, in fact, double for run 1 with respect to run 2. However, the microphone calibrations have not been applied yet. This will be done later in section 6.2.

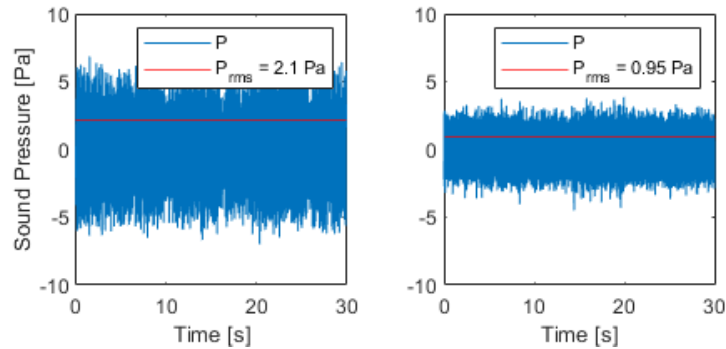


Figure 6.2: Time signal of microphone 1 and its root-mean-square of run 1 (left) and run 2 (right).

Spectrograms show the signal's power at each frequency as a function of time. Similarly to the previous plot, one microphone is shown for two test cases as an example in Figure 6.3. The two left plots show the power over the frequencies between 0 and 1500 Hz. It is observed that the horizontal lines stay constant over time. The power over the frequencies should stay constant over time, as the test conditions have been kept constant during the measurements. The color bar shows negative power values as these are relative values. Some frequencies approaching zero show higher amplitudes. The right plots show a close-up of the left ones in a region where higher power is plotted. For plot b, a dark red line is visible around 34 Hz, which is the BPF of the wind tunnel fan during this run. For d, this should be around 23 Hz, although this line is less defined. This could be due to disturbances of other noise sources and a lower tonal noise source from the fan, as it spun at a lower speed.

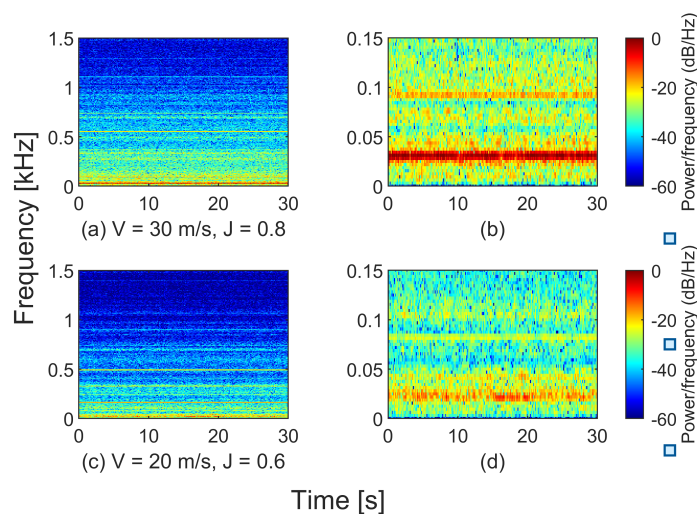


Figure 6.3: Spectrograms of average signals for run 1 (a), close-up of run 1 (b), run 2 (c), and a close-up of run 2 (d) over 30 seconds.

6.2. Microphone Sensitivity and Calibration

For the voltage signals to be converted to the correct pressure levels, microphone calibrations were performed for each microphone. Noise waves vibrate the microphone's diaphragm, which is then converted into electrical currents in volts [45]. The sensitivity of a microphone is an important aspect when it comes to its calibration. It is the ratio between the sound pressure input and the electrical output of the microphone. A higher sensitivity means more volts are measured per pascal. The sensitivity is commonly expressed as the transfer factor millivolts per pascal. Calibration is performed by exposing each microphone to a known input. Generally, a 1 kHz pure tone at 74 dB or 94 dB sound pressure level, equivalent to 0.1 Pa or 1 Pa pressure respectively [56]. The hearing of a human person works logarithmically. Therefore, the microphone sensitivity is often expressed in dB. Equation 6.1 converts the transfer factor in millivolt per pascal into dB relative to 1 volt per pascal [45].

$$S_{dBV} = 20 \log_{10} \left(\frac{TF_{mV/Pa}}{1000 mV/Pa} \right) \quad (6.1)$$

The calibrations for this research were performed using a G.R.A.S. 42AA pistonphone with a calibration level of 94 dB (reference sound pressure 20 μ Pa) at 1 kHz and a sampling frequency of 51200 Hz for the microphones in the wall and floor array with a total of 63 microphones. The calibration gives the sensitivity of each microphone in mV/Pa with an uncertainty level of 0.09 dB. This is used to convert the measured voltage of the experiments into pressure in pascal by dividing the voltage in mV by the sensitivity in mV/Pa. The calibration factor for each microphone is shown in Figure 6.4. The five red bars are microphones from the floor array, and the blue bars are microphones in the wall array. There is no bar visible at number 48, as this microphone input number was used for the 1P-signal to measure the angular frequency of the shaft, as will be discussed in section 6.3.

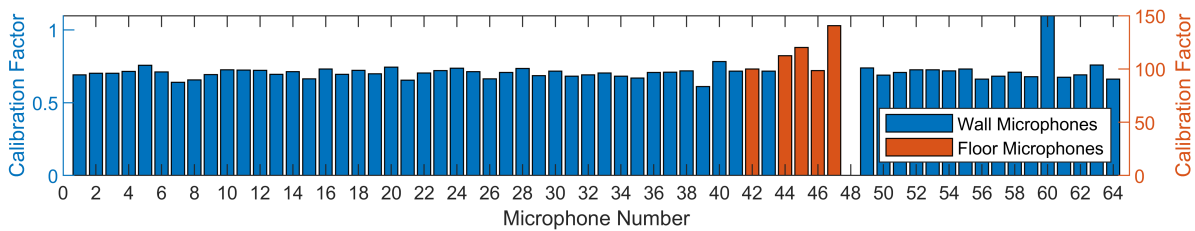


Figure 6.4: Microphone calibration factors for a 1 kHz tone at 94 dB.

In the frequency spectrum, which will be discussed in section 6.4, it becomes clear how important calibration of microphones is. Figure 6.5 shows a raw signal and a calibrated signal converted into the frequency spectra and to sound pressure levels. The difference between the two plots is 3.2 dB, which is a large difference if it is kept in mind that decibels are logarithmic and that a difference of 3 dB equals the doubling of the sound energy.

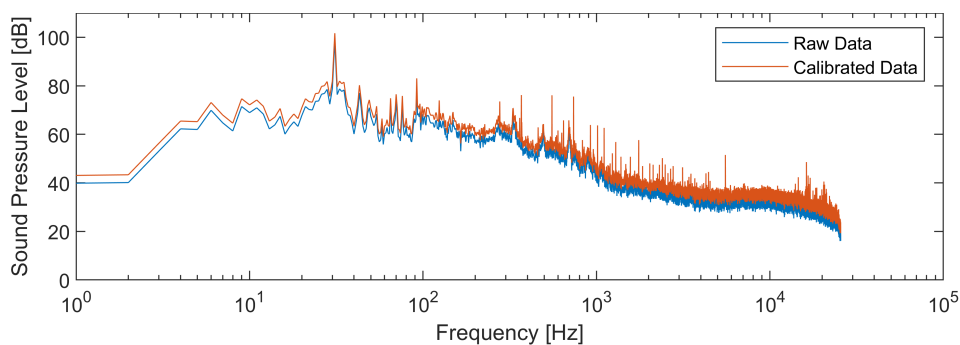


Figure 6.5: Comparison between raw data and calibrated data in the frequency domain for run 1 test 2 mic 1.

6.3. Angular Frequency

A one-pulse signal is used to record the actual rotational speed of the propeller shaft. The measurement device is placed with a sender and receiver on the propeller shaft and in the nacelle. When the shaft rotates, it records a pulse signal every time the sender passes the receiver. This gives an accurate measurement of the time between each rotation of the propeller. The pulse signal, 1P signal, is processed by finding the peaks in the signal and calculating the rotational speed of the propeller using the time between each peak. Figure 6.6 shows the first 0.1 second of a 1P signal of run 1 test 2 as an example. The distances are converted into the rotational speed of each revolution, showing that every revolution has an angular frequency of around 92 Hertz. The average angular frequency of 92.2707 corresponds with the angular frequency on the test matrix in Table 5.1, 92.27. The blade passing frequency, BPF, can be calculated based on the 1P signal using Equation 6.2.

$$BPF_{1P} = n_{1P} \cdot B \quad (6.2)$$

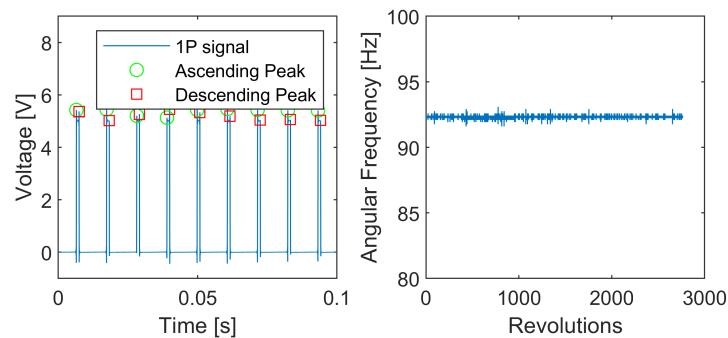


Figure 6.6: Example of a 1P signal with its located peaks (left) and the angular frequency (right).

6.4. Fourier Transformation

Sound or noise is measured by using microphones in the time domain. The sound waves pass the microphone's membrane, and the pressure changes are measured over time. The output signal is, therefore, in the time domain. The Fourier transform is a general method used to convert a signal in the time domain to the frequency domain, as shown in Equation 6.3. The frequency domain is used to gain insight into the signal from the spectral point of view instead of the time domain. Figure 6.7 clarifies these different points of view. It shows the power for each frequency, which is easier to observe for applications with signal sources related to specific frequencies.

$$F(\omega) = \frac{1}{2\pi} \int_{-\infty}^{\infty} f[T] \cdot e^{-i\omega t} dt \quad (6.3)$$

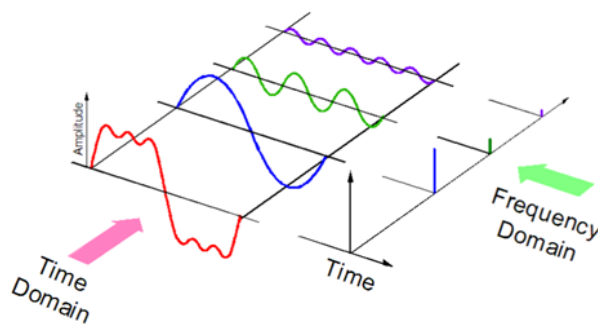


Figure 6.7: Perspectives of the time domain and the frequency domain [57].

6.4.1. Fast Fourier Transform

The input signal for a Fourier transform is a continuous time domain function converted into a continuous frequency domain function. However, the recorded signals are discrete time signals. The fast Fourier transform (FFT) is designed to convert discrete time domain data into discrete frequency domain data. This section will provide an intuitive understanding of the fast Fourier transform. Entire textbooks exist about the mathematics behind these methods. This thesis will only touch upon the main points to get a basic understanding. The fast Fourier transform (shown in Equation 6.4) is commonly used for converting digitized waveforms, giving n number of frequency domain points for n number of time domain points. Therefore $k=x$ in Equation 6.4.

$$F[k] = \sum_{n=0}^{N-1} f[n] \cdot e^{-i2\pi k \frac{n}{N}} \quad (6.4)$$

6.4.2. Aliasing, Picket Fence, and Scallop Loss

The frequency domain resulting from the FFT is symmetric due to the alias, which is a mirrored image of the frequency domain about the frequency that is half of the sampling frequency, $f_s/2$, also called the Nyquist frequency. It is common practice to hide the alias region in the frequency domain.

6.4.3. Spectral Leakage, Window Functions, and Overlap

The frequency resolution, Δf , is equal to the sampling frequency divided by the number of data points, f_s/N , or frequency bin width. In many cases, the frequency resolution will not be an exact integer of the frequency of the input signal. The input signal frequency falls between two frequency points in the frequency domain, as shown in Figure 6.8. In this case, there will be spectral leakage, which means that the energy at one frequency is smeared over multiple neighboring frequency bands. As the energy is 'lost' to neighboring frequencies, the peak in the spectrum might be significantly lower than the actual peak, and the peak will look wider in the base. The lower peak in the spectrum is called the picket fence effect, while the smearing of energy over other frequencies is called the scallop effect or scallop loss [10]. Spectral leakage is a loss in accuracy due to processing and is indistinguishable from noise near the signal frequency.

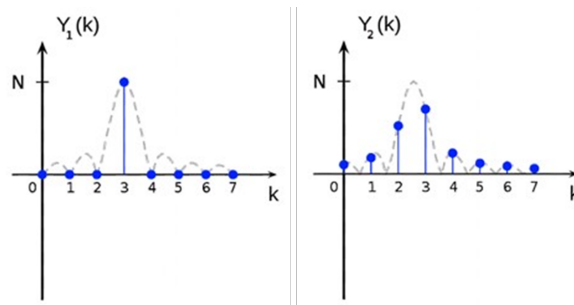


Figure 6.8: Spectral leakage effect where f_{in} equals an integer multiple of δf (left) and f_{in} does not equal an integer multiple of Δf (right).

The FFT assumes that the time domain signal continues infinitely in time. This is not the case for recorded signals. Therefore, the FFT copies the signal and repeats it infinitely. In most real cases, a discontinuity in the sampled waves will occur where at the endpoints, causing spectral leakage. Window functions are applied to the signal to minimize error sources, such as the spectral leakage effect due to the discontinuity at these points. Windowing can eliminate discontinuity at the endpoints of the samples. Windowing is a time domain function that shapes the signal, as shown in Figure 6.9. Choosing the proper window function will force the signal towards zero at each start and end of the signal, eliminating discontinuity. It has to be taken into account that the length of the window affects the frequency resolution. The larger the window, the higher the frequency resolution is, which serves a narrower lobe width. The Hanning window is the most used window function, which is adequate for 95% of the cases. However, many other window functions exist for particular needs [39].

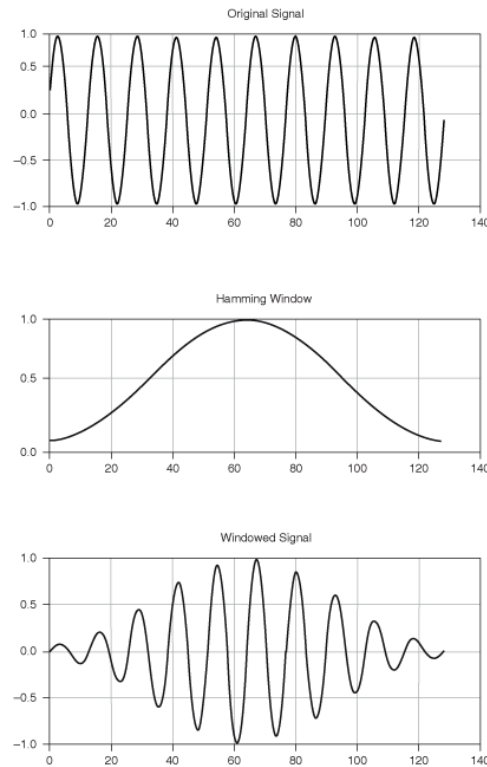


Figure 6.9: Hamming window applied on a signal with 0% window overlap [39].

Consequently, depending on the window used, part of the signal is reduced to zero. Some information from the recordings is being canceled. This can be resolved by applying a window overlap. An overlap of 50% of the number of samples in a window is a common overlap in signal processing. With overlapping windows, the start and endpoints do not meet at the same position, and the second window starts before the first window ends. This way, signal loss is reduced as no part of the signal is reduced to zero.

6.5. Frequency Analysis

For the frequency analysis, the time domain signals with a duration of 30 seconds and a frequency rate of 51200 Hz are converted to the frequency domain using the fast Fourier transform. Using Matlab, Welch's power spectral density estimate was applied to the calibrated data of each microphone for the conversion. With Welch's method, the signals were split into 400 Welch blocks multiplied by the Hanning window function with an overlap of 50%. The 'pwelch' function in Matlab returns a power spectral density (PSD) estimate using Equation 6.5 and Equation 6.6 [58].

$$Y[i] = \frac{1}{N} FFT x[i]w[i] \quad (6.5)$$

$$P_{yy}[0] = \frac{Y[0] \cdot Y[0]^*}{NG \cdot f_{bin}} \quad \text{and} \quad P_{yy}[i] = \frac{2 \cdot Y[i] \cdot Y[i]^*}{NG \cdot f_{bin}} \quad \text{for } i < 0 \quad (6.6)$$

The spectral power will be integrated. Therefore the PSD is normalized for integration purposes. For the value to be integrated over the frequency bin, Equation 6.6 will become Equation 6.7. This output will give accurate integration values for the overall sound pressure level.

$$P_{yy}[0] = \frac{Y[0] \cdot Y[0]^*}{NG} \quad \text{and} \quad P_{yy}[i] = \frac{2 \cdot Y[i] \cdot Y[i]^*}{NG} \quad \text{for } i < 0 \quad (6.7)$$

For the output in Matlab, this means that the PSD returned by the 'pwelch' function should be multiplied by the frequency bin width for integration purposes over a frequency range [58].

The frequency spectrum of each microphone is plotted in Figure 6.10. The floor microphones in yellow show significantly higher SPL over a wide range of frequencies. The large amplitude of broadband noise is because the floor microphones are placed much nearer to the test section wall and the air-flow. Near the walls, the (turbulent) boundary layer of the flow causes pressure fluctuations, resulting in broadband pressure levels for the affected microphones. The floor microphone measurements have a lower signal-to-noise ratio, which means degrading the noise content. The measurements of the floor microphones were discarded from this point on.

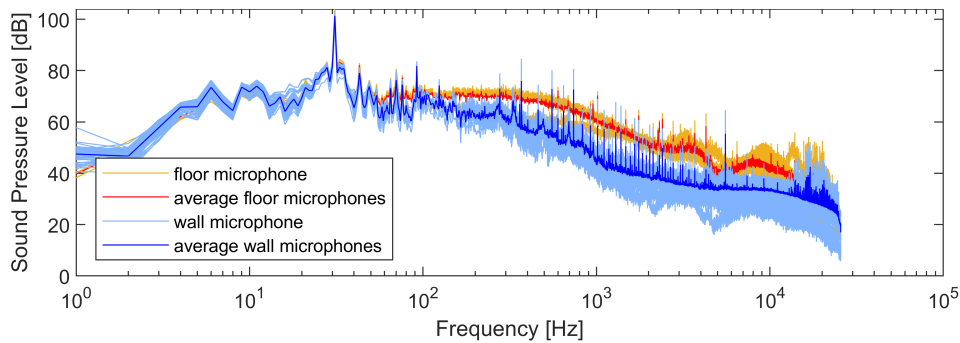


Figure 6.10: Example averages of spectra for wall and floor microphones for run 1 test 2.

The spectrum in Figure 6.11 shows the sound pressure level (SPL) versus the frequency. These spectra are plotted in dimensional form to show the first preliminary results. The average spectra of all the microphones for every thrust condition are plotted. The background noise, the corresponding wind tunnel noise measurements (run 5 for $V = 30$ m/s), and the motor noise measurement (for negative thrust) are also plotted for the frequency spectra of the measurements. It is observed that the peaks with the highest sound levels occur in the low-frequency region. The most significant peaks are positioned at frequencies that match the BPF of the wind tunnel fan (BPF_{wt}), varying from 34.2 Hz to 36.0 Hz, even though the wind speed in the tunnel was constant during every run. The variation in frequency is explained by looking at the thrust component, measured by the six-component balance in the direction of the wind. At lower advance ratios, the propeller generated positive thrust in the test section, accelerating the flow. This way, the wind tunnel fan could maintain the wind speed at a lower fan speed and thus a lower BPF_{wt} . The different frequencies throughout the tests equal the BPF_{wt} . As the wind tunnel noise dominated the low-frequency region, a high-pass filter was applied to the signal at $f = 100$ Hz.

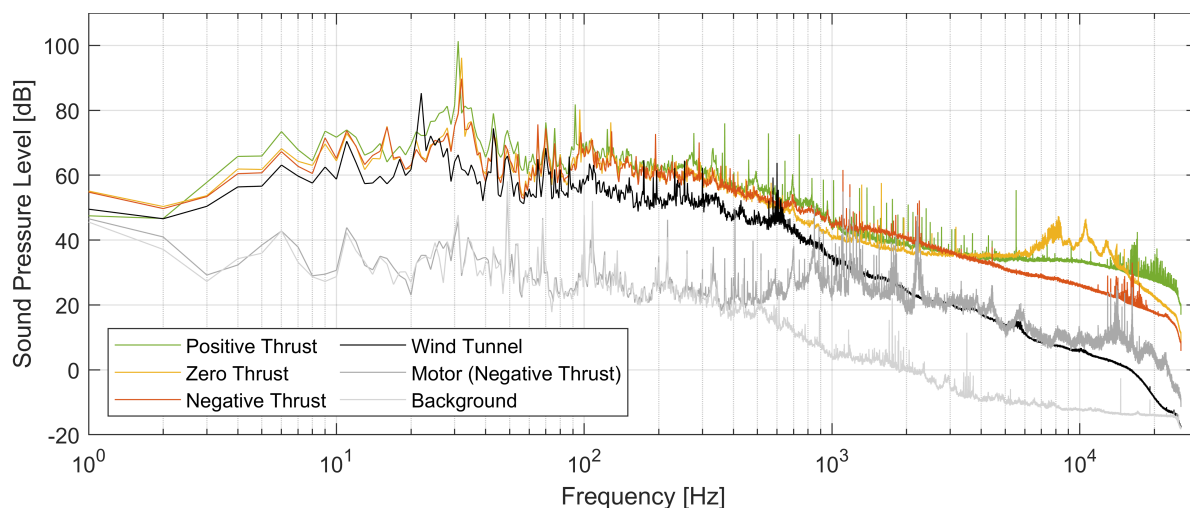


Figure 6.11: Frequency spectra for positive, zero and negative thrust for $V = 30$ m/s, averaged over all microphones ($\Delta f = 1$ Hz).

The dominant noise source of the wind tunnel is at low frequencies. Some discrete tones from the wind tunnel exceed the broadband floor of the three regimes. Sometimes, the spectrum shows peaks

at equal frequencies for all tests, e.g. at $0.4 \cdot 10^3$ Hz and $0.7 \cdot 10^3$ Hz, where the noise levels increase with the thrust setting. These tonal noise components are not related to the angular frequency of the propeller, as it does not change with the rotational speed of the propeller. This could be wind tunnel noise, propulsive noise, or aerodynamic noise sources unrelated to the propeller. Propeller-related discrete components would change with the angular frequency.

The zero thrust spectrum shows the lowest broadband noise ranging from $0.7 \cdot 10^3$ Hz to $3 \cdot 10^3$ Hz. The absolute thrust coefficient at zero thrust is lower than at positive and negative thrust. As the loading increases, both negative and positive thrust modes have exceeded these broadband noise levels in this region. It also shows that the negative thrust spectrum generated higher broadband noise in the same frequency range than the positive thrust spectrum.

In the high-frequency region, the positive thrust spectra show a significant bump. The diagnostic BEM analysis will be discussed in the next section. It will show that the airfoils with positive thrust settings have laminar separation bubbles (LSB) at the performed Reynolds number. LSBs result in a hump in the spectrum in the high-frequency region due to high-pitched noise. Paterson's law was used as a model to predict the minimum vortex shedding frequency caused by the LSB. However, the model contains limitations due to its simplifications and does not consider the airfoil shape. As a result, the exact frequencies related to the LSB could not be determined precisely as they did not fully match the spectra. To minimize the influence of the LSB during the analysis, a low-pass filter was applied with an estimated based frequency of $3 \cdot 10^3$ Hz.

The results of the BEM analysis are provided in section 7.3. Low energy of motor noise was recorded in the low-frequency region, as the background noise levels equal the motor noise measurements where $f \leq 250$ Hz. The motor noise is plotted for the rotational speed at negative thrust conditions. It is observed that the noise levels without load only have tonal components that exceed the broadband floor of the propeller measurements.

6.6. Blade Element Momentum Analysis

The appearance of a large hump in the high-frequency region of the spectra is suspected to be caused by laminar separation bubbles (LSB), which are known to generate noise at high-frequency regions [29]. The occurrence of laminar separation bubbles, a phenomenon where separation, transition, and reattachment take place, is highly dependant on the Reynolds number when Reynolds numbers are low ($Re_c < 5 \cdot 10^5$) [64]. The behavior of the LSB is not only affected by the Reynolds number but also by the geometry of the airfoil, angle of attack, and rotational speed [28]. All the performed tests are more susceptible to high-frequency noise sources caused by laminar separation bubbles, as they range between $0.8 \cdot 10^5$ and $1.9 \cdot 10^5$ at 75% of the chord. A blade element momentum analysis has been performed by simulating the test conditions to confirm the presence of an LSB. Different airfoil sections of the propeller TUD-XPROP blade were modeled using JavaFoil. These were then exported to Xfoil to analyze the flow around the airfoil with the test conditions of the acoustic measurements.

The screenshot shown in Figure 6.12 is the result of the analysis of the airfoil section at 40% of the chord with a wind speed of 30 m/s and an advance ratio of 0.8. This is the positive thrust region, where L/D shows to be positive. The solid yellow line shows the viscous analysis of the flow over the upper surface of the blade. The pressure distribution shows a bump at the location where the LSB is located. In the lower plot, the airflow is demonstrated over the airfoil, where it is visible that the flow separates and reattaches again downstream. The LSB appeared at different locations on the chord for different airfoil sections and for different advance ratios or rotational speeds. The hump moves towards the trailing edge and increases amplitude for increasing J , as described in literature [28]. The LSB was shown for every run in the positive thrust regime. When the angle of attack decreases and the thrust mode becomes negative, it is shown in Figure 6.13 that the flow over the upper surface is attached and the completely separated flow on the lower surface. For both wind speeds, the boundary layer separates at the lower surface around $r/R = 0.5$ for $J = 1.4$ and is fully separated on the lower surface of the entire blade for all the higher advance ratios.

The phenomena of the LSB appear at lower Reynolds numbers, which is not the case in actual airplane flights. The measured high-frequency noise is, therefore, not of importance for real flight cases. Frequencies above 3000 Hz are not considered for calculating broadband noise.

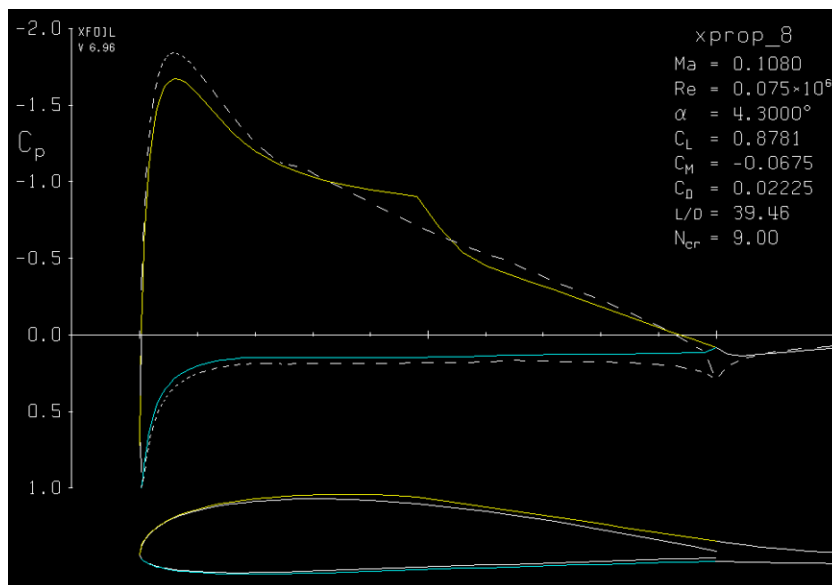


Figure 6.12: XFOIL screenshot of a C_p distribution for viscous (solid line) and inviscid (dashed line) analysis of the TUD-XPROP blade simulated in the conditions of run 2 test 2 at $0.4 r/R$.

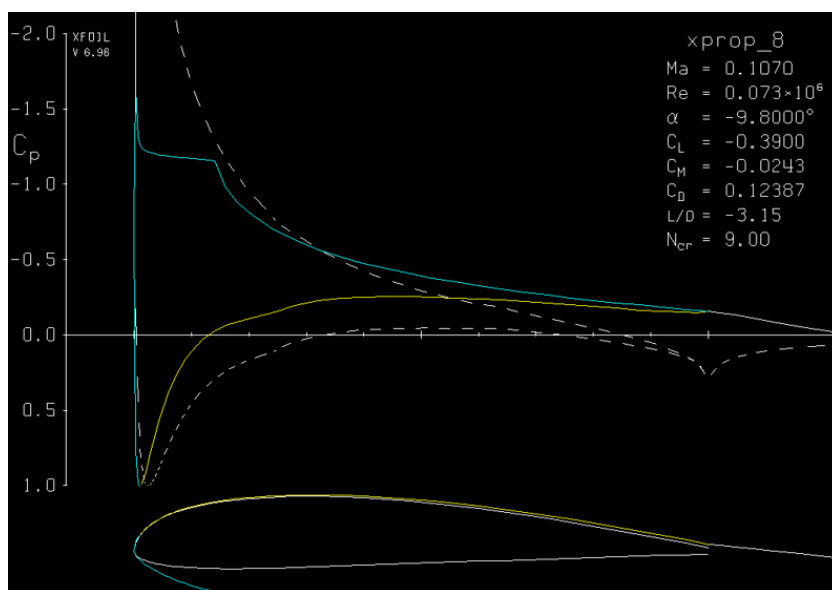


Figure 6.13: XFOIL screenshot of a C_p distribution for viscous (solid line) and inviscid (dashed line) analysis of the TUD-XPROP blade simulated in the conditions of run 1 test 8 at $0.4 r/R$.

6.7. Phase Averaging

Phase averaging is a processing technique that amplifies the rotational noise with respect to other noise sources. This can be done for each microphone signal to map the isolated noise for every microphone location. The measurement data was phase-averaged over the propeller rotation using the rotational speed calculated with the 1P-signal, see section 6.3. The rotational position of the propeller is determined for every point in time. The signal is then averaged over every revolution. The resulting signal is the averaged pressure signal at each rotational position of the propeller, as shown in Figure 6.14,

where the pressure signal is highlighted for microphone number 1.

The phase-averaged pressure signals are strong if a distinct tonal propeller noise was measured. However, if this noise source was masked mainly by interfering sources such as motor noise or sound due to reflections, the random phase shifts of those signals will average each other out. Also, a dominant broadband noise source can make the phase-averaged signal insignificant. This was the case for all other test conditions besides the most positive thrust case. Therefore, phase averaging did not lead to the desired outcome of isolating the rotational noise component of the propeller. Using the pressure RMS of each microphone, a map of the whole microphone array can be shown. The pressure RMS values for each microphone were converted to SPL, and the area between the microphone locations was interpolated and plotted. This contour plot shows the phase-averaged sound pressure levels of the array.

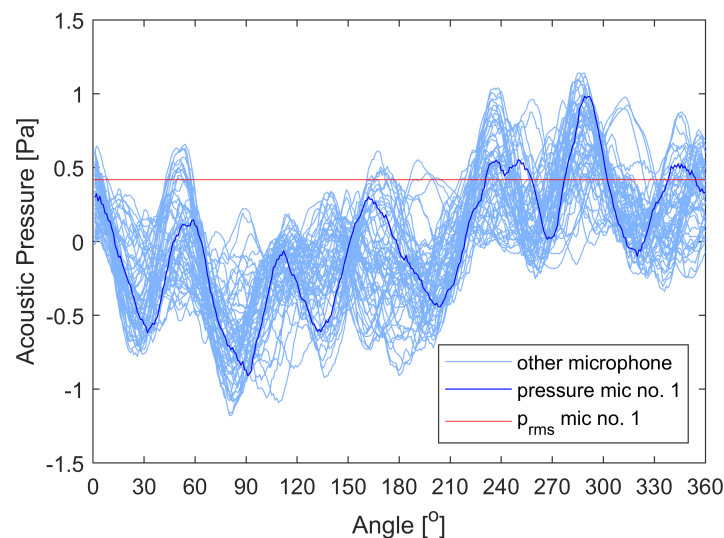


Figure 6.14: Phase averaged data of all microphones for one test case with one microphone signal highlighted and its pressure RMS value.

6.8. Beamforming

The phase-averaging method did not show significant pressure signals for tests other than the most positive thrust case. It can also not be used to derive the source locations of the measured signals at the microphone, as many factors influence the propagation of the sound waves. The boundary layer might diffract the noise or arrive at the microphone after reflecting against the test section wall, making it impossible to know the source location. Beamforming, also called spatial filtering, is one of the essential signal-processing techniques for applications where multiple sensors are used to receive signals. Figure 6.15 provides an example of the fundamental idea behind beamforming. Beamforming maintains the source signal from a specific location in space (source 1) while it conceals signals from other directions (source 2) that interfere with it [19]. These could be noise sources from other systems, such as wind tunnel propulsion, or reflections that are incoming from other directions than the source. The beamforming technique utilizes the fact that the different microphones have different locations. Therefore, the sound wave from one particular source will arrive at a different time at each microphone. The microphone signals can then be shifted relative to the travel distance from the wanted source to the microphone to synchronize those signals. At this point, the desired signals are in phase, contrary to other noise signals, which are out of phase. The signals of all 58 microphones are summed, and due to the source signal being in phase, this part of the signal will contain much more energy than the other source signals. When the signal is divided by the number of microphones to normalize the amplitudes, the interfering signals will have much lower amplitudes.

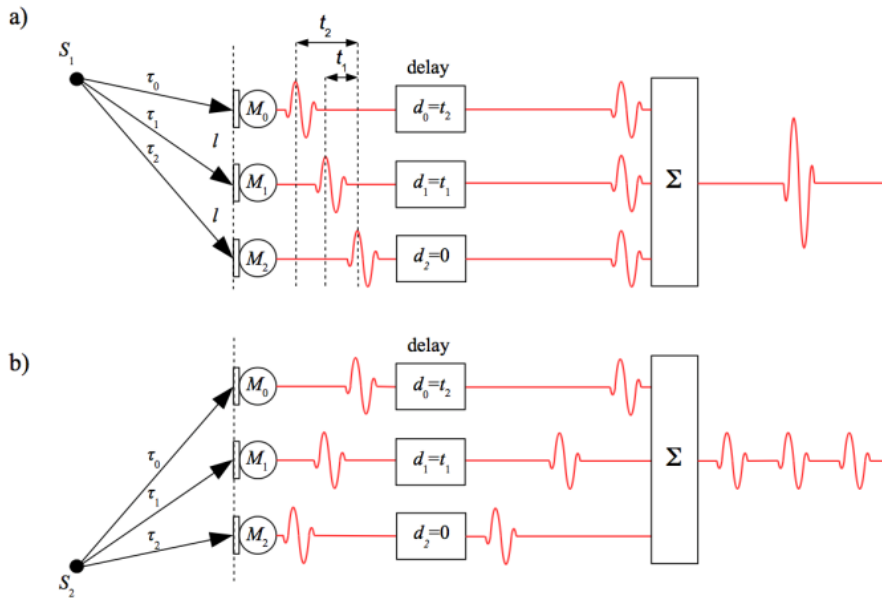


Figure 6.15: Beamforming effect on the target signal (a) and the interfering signal (b) [42].

Inverse Beamforming uses this principle inversely to locate noise sources at a defined plane. Inverse beamforming was used to plot the beamforming map to see the energy's location of the signal at a frequency in the rotational axis plane. A contour plot showing sound pressure levels in the plane of the propeller rotational axis. The region of integration (ROI) is set at a location in the plane, around the propeller, to integrate the noise levels from the beamformed data in that location. This is done at every frequency, resulting in a beamformed frequency spectrum.

$$\Delta\tau_n = \frac{n \cdot d \cdot \cos(\theta_s)}{c} \tag{6.8}$$

Figure 6.16 shows an example of a beamformed spectrum in orange and a non-beamformed spectrum in blue, as we have seen in section 7.2. The broadband noise levels diverge with frequency due to the higher resolution at higher frequencies. The fundamental BPF and its harmonics are marked, where the fundamental BPF sound pressure level did not change significantly, while the higher BPF multiples did. This can be due to the low resolution at the fundamental BPF or because the propeller noise was already dominant at the fundamental BPF before beamforming.

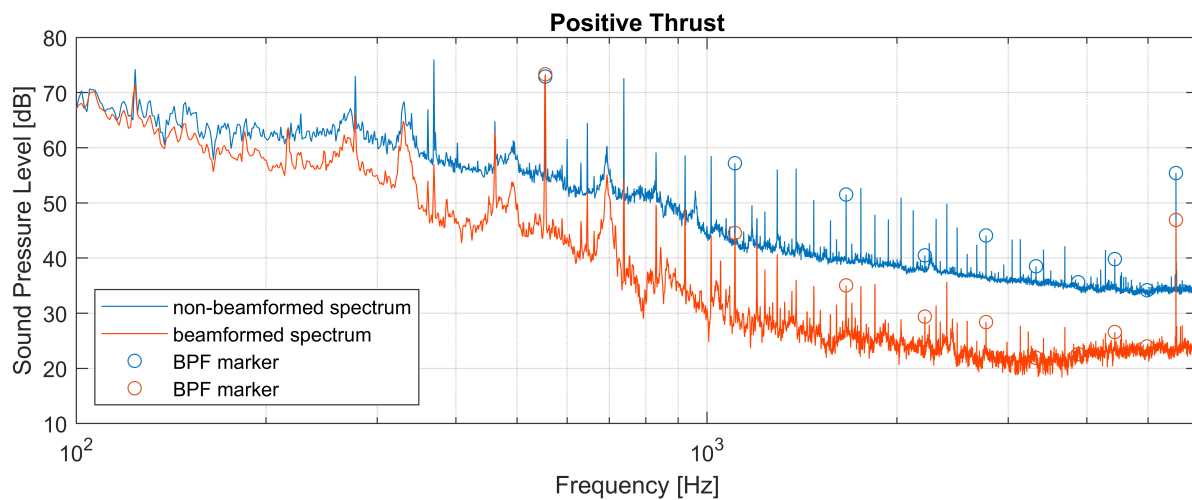


Figure 6.16: Non-beamformed and beamformed frequency spectrum for the positive thrust regime for \$V = 30\$ m/s (\$\Delta f = 1\$ Hz).

6.9. Broadband and Tonal Components

To quantify the isolated tonal and broadband components of the propeller noise in the beamformed spectra, first, the SPLs are calculated. The tonal and broadband components of the propeller noise will be compared between positive and negative thrust. A range of SPLs from the spectrum is summed at each BPF multiple from BPF-8 Hz to BPF+8 Hz to obtain the full power of the peak, including the power that might be lost to neighboring frequencies due to spectral leakage. These frequencies are summed at each BPF multiple. As the data is in decibels, which is logarithmic, the summation is performed using Equation 6.9. The same operation is performed on the beamformed spectra of the motor noise and the wind tunnel noise at each multiple of the propeller BPF. The motor and wind tunnel noise is subtracted from the propeller measurements at each BPF. The remaining SPL is the increase of the propeller measurements. The overall sound pressure level, OSPL, is calculated by summing the SPL of each BPF.

$$SPL = 10 \log_{10} \sum_{i=1}^n (10^{\frac{SPL_i}{10}}) \quad (6.9)$$

The noise generated by the motor is expected to show similar tonal components at the BPF multiples with equal or higher amplitudes at those frequencies when the motor is operating with the load of the propeller blades. The variation of frequencies or amplitudes when loads are applied to the motor is unknown. This will be further discussed in chapter 7. Broadband noise calculations are similar to tonal noise calculations. The spectra of the wind tunnel and motor measurements are subtracted from the propeller measurements, excluding the frequencies used to calculate the tonal components at the BPFs to avoid summing the tonal components. A low-pass filter was applied at $f = 3000$ Hz to avoid summing the high-frequency noise from the laminar separation bubble that appears at a low Reynolds number, as described in section 6.6. Real flight conditions are at a high Reynolds number. Therefore, the effect of the laminar separation bubble should not be included in the simulation results. Sometimes, the pressure levels during propeller measurements are lower than the combined motor and wind tunnel noise. This will result in negative pressure levels when they get subtracted, getting imaginary results when the log is taken of that value. To prevent this, the minimum pressure level was set to 1, which resulted in a minimum decibel level of 0 dB. This equals the minimum noise level the human ear can hear, a very low-energy insignificant noise level.

IV

Results and Discussion

7

Results and Discussion

This chapter presents the results of the acoustic measurements taken in the wind tunnel. The results are presented in graphical form and accompanied by a discussion of their interpretation. This analysis aims to gain insight into the relationship between the measured pressure fluctuations and the different operating conditions. For the conciseness and clarity of this chapter, results are only presented for the most positive, zero, and most negative thrust cases for the comparison of the propulsive and regenerative modes that relate to tests 2, 5, and 10 with advance ratios of 0.8, 1.4, and 2.0, respectively, for $V = 30$ m/s. This run contains the series of tests with the best signal-to-noise ratio due to the lower interference of the wind tunnel noise and the motor noise with respect to $V = 20$ m/s. The selected test cases are shown in Table 7.1. The full test matrices are found in section 5.4, and the extended results with plots for every test case can be found in Appendix A.

Table 7.1: Test matrix of the selected test conditions derived from Table 5.1.

Regime	Test no.	V [m/s]	J [-]	T_c [-]	β [°]	rps _{prop} [Hz]	rps _{WT} [Hz]
Positive Thrust	2	30	0.8	1.09	30	92.27	5.7
Zero Thrust	5	30	1.4	-0.04	30	52.73	5.9
Negative Thrust	10	30	2.0	-0.22	30	36.91	6.0

7.1. Thrust Coefficient

The six-component balance was used to measure the absolute forces and moments on the model. The measurements are used to determine the thrust coefficient and show in which tests the propeller generated positive or negative thrust. The experimental setup did not include an internal load cell, which could have enabled the separation of the support beam's interaction effects from the propeller's wake. The propeller-off measurements corrected the forces on the structure of the setup by the freestream velocity. The results from the balance are plotted as normalized thrust coefficients in Figure 7.1. Equation 7.1 shows how the normalized thrust coefficient was defined. The plot shows that for $J \leq 1.2$, the propeller was operating at positive thrust condition, and for $J \geq 1.4$, the propeller was operating at negative thrust mode.

$$T_c = \frac{T}{\frac{1}{2}\rho V_\infty \pi \frac{D^2}{4}} \quad (7.1)$$

High thrust coefficients are observed at low advance ratios, where it flattens out at higher advance ratios and the absolute levels of the thrust coefficient are higher at positive thrust than at negative thrust

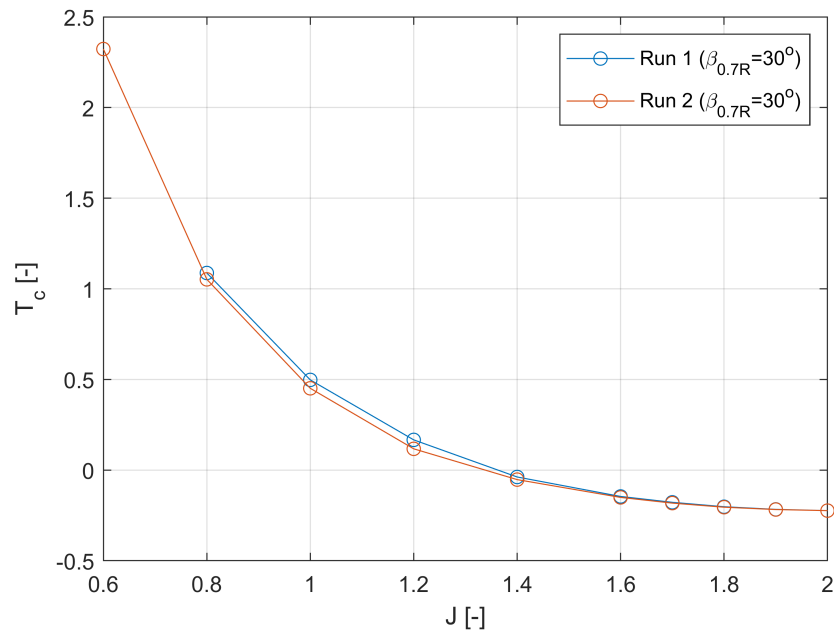


Figure 7.1: Normalized thrust coefficient derived from the six-component external balance.

7.2. Frequency Spectra

The frequency spectrum is obtained using a fast Fourier transform on the calibrated microphone data. The power density spectrum is converted into decibels' logarithmic sound pressure levels. The wind tunnel noise measurement can be seen as the baseline of the measurements. If the propeller measurements do not exceed the pressure levels of the wind tunnel noise measurements, the recorded noise can not be related to the propeller. These measurements include the noise of the wind tunnel system and noise from the model support structure and the nacelle. The same can be assumed from the motor noise measurements. The measurements without loads on the motor will be the minimum noise generated by the propulsion system. Suppose the propeller measurements do not exceed the summation of the wind tunnel noise and the motor noise measurements. In that case, the pressure levels are not a result of noise generated by the propeller. Overall, the spectra of the propeller-on measurements show a significant difference relative to the wind tunnel noise.

The three operating conditions were achieved by varying the advance ratio, resulting in variations in rotational speed, tip Mach number, and Reynolds number. The blade loading and propeller performance, therefore, varies for each case. As the wind tunnel noise dominated the low-frequency region, a high-pass filter was applied to the signal at $f = 100$ Hz.

In Figure 7.2, the spectra of the previous plots are shown with the frequencies divided by their BPFs. This results in spectra being presented in non-dimensional frequencies to better assess the different noise levels between the test conditions at the BPF and its multiples. The motor noise is normalized using the BPF of the test where $J = 2.0$, the negative thrust condition. The BPF ranges from 221 Hz for negative thrust to 554 Hz for positive thrust, and the plot shows the SPL in the spectra until the twelfth harmonic of the BPF for each regime. At the fundamental BPF, only positive thrust shows a significant peak. Other notable peaks at BPF multiples are observed at the fifth and tenth harmonic of the BPF. This coincides with the motor's discrete tones that exceed the measurements' broadband floor. In theory, the energy of a rotational propeller component decays with every BPF multiple. However, the noise levels at the fifth BPF are much larger than the three lower harmonic BPFs. The motor noise seems to be the agitator for this rise in sound levels at the fifth, tenth, and sometimes the eighth BPF multiple. Tonal noise components at the remaining BPF are relatively small or non-existent. Other discrete tones between BPF multiples spaced with one-sixth of the BPF were found and also coincided with discrete tones that the motor generates. It is, therefore, highly possible that these tones are also sourced from the motor or the drive system.

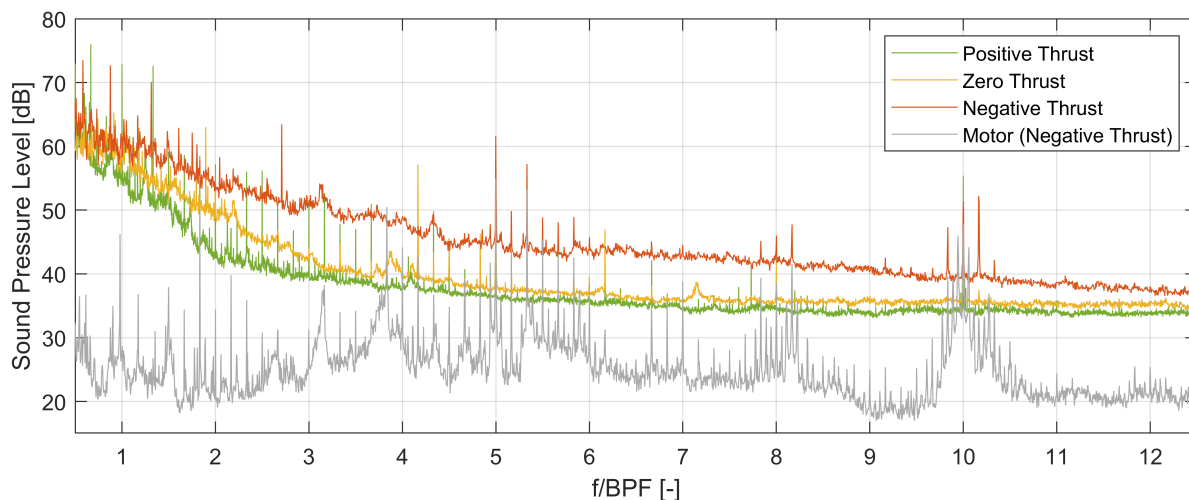


Figure 7.2: Normalized frequency spectra for $V = 30$ m/s ($\Delta f = 1$ Hz).

The broadband noise sources at negative thrust are significantly higher than for the two other thrust settings, and the efficiency at negative thrust was lower. The increase in broadband noise is explained by the separation of the boundary layer due to a sub-optimal condition of the propeller, generating random pressure fluctuations on the blades.

The motor noise spectra are shown for three rotational speeds in Figure 7.3, where the lowest angular velocity corresponds to the negative thrust condition during the experiment, the middle angular velocity to the zero, and the highest angular velocity to the positive thrust condition. The plot gives insight into the variation of motor noise with its angular velocity. The measurements were performed without assembled blades. No loading was applied on the shaft. The measurements include the propulsion system, shaft, bearings, and coupling. It is observed that the broadband noise increases with increasing angular velocity. Tonal components are expected to harmonize with the propeller's angular frequency as the motor's shaft rotates at the same angular velocity as the propeller. The magnitude of tonal components that match with the harmonics of the BPF of the propellers are inversely correlated with the angular velocity. This agrees with the discrete tones found in the propeller measurements, where the peaks at the fifth, eighth, and tenth BPF harmonic are more significant for negative than positive thrust. Thus, the rotational noise of the propeller at negative thrust measurements was more affected by the tonal motor noise than the positive thrust conditions due to the varied angular frequency that was lower at negative thrust conditions.

It is crucial to note that the motor noise measurements were taken with the propeller blades removed from the shaft. This is an essential consideration, as the presence of the blades may significantly impact the measured noise levels. Although the change in amplitude or the distribution of the spectral content of the noise is unknown, the tonal components associated with the multiple of the rotational speed are assumed to generate more noise with higher loads. The extent to which the amplitudes might increase is unknown, nor is the behavior of other tonal or broadband components. Negative and positive thrust forces on the shaft, bearings, and motor possibly generate different noise levels. Positive thrust creates a pulling effect on the shaft, and negative thrust creates a pushing effect on the shaft. The impact of these opposing forces on noise generation is not known. By subtracting the tonal motor noise levels at propeller BPFs from the propeller measurements, the contribution of the motor noise during the measurements is, at most, partially minimized and not canceled out. If the combined noise level of the motor noise and the wind tunnel noise at a certain BPF is not exceeded during the measurement, no propeller noise was measured at that frequency using the experimental setup in this research.

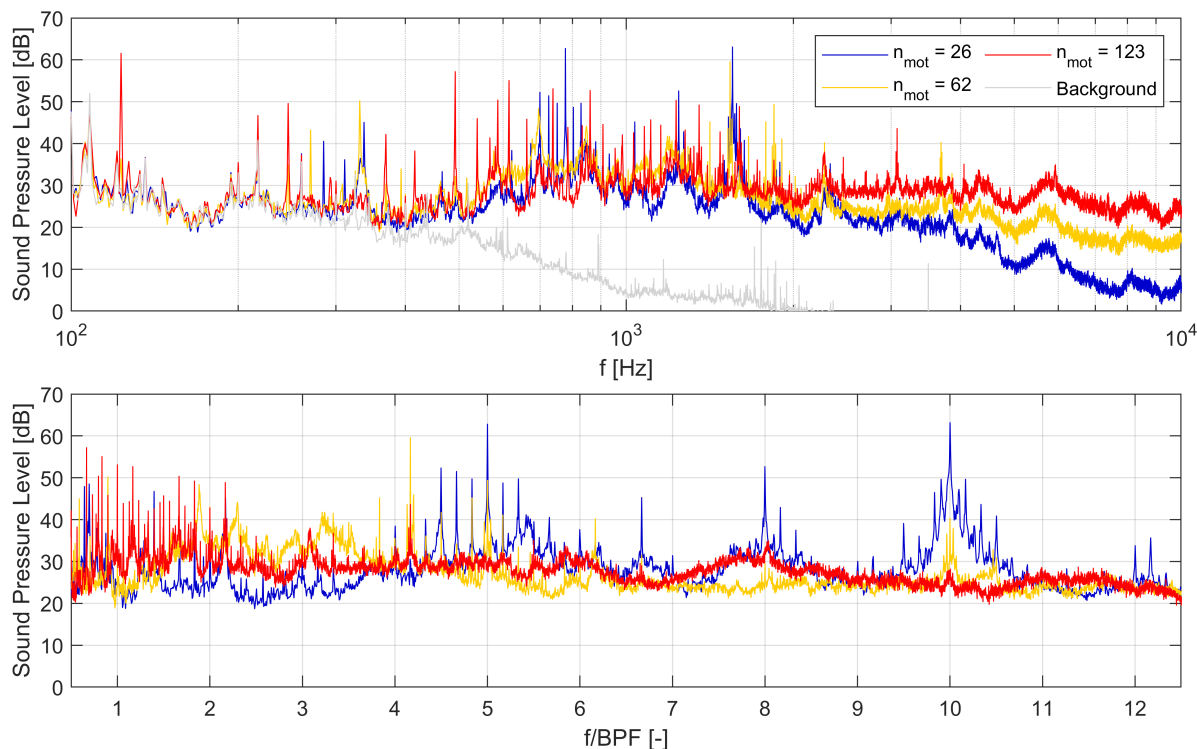


Figure 7.3: Frequency spectra ($\Delta f = 1$ Hz) of motor measurements (top), and normalized spectrum (bottom).

7.3. Blade Element Momentum Analysis

Due to the appearance of the high-frequency increase in the previously shown spectra, a diagnostic analysis was performed to confirm the presence of a laminar separation bubble at certain conditions of the experiment.

The blade element momentum (BEM) analysis resulted in the pressure distributions as shown in Figure 7.4. At positive thrust ($J < 1.4$), a laminar separation bubble (LSB) formed in the upper airfoil surface of the blade. An LSB is a phenomenon that occurs at low Reynolds numbers. The LSB would not appear in real flight, as the Reynolds number is much higher. The LSB causes a separation of the boundary layer, which forms turbulent structures in the flow. The turbulence induces pressure and velocity fluctuations on a small scale, therefore generating noise in the high-frequency region in the far field. This contributes to broadband noise in the high-frequency region as the turbulent flow is unsteady and chaotic, causing random fluctuations. This explains the large humps in the frequency spectra that were previously discussed. The LSB moves towards the trailing edge for advance ratios approaching zero thrust, where it bursts due to the decreasing angle of attack. The location of the LSB also varied for different blade sections. For higher r/R ratios, the LSB moved downstream due to the decreasing angle of attack and increasing Reynolds number at the blade sections. The appearance of LSBs at positive thrust mode agrees with the spectral frequency humps found in the high-frequency region for positive thrust, shown in Figure 6.11. At zero thrust, the lower surface boundary layer was attached for the blade sections where $r/R < 0.5$ and fully separated for $r/R > 0.5$. This is at the transition point of the positive and negative thrust regimes. The lower surface boundary layer was fully separated at all the blade sections for tests where the thrust was negative. Fully separated boundary layers lead to turbulent flow where random pressure fluctuations cause broadband noise. A turbulent flow generates more broadband noise than a laminar flow. The increase in broadband noise levels at negative thrust conditions with respect to positive thrust conditions was observed in the frequency spectra.

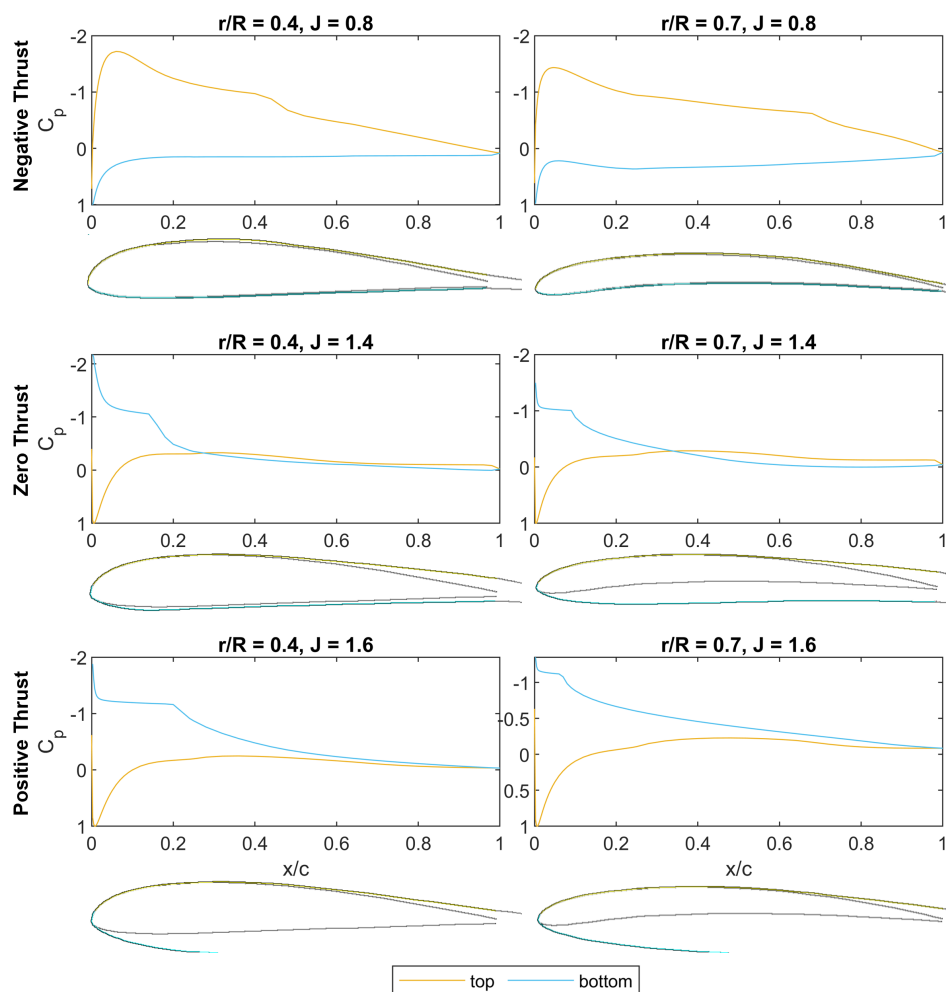


Figure 7.4: Pressure distribution for different thrust settings and blade sections where $V = 30$ m/s.

7.4. Phase Averaged Noise Levels

For the phase-averaged noise levels, measurement data were averaged over these pressure signals' over a full propeller rotation using the rotational speed calculated with the 1P-signal. The results of microphone no. 1 are shown as an example for each thrust setting where $V = 30$ m/s (Figure 7.5).

The figure illustrates the average pressure level as a function of the angular position of the propeller. Six blades pass during one rotation, altering the surrounding pressure with every pass. The positive thrust condition shows six-hilled pressure waves caused by the six propeller blades. Another tonal component at a lower frequency can be recognized if, for example, a component of only one wave cycle of a wave is observed for positive thrust. This means that the pressure changed with a frequency at one-sixth of the BPF, corresponding to $\frac{1}{6} \cdot \text{BPF} = 92$ Hz. This component was observed in the frequency spectra. The tests at higher advance ratios show much lower pressure levels. The six hills are also not very apparent for the remaining two conditions due to higher broadband noise or other noise sources that masked the rotational noise. Pressure levels can average each other out if they are not related to the BPF of the propeller due to random phase shifts, resulting in averages near zero. Low-pressure levels in the phase-averaged signals show the minimal contribution of tonal noise components measured by that microphone.

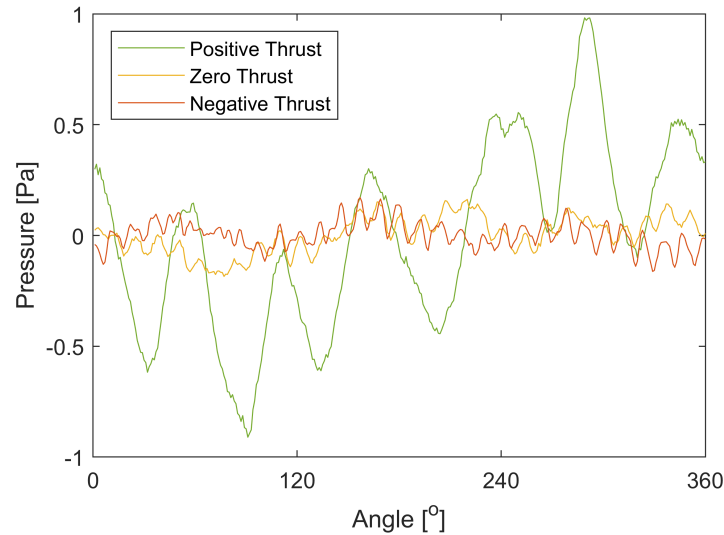


Figure 7.5: Phase average signal of microphone no. 1 for each regime for $V = 30$ m/s.

The phase-averaged signal was computed for each microphone, and the root mean square (RMS) was converted into sound pressure levels (SPLs). These are illustrated in Figure 7.6. The interpolated plots provide insight into how the amplitude of the phase-averaged signal was distributed over the wall array, which are pressure levels related to the angular frequency of the propeller. The phase-averaged signals at zero and negative thrust are insignificant compared to the positive thrust condition. The maps based on phase-averaged data cannot be observed as a noise source location, as it is unknown where the pressure waves arrived at each microphone. The sound levels can change significantly with the position in the near field due to circulating sound waves. The sound waves can be reflected against the hard test section walls or diffracted by the boundary layer over the blades before it arrives at the observing microphone. Therefore, phase averaging did not successfully locate propeller noise to isolate it from other noise sources, such as the motor and reflections. To gain further knowledge about the noise sources, beamforming was performed on the signals to isolate the propeller noise contribution to the signal. This is presented in the following section.

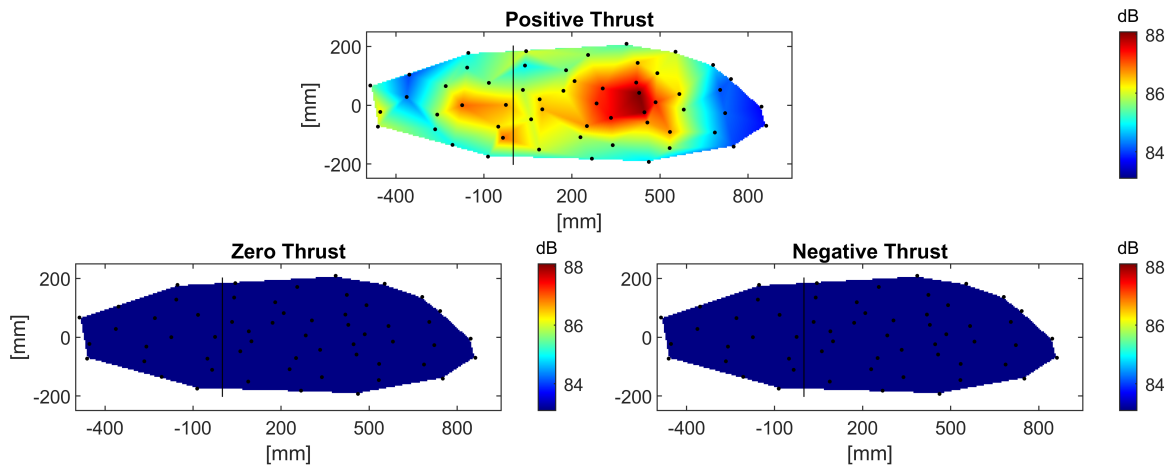


Figure 7.6: Interpolated contour plot of phase-averaged sound pressure levels of every microphone for $V = 30$ m/s with color bars showing a 5 dB range.

7.5. Noise Data from Inverse Beamforming

The inverse beamforming technique was used to integrate the noise levels over the region of integration at the propeller plane at each frequency and is expected to diminish noise sources coming from other directions, such as reflections and motor noise. The resulting beamformed spectra are plotted in

beamforming maps for several frequencies in SPL.

The frequency of the noise can impact the resolution of the beamforming technique. Figure 7.7 shows the beamforming maps nearest the first, fifth, and tenth BPF for positive thrust at the top and negative thrust at the bottom. The ranges of the color bars are different for each plot. Notably, the beamforming near the tenth BPF for positive thrust has a higher resolution than the beamforming map near the tenth BPF for negative thrust. At lower frequencies, the noise wavelength is larger, requiring the sensors in the array to be spaced further apart to accurately capture the longer wavelength noise, leading to a lower resolution for a fixed array design with respect to the case with higher wavelengths of interest. In the plots, this translates to a blob larger than the model, where different sources of sound merge.

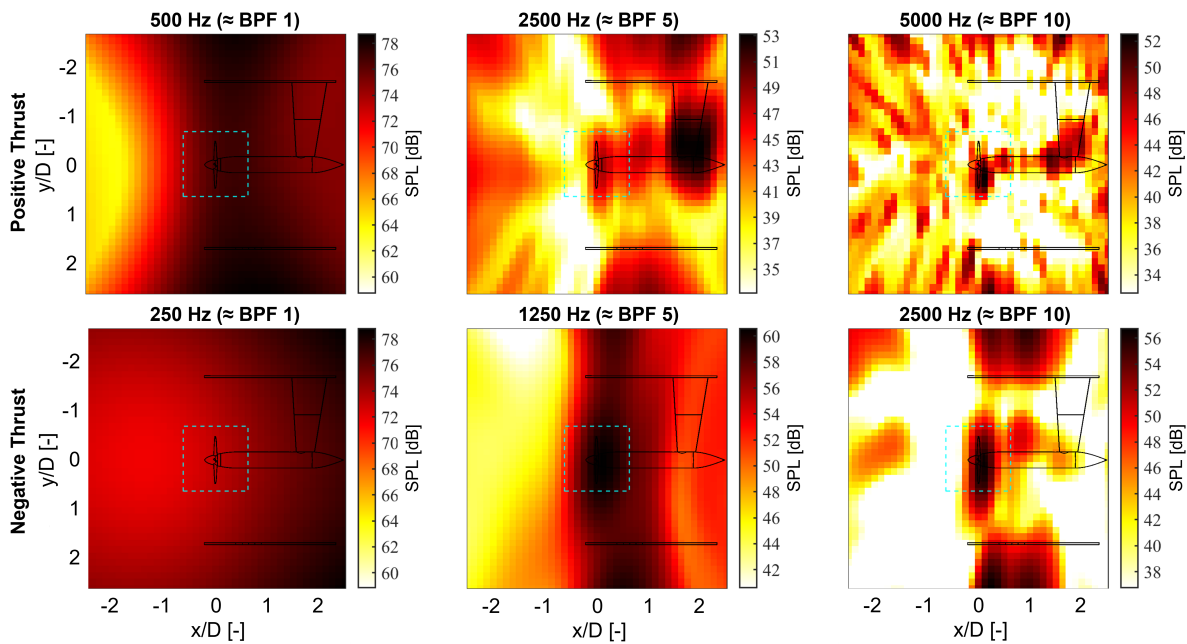


Figure 7.7: Beamforming maps for $V = 30$ m/s with the ROI indicated with the dashed line for frequencies nearest to the first, fifth, and tenth BPF at both thrust regimes.

Conversely, the shorter wavelength of the noise at higher frequencies allows the sensors in the array to be spaced closer together, resulting in higher beamforming resolution. The resolution of beamforming on noise signals is inversely proportional to the noise frequency, with higher frequencies resulting in improved resolution and vice versa. This is shown as smaller areas of noise sources that are separable. Beamforming is, therefore, more effective at higher frequencies than lower ones. Different effectiveness arise for different thrust conditions at each BPF multiple. The resolution is higher for positive thrust than for negative thrust in this experiment due to the higher angular frequency.

The maps are provided for frequencies that do not exactly match the BPF multiples. The shown maps are therefore considered broadband noise sources. While observing all the beamforming maps, significant sources were found at the propeller ($x = 0$), at $x = 0.47$, and at $x = 0.65$ at the y location of the rotational axis. The latter two distances match the motor's location and the support beam from the propeller hub. It is observed that significant noise sources from the motor and noise at the support beam are isolated properly for frequencies above ~ 2500 Hz due to the higher resolution. If we focus on the beamforming maps at 2500 Hz for both thrust conditions, the positive thrust condition shows a noise source that is most dominant at the support beam, which is not shown for the negative thrust condition. The support beam interacts with the wake and blade tip vortices, generating interaction noise. This interaction is stronger at higher thrust generating more noise. The primary source of negative thrust is the propeller's broadband component. This broadband component is significantly higher than at positive thrust due to the separation of the boundary layer observed during the BEM analysis in the negative thrust regime.

The region of integration (ROI) is indicated with the light blue dashed lines. This is integrated at each frequency to obtain the beamformed frequency spectrum of the signal. The ROI will have isolated the propeller noise more precisely for higher resolutions. The fundamental BPFs are at low frequencies and have poor beamforming resolutions that worsen for negative thrust conditions. The sound waves related to the motor noise and the bearings can also be emitted through the nacelle and its vibrations, which is (partially) situated in the ROI. This makes it more challenging to isolate motor noise from the signal. Despite the low resolution near the fundamental BPF, this approach will have contributed by partially filtering out reflections and background noise from the wind tunnel.

When the beamformed frequency spectra are plotted for each regime together with the spectrum of the beamformed wind tunnel noise measurement and the beamformed motor noise measurement, it is possible to distinguish four different cases at each BPF in the spectra, which are shown in Figure 7.8. The first situation, plot (a), shows that the wind tunnel level is higher than the total level of the test with the propeller. Therefore, no propeller noise has been measured at this BPF multiple. The second situation is shown in plot (b), where the measurement with only motor noise levels without loads exceeds the total noise measured. Therefore no propeller noise has been measured at this BPF multiple either. In plot (c), no increase in the tonal noise component was observed in the spectrum with respect to the broadband floor, showing that the broadband noise at those BPFs was higher than the tonal component. Finally, plot (d) shows a peak formed in the spectrum where other noise sources are significantly lower than the tonal component of the propeller noise. The tonal component is larger than the broadband component, the wind tunnel noise, and the motor noise. Each BPF of the plots can be categorized this way.

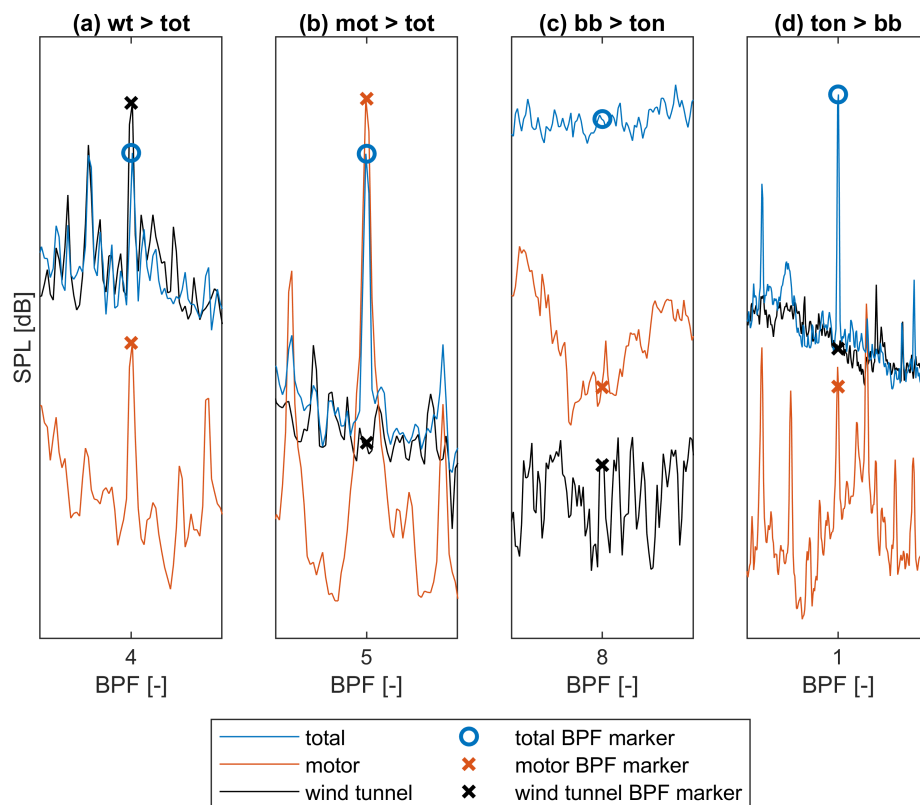


Figure 7.8: Different situations at each BPF of the total measurements with respect to the motor noise and wind tunnel noise.

Figure 7.9 shows the normalized spectra of the beamformed data for advance ratios of positive thrust, zero thrust, and negative thrust. The spectrum is plotted together with the beamformed motor noise data in red and the beamformed wind tunnel noise data in black in the first twelve BPF harmonics range,

each normalized with the BPF at the respective thrust setting. The SPL levels at the BPF harmonics are also marked for each spectrum. Tonal components at the fifth, eighth, and tenth BPF are the most apparent, and the motor noise measurements are also the highest. As the motor noise still shows significant discrete tonal components, the beamforming could not isolate the propeller noise fully from the motor noise. At negative thrust, the beamforming resolution was lower, resulting in a less effective separation of the noise sources.

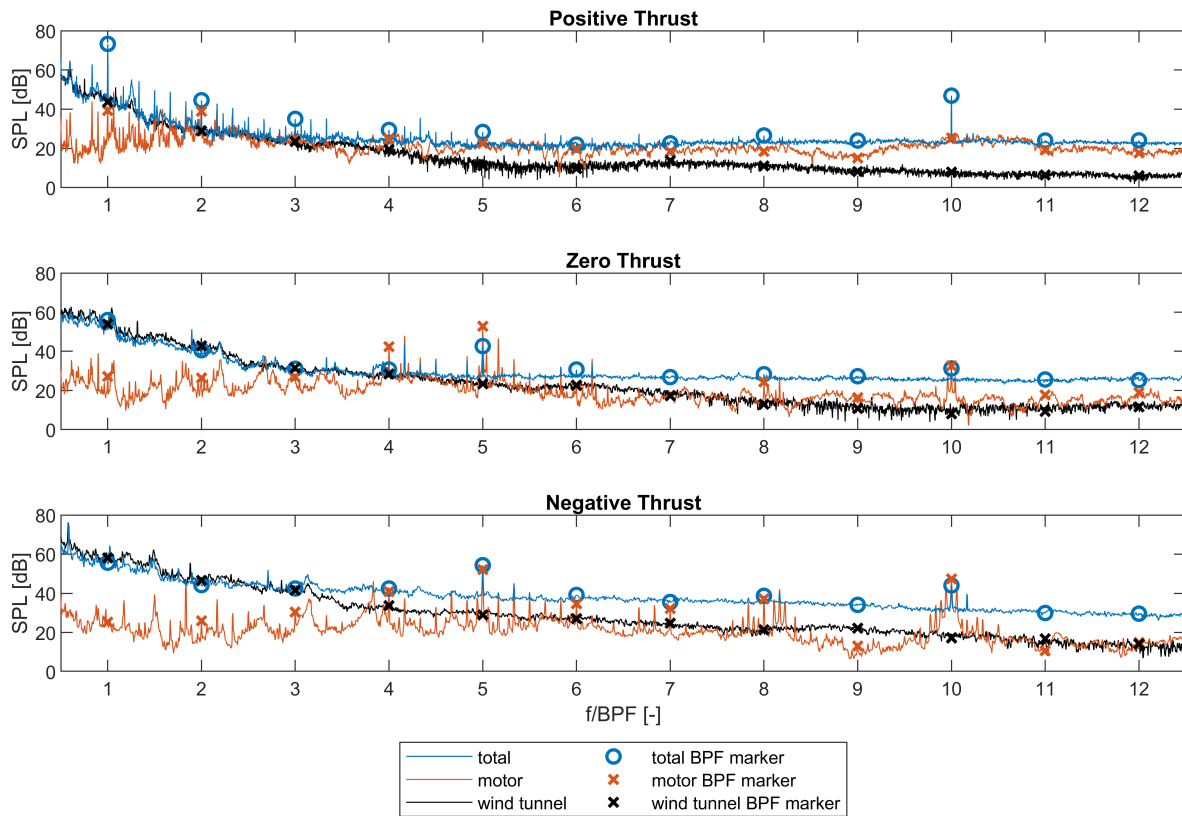


Figure 7.9: 12 BPF harmonics of beamformed spectra for positive, zero and negative thrust ($\Delta f = 1$ Hz).

Furthermore, only at positive thrust a clear peak at the fundamental BPF was shown, as the loading was the highest. There is more separation between the broadband motor and the propeller measurements at negative thrust. The rotational speed is lower, but due to the fully separated boundary layer, the broadband levels increased due to turbulent flow, causing random pressure fluctuations. The tonal components are higher at negative thrust than at higher thrust due to the motor's tonal components that decrease with the rotational speed, which was lower at negative thrust. The wind tunnel noise levels are dominant in the lower frequencies ranging from the first to the third or the fourth BPF harmonic.

Figure 7.10 shows the broadband frequency spectra for $V = 30$ m/s, normalized to the BPF. The few tonal components that result in a value are not representative of any analysis. Therefore, they are left out of the plot. The resulting broadband and tonal noise levels after subtraction of the wind tunnel noise and the motor noise measurements do not only contain the broadband and tonal propeller noise. The generated noise during the motor noise and the wind tunnel noise measurements might be higher during the propeller measurements, due to extra loads or the thrust force from the propeller, for instance. Therefore, the decomposition of the broadband and tonal components are not perfect. However, it is assumed that the influence of the wind tunnel and motor noise is minimized by subtracting the quantified wind tunnel and motor noise from the measurements. Tonal components at the BPF have not been determined for every thrust setting due to high wind tunnel noise, motor noise, or propeller broadband levels that masked the rotational noise. In any case, this does not mean that there was no tonal propeller component, but it was not dominant enough and too low to be measurable in this experimental

setup. Other noise sources masked the empty data points in the broadband plot. Especially in the low frequencies, the wind tunnel noise was often dominant enough to overrule the propeller broadband components.

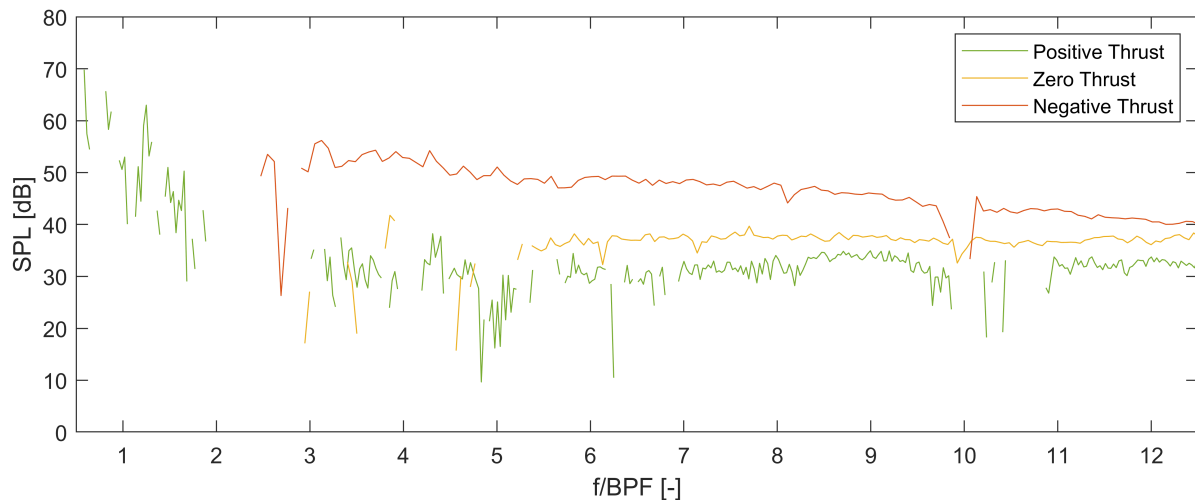


Figure 7.10: Resulting broadband and tonal propeller noise components at each regime after subtraction of wind tunnel noise and motor noise for $V = 30$ m/s ($\Delta f = 16$ Hz).

After beamforming, the motor noise still showed substantial interference with the propeller noise at the fifth, eighth, and tenth BPF harmonic for tonal components and the wind tunnel. The expected distribution of the tonal noise component of the propeller would start with a strong sound level at the fundamental BPF with harmonics that decrease in amplitude. Only for positive thrust a strong peak was found at the fundamental BPF. Often, the less significant peaks at the BPF multiples matched the strong tonal tones of the motor noise measurements. This could imply that the motor noise played a more substantial role with loads and that these increased tonal components are due to motor noise. To what extent the motor contributed to the measured tonal propeller components is unknown. Mechanical load on the motor would increase the friction and vibrations of the system, leading to an increase in mechanical noise. Also, the electrical load increases as the current increases, which may lead to increased noise levels. Extended experiments would be needed for the exclusion of this factor. The tonal noise components of the propeller are left out of the figure for the remaining of the report.

7.6. Overall Sound Pressure Levels

For the overall sound pressure level (OSPL) of the broadband propeller component, the SPL of the isolated broadband noise, as shown in Figure 7.10, was integrated over a frequency range after having applied a low-pass filter to exclude the LSB effects. The isolated broadband propeller noise resulted by subtracting the tonal noise components, wind tunnel noise, and motor noise from the full spectrum. The resulting noise levels might still include some contribution by the motor noise as the loaded motor noise might be higher than the subtracted unloaded motor noise. It can be considered that the contribution of motor noise to the isolated broadband propeller noise component is minimized as the unloaded motor noise was subtracted. Figure 7.11 shows the OSPL of the total noise, isolated broadband propeller component, and the motor noise as a function of the thrust coefficient (Equation 7.1) measured during each test condition for $V = 30$ m/s. It shows how the propeller's broadband component varies over the tested nine thrust settings.

The measurements show that the broadband propeller noise component decays with a lower thrust coefficient in positive thrust. When the thrust coefficient becomes more negative, the broadband noise component of the propeller grows significantly due to the boundary layer that is fully separated at negative thrust, introducing random pressure fluctuations. Based on the previously observed motor noise measurements, it is not probable that the increase is caused by the motor, as lower rotational speeds resulted in lower broadband motor noise. The pushing and pulling effect on the shaft due to the positive and negative thrust of the propeller might have caused a change in the noise generation between

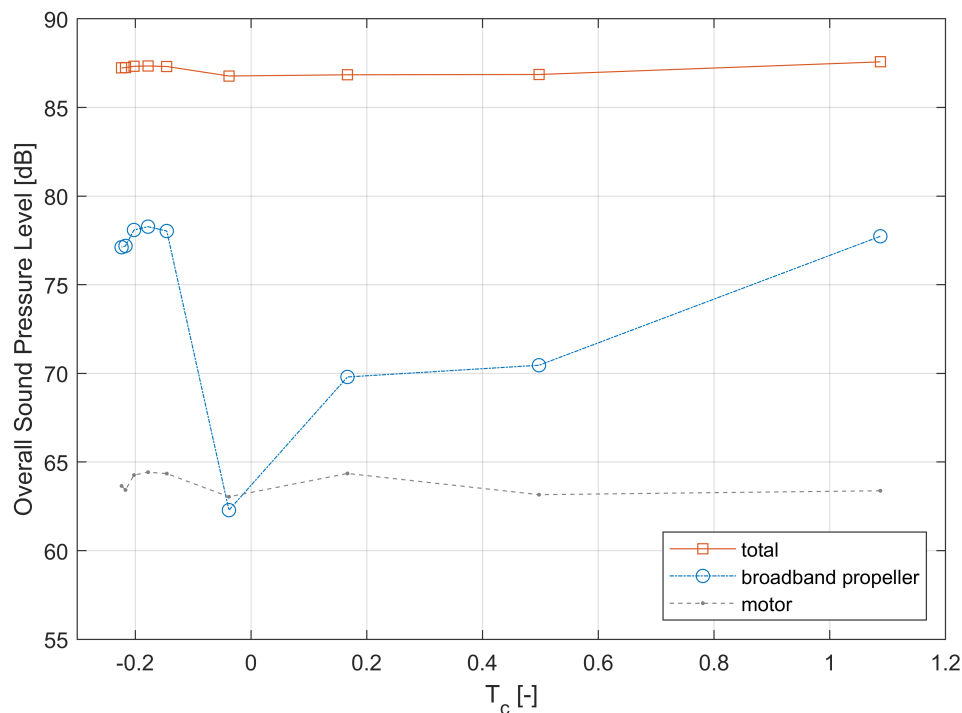


Figure 7.11: Overall sound pressure levels of different components and helical Mach number for different thrust settings.

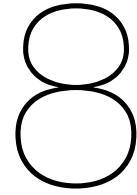
positive and negative thrust. The fact that the test conditions show a difference in similarity is also not the cause for the increase in broadband levels. When the tip Mach number at negative thrust is scaled up to the same tip Mach number as the one at positive thrust, the noise levels will increase with respect to the noise levels at the lower tip Mach number. Accordingly, the broadband noise generated by the propeller at negative thrust can be attributed to the fully separated boundary layer on the lower surface of the airfoil sections, as shown by the quantitative analysis based on the blade element momentum (BEM) theorem. Tonal propeller noise is sourced from aerodynamic loading and blade thickness. In the negative thrust regime, the loading on the blade was found to be smaller than in the positive condition due to the less efficient production of lift and lower tip Mach number. However, in this configuration, the propeller operates in a suboptimal design condition, generating more turbulent flow and increasing broadband noise.

Many thrust settings did not result in any visible tonal components from the propeller. In the low-frequency range, the broadband propeller noise was often masked by wind tunnel noise and tonal noise by the motor noise at the blade passing frequency harmonics. Most tonal components were observed at positive thrust, where the component at the fundamental BPF exceeded the wind tunnel noise in the low-frequency region. Conversely, at negative thrust, the tonal component of the motor was found to be the strongest. The higher motor noise masked the tonal components of the propeller, and due to the low beamforming resolution at negative thrust, these sources could not be isolated.

During this experiment, the advance ratio was varied by adjusting the rotational speed of the propeller. This approach makes it challenging to isolate the effect of negative and positive thrust on the noise generation of tonal components, as it also results in changes to the tip Mach number and the motor noise. The tip Mach number strongly affects the magnitude of the radiated noise.



Conclusion and Recommendations



Conclusion

This thesis aimed to examine the effect of positive and negative thrust regimes on the propeller's tonal and broadband noise sources. To achieve this goal, aeroacoustic measurements were performed in a wind tunnel using a scaled propeller setup, and signal processing techniques were applied to the noise data for analysis. The experiments were conducted using the available materials, and the noise sources of the propeller were isolated and quantified for both the negative and positive thrust modes using techniques such as fast Fourier transformation (FFT), phase averaging, beamforming, and blade element momentum (BEM) analysis. The results of these experiments allow for answering the main research question posed in chapter 1. This study investigated the impact of positive and negative thrust regimes on a propeller's tonal and broadband noise sources.

"How do propeller noise sources vary in relation to positive and negative thrust settings for an existing isolated forward thrust propeller?"

The experiments were conducted at low tip Mach numbers in a wind tunnel without acoustic treatment, which resulted in tonal noise components being largely masked by wind tunnel noise and motor noise. This interference made it difficult to conclusively determine the variation of tonal propeller noise in the negative thrust setting as it often did not rise above the quantified motor noise, wind tunnel noise, or propeller broadband noise. However, the validity of the test results can be shown by the fact that the overall magnitude of the wind tunnel noise is sufficiently lower than the propeller noise measurements. The thrust setting was adjusted by varying the rotational speed of the propeller, which resulted in changes to the tip Mach number, a key variable for the scaling of aeroacoustics, and the Reynolds number. Both tonal and broadband propeller components vary significantly with changing tip Mach number, and the motor noise demonstrated a strong relationship with its angular velocity. These factors made attributing the noise variation to the thrust setting variations challenging.

The motor noise was in various forms, with tonal motor noise components matching some of the blade passing frequencies (BPF). Furthermore, broadband motor noise components were higher during the tests at positive thrust conditions, while tonal motor components were higher at negative thrust condition tests. Another interfering noise source was the wind tunnel noise at low frequencies. Therefore, a high-pass filter was applied to the data to cancel out the dominance of the wind tunnel noise at low frequencies.

In the high-frequency region at positive thrust, an increase in broadband noise source was identified due to the laminar separation bubble, consistent with the blade element momentum (BEM) analysis results. The laminar separation bubble is known to appear at low Reynolds numbers. Full-scale propellers in real-flight conditions operate at much higher Reynolds numbers. Therefore, the noise data affected by the laminar separation bubble was excluded from the results. The BEM analysis revealed that the boundary layer on the lower surface of the airfoil section was fully separated at negative thrust mode. This suboptimal condition affects the aeroacoustic performance, as the separation can induce more broadband noise. The increase in broadband noise levels at negative thrust conditions compared

to positive thrust conditions was observed in the frequency spectra.

Broadband propeller noise components had the highest sound pressure levels in the low-frequency region, but the perceived acoustic emission could be different when weighting is applied after scaling. The overall sound pressure level of the broadband propeller noise decreased with decreasing thrust coefficient in the positive thrust regime. The broadband noise components of the propeller measurements were significantly higher in the negative thrust condition with respect to positive thrust conditions.

The literature on propeller noise primarily focuses on the prediction of dominant tonal noise components, often neglecting the contribution of broadband noise. However, these experimental results indicate that broadband noise becomes increasingly significant at negative thrust conditions, making it a crucial aspect to consider in future studies on propeller noise under negative thrust conditions. Further experimental research is essential to determine the relative importance of tonal and broadband noise components in this regime as a step to make aviation climate-neutral by 2050.

9

Recommendations

The experimental study described in this thesis has the potential to be expanded upon through further research. Building upon the work and discussion presented in this thesis, this section offers several recommendations for future work that could enhance understanding of the negative thrust regime of propellers and ultimately contribute to the decarbonization of the aviation industry.

- To ensure the validity of the results, it would be advisable to experiment in an acoustically treated wind tunnel. The surfaces of an acoustically treated wind tunnel absorb noise energy, reducing wall and floor reflections, which is expected to improve the signal-to-noise ratio of the data significantly. The environment in an anechoic chamber is a free-field environment in acoustics, which can be considered far-field for noise measurements.
- It is recommended to add an internal load cell for the thrust measurements; this isolates the effects of the propeller slipstream and support beam interaction.
- Multiple approaches exist that may reduce the interference of motor noise during the experiments. For example, increasing the distance between the motor and the propeller by altering the motor's placement improves beamforming results. Alternatively, decreasing the number of blades from six to three would shift the first dominant motor tonal component, which appears at the fifth blade passing frequency (BPF) multiple, to the tenth BPF multiple. This would provide more BPF multiples of propeller noise with less interference from the motor but would also worsen the beamforming resolution at each BPF multiple. Another option is to adjust the angular frequency of the motor to be different from that of the propeller, which may be the most effective at reducing the impact of tonal motor noise at frequencies of discrete propeller tones. This objective can be achieved by using drive pulleys, for instance.
- Quantification of the motor noise with loads would improve the isolation of motor noise from the total noise measurements. The blade load effects on the motor noise have not been considered. The method should be explored, as this would give more accurate propeller noise levels. The positive and negative thrust regimes create a pushing and pulling effect on the motor shaft. This means that loads on the shaft, bearings, and motor are in opposite directions between the two regimes. The effect on the generated sound by the motor with the variation of thrust setting is yet unknown.
- It would be insightful to know how the amplitude varies at the positive and negative thrust regimes in the frequency region that is affected by the noise of the laminar separation bubble. This can be achieved, for example, by experimenting with higher Reynolds numbers or by numerical predictions. In real-life (at higher Reynolds numbers), the laminar separation bubble would not appear. The appearance of laminar separation bubbles now masked this region of frequencies.
- To ensure that a model propeller maintains a constant similarity between the test conditions, it is advisable to maintain a constant tip Mach number and a constant advance ratio. The positive and negative thrust modes can be achieved through changes in the blade pitch. This will improve

the quality of the data in various ways.

The beamforming resolution varied relative to the normalized frequencies. The BPF at positive thrust was higher than the BPF at negative thrust, resulting in higher beamforming resolution for the BPF at positive thrust. This affects the accuracy of the decomposition of the different noise sources, which could be avoided by maintaining a constant angular frequency throughout the tests.

The generated motor noise shows a strong relationship with its speed, which resulted in a varying level of interference with the propeller noise for different thrust settings. A constant rotational speed would minimize the noise variation for different thrust settings, as the change in load becomes the only variable affecting the motor noise levels.

The helical tip Mach number is an important similarity parameter in aeroacoustics, as it strongly affects the radiated noise levels of a propeller. Therefore, canceling variations in the helical tip Mach number is favorable. This can be achieved with a constant tip Mach number and a constant advance ratio. A constant Reynolds number will also be maintained by maintaining a constant helical tip Mach number, a metric that affects the aerodynamic performance of the propeller.

- Tests at higher speeds showed higher sound pressure levels, and the wind tunnel noise and the motor noise were less dominant for $V = 30$ m/s with respect to $V = 20$ m/s. Therefore, it is recommended to increase the wind speeds for an improved measurement of propeller noise. By raising the tip Mach number and the Reynolds number, an improvement in similarity with the full-scale case is also realized. This research's interest lies in assessing aeroacoustic behavior in variations in thrust setting. d. Besides more apparent propeller noise levels, the overall beamforming resolution would benefit from the higher BPF.
- The acoustic measurements were only performed at an angle of attack of zero degrees. Studying the effects of the negative thrust regime at different angles of attack is recommended. The negative thrust mode will most likely be employed at flight conditions where the forward thrust is least necessary, such as during descent.
- This thesis focused on isolated propellers only. Therefore, installation and interference effects on the aeroacoustic performances were not studied. These effects will have to be considered in further studies. Apart from the acoustics, the reversed thrust direction can affect the control surfaces if the control surfaces are located downstream of the propeller.
- Blade sweep is often applied to modern aircraft propellers to increase efficiency and reduce noise. But the effect of blade sweep on noise in regenerative mode is still unknown. The TUD-XPROP was used in this thesis and is not representative of the aeroacoustics of swept propeller blades. Therefore, the swept blades should be included in future studies on aeroacoustics in regenerative mode.

Bibliography

- [1] Propeller terminology. URL <http://www.expertsmind.com/questions/propeller-terminology-30112145.aspx>.
- [2] Project overview. URL <https://futprint50.eu/about/project-overview>.
- [3] Low turbulence tunnel. URL <https://www.tudelft.nl/lr/organisatie/afdelingen/flow-physics-and-technology/facilities/low-speed-wind-tunnels/low-turbulence-tunnel>.
- [4] 1903 wright flyer. URL https://airandspace.si.edu/collection-objects/1903-wright-flyer/nasm_A19610048000.
- [5] Our paris letter, 1882. URL <http://nla.gov.au/nla.news-article97293603>.
- [6] *World intellectual property report: breakthrough innovation and economic growth*, volume 944E. WIPO, 2015.
- [7] Joshua B. Anderson, Ellen K. Wilkes, John W. McClintic, and David G. Bogard. Effects of freestream mach number, reynolds number, and boundary layer thickness on film cooling effectiveness of shaped holes. In *Turbo Expo: Power for Land, Sea, and Air*, volume 49804, page V05CT19A003. American Society of Mechanical Engineers, 2016.
- [8] E. N. da C. Andrade. Doppler and the doppler effect. 1959.
- [9] R. M. Bass. Techniques of model propeller testing. Technical report, SAE Technical Paper, 1983.
- [10] Glenn D. Bergland. A guided tour of the fast fourier transform. *IEEE spectrum*, 6(7):41–52, 1969.
- [11] P. J. W. Block and C. L. Gentry Jr. Directivity and trends of noise generated by a propeller in a wake. 1986.
- [12] Roberto F Bobenrieth Miserda, Ana Maldonado, and Braulio Gutierrez. A moving-body high-order immersed boundary method for computational aeroacoustics. In *17th AIAA/CEAS Aeroacoustics Conference (32nd AIAA Aeroacoustics Conference)*, page 2753, 2011.
- [13] T. Britannica. Hans joachim pabst von ohain. URL <https://www.britannica.com/biography/Hans-Joachim-Pabst-von-Ohain>.
- [14] Murat Bronz, Jean Marc Moschetta, and Gautier Hattenberger. Multi-point optimisation of a propulsion set as applied to a multi-tasking mav. In *IMAV 2012, International Micro Aerial Vehicle Conference and Competition*. Citeseer, 2012.
- [15] Thomas F. Brooks and Michael A. Marcolini. Airfoil tip vortex formation noise. *AIAA journal*, 24(2):246–252, 1986.
- [16] H. H. Brouwer. Anechoic wind tunnels. 1997.
- [17] David Brown and John B. Ollerhead. Propeller noise at low tip speeds. Technical report, WYLE LABS HAMPTON VA, 1971.
- [18] Michael Carley. Propeller noise fields. *Journal of Sound and Vibration*, 233(2):255–277, 2000.
- [19] Paolo Chiariotti, Milena Martarelli, and Paolo Castellini. Acoustic beamforming for noise source localization—reviews, methodology and applications. *Mechanical Systems and Signal Processing*, 120:422–448, 2019.

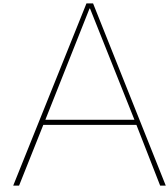
- [20] Bridget Cogley. World's first commercial electric plane takes off in vancouver, Dec 2019. URL <https://www.dezeen.com/2019/12/17/worlds-first-commercial-electric-plane-canada-seaplane/>.
- [21] T. D. Crouch. Ader Éole. URL <https://www.britannica.com/topic/Ader-Eole>.
- [22] Sean Dooley. The development of material-adapted structural form. Technical report, EPFL, 2004.
- [23] G. Eitelberg, T. Pelt, and T. Sinnige. *AE4115: Experimental Simulations Reader*. Delft University of Technology, 2020.
- [24] Wendell E. Eldred, Henry H. Kerr, and Harold H. Warden. Weight reduction of aircraft braking systems through use of reverse-thrust propellers. *SAE Transactions*, pages 107–119, 1946.
- [25] I. E. Garrick and Charles E. Watkins. A theoretical study of the effect of forward speed on the free-space sound-pressure field around propellers. Technical report, 1953.
- [26] Xin Geng, Tianxiang Hu, Peiqing Liu, Tomas Sinnige, and Georg Eitelberg. Analysis of thrust-scaled acoustic emissions of aircraft propellers and their dependence on propulsive efficiency. In *32nd Congress of the International Council of the Aeronautical Sciences*, pages ICAS–2021. International Council of the Aeronautical Sciences, 2021.
- [27] Jatinder Goyal, Tomas Sinnige, Francesco Avallone, and Carlos Ferreira. Aerodynamic and aeroacoustic characteristics of an isolated propeller at positive and negative thrust. In *AIAA Aviation 2021 Forum*, 2021.
- [28] Edoardo Grande, Daniele Ragni, Francesco Avallone, and Damiano Casalino. Laminar separation bubble noise on a propeller operating at low reynolds numbers. *AIAA Journal*, 60(9):5324–5335, 2022.
- [29] Edoardo Grande, Gianluca Romani, Daniele Ragni, Francesco Avallone, and Damiano Casalino. Aeroacoustic investigation of a propeller operating at low reynolds numbers. *AIAA Journal*, 60(2): 860–871, 2022.
- [30] L. Gutin. On the sound field of a rotating propeller. *Physikalische Zeitschrift der Sowjetunion: Physical magazine of the Soviet Union volume 9 number 1*, 9(NACA-TM-1195), 1948.
- [31] Mohammed Haddaoui. Development of a propeller source noise model. 2019.
- [32] Nancy Hall. Types of wind tunnels. URL <https://www.grc.nasa.gov/www/k-12/airplane/tuntype.html>.
- [33] Richard Hallion. Taking flight: inventing the aerial age from antiquity through the first world war. page 22, 2003. doi: 978-0-19-516035-2.
- [34] Donald B. Hanson. Influence of propeller design parameters on far-field harmonic noise in forward flight. *AIAA Journal*, 18(11):1313–1319, 1980.
- [35] Edwin P. Hartman and David Biermann. *The negative thrust and torque of several full-scale propellers and their application to various flight problems*. US Government Printing Office, 1938.
- [36] D. L. Hawkings and M. V. Lawson. Theory of open supersonic rotor noise. *Journal of Sound and Vibration*, 36(1):1–20, 1974.
- [37] William S. Hedrick and William M. Douglass. An experimental investigation of the thrust and torque produced by propellers used as aerodynamic brakes. Technical report, National Aeronautics and Space Administration, 1944.
- [38] Harvey H. Hubbard. *Aeroacoustics of flight vehicles: theory and practice*, volume 1. National Aeronautics and Space Administration (NASA), 1991.
- [39] National Instruments. Understanding ffts and windowing. URL <https://download.ni.com/evaluation/pxi/Understanding20FFTs20and20Windowing.pdf>.

- [40] K. Kimura. Wind loads. In Alessio Pipinato, editor, *Innovative bridge design handbook (second edition)*, pages 47–59. Butterworth-Heinemann, second edition edition, 2022. ISBN 978-0-12-823550-8. doi: <https://doi.org/10.1016/B978-0-12-823550-8.00031-7>. URL <https://www.sciencedirect.com/science/article/pii/B9780128235508000317>.
- [41] Michael Kingan, Vincent Blandeau, Brian Tester, Phillip Joseph, and Anthony Parry. Relative importance of open rotor tone and broadband noise sources. In *17th AIAA/CEAS Aeroacoustics Conference (32nd AIAA Aeroacoustics Conference)*, page 2763, 2011.
- [42] Daniel Król, Anita Lorenc, and Radosław Świcęński. Detecting laterality and nasality in speech with the use of a multi-channel recorder. In *2015 IEEE International Conference on Acoustics, Speech and Signal Processing (ICASSP)*, pages 5147–5151. IEEE, 2015.
- [43] D. W. Kurtz and J. E. Marte. A review of aerodynamic noise from propellers, rotors, and lift fans. 1970.
- [44] John Lamancusa. Sound reasons. URL <https://www.lockhaven.edu/~dsimanek/puzzles/soundreasons.htm>.
- [45] Jerad Lewis. Understanding microphone sensitivity. *Analog Dialogue*, 46(2):14–16, 2012.
- [46] Michael James Lighthill. On sound generated aerodynamically. *Proceedings of the Royal Society of London. Series A. Mathematical and Physical Sciences*, 211(1107):564–587, 1952.
- [47] Paul MacCready. Regenerative battery-augmented soaring. *Technical Soaring*, 23(1):28–32, 1999.
- [48] J. Robert Mahan and Allen Karchmer. Combustion and core noise. *Aeroacoustics of flight vehicles: theory and practice*, 1:483–517, 1991.
- [49] S. Mayoral. Aerodynamic forces on immersed bodies. *California State University, Fullerton*, 2016.
- [50] Ron Moulton. An electric aeroplane. *Flight International*, page 946–946, Dec 1973. URL <https://www.flightglobal.com/FlightPDFArchive/1973/1973-2937.pdf>.
- [51] Michael J. Neufeld. Rocket aircraft and the ‘turbojet revolution’: The luftwaffe’s quest for high speed flight 1935–1939. *Innovation and the Development of Flight*, page 212, 1999.
- [52] Changhyun Pang, Gil-Yong Lee, Tae-il Kim, Sang Moon Kim, Hong Nam Kim, Sung-Hoon Ahn, and Kaohp-Yang Suh. A flexible and highly sensitive strain-gauge sensor using reversible interlocking of nanofibres. *Nature materials*, 11(9):795–801, 2012.
- [53] Anthony Brian Parry. *Theoretical prediction of counter-rotating propeller noise*. PhD thesis, University of Leeds, 1988.
- [54] Caterina Poggi, Giovanni Bernardini, Massimo Gennaretti, and Roberto Camussi. Scalability of mach number effects on noise emitted by side-by-side propellers. *Applied Sciences*, 12(19):9507, 2022.
- [55] Arthur A. Regier and Harvey H. Hubbard. Status of research on propeller noise and its reduction. *The Journal of the Acoustical Society of America*, 25(3):395–404, 1953.
- [56] Mitch Ricketts. Illustrating abstract concepts with concrete examples in web-based learning. In *ASSE Professional Development Conference and Exposition*. OnePetro, 2012.
- [57] Cameron Rose. Introduction to wavelet theory, Oct 2018. URL <https://medium.com/financial-time-series-denoising-with-wavelet/introduction-to-wavelet-theory-ddafa4204707>.
- [58] Hanspeter Schmid. How to use the fft and matlab’s pwelch function for signal and noise simulations and measurements. *FHNW/IME*, pages 2–13, 2012.

- [59] John Semmlow. Chapter 4 - signal analysis in the frequency domain—implications and applications. In John Semmlow, editor, *Circuits, Signals and Systems for Bioengineers (Third Edition)*, Biomedical Engineering, pages 169–206. Academic Press, third edition edition, 2018. ISBN 978-0-12-809395-5. doi: <https://doi.org/10.1016/B978-0-12-809395-5.00004-7>.
- [60] Jack H. Sheets and Gordon W. MacKinney. Reverse-thrust propellers as landing brakes. *SAE Transactions*, pages 257–263, 1945.
- [61] Dick G. Simons. *Introduction to aircraft noise*. Delft University of Technology, 2019.
- [62] Tomas Sinnige. *Aerodynamic and aeroacoustic interaction effects for tip-mounted propellers: An experimental study*. PhD thesis, Delft University of Technology, 2018.
- [63] Tomas Sinnige, Tom Stokkermans, Nando Van Arnhem, and L. L. M. Veldhuis. Aerodynamic performance of a wingtip-mounted tractor propeller configuration in windmilling and energy-harvesting conditions. In *AIAA Aviation 2019 Forum*, page 3033, 2019.
- [64] S. Sunada, K. Ozaki, M. Tanaka, T. Yasuda, K. Yasuda, and Keiji Kawachi. Airfoil characteristics at a low reynolds number. *Journal of Flow Visualization and Image Processing*, 7(3), 2000.
- [65] Christopher K. W. Tam and M. Salikuddin. Weakly nonlinear acoustic and shock-wave theory of the noise of advanced high-speed turbopropellers. *Journal of Fluid Mechanics*, 164:127–154, 1986.
- [66] L. L. M. Veldhuis. Propeller wing aerodynamic interference. 2005.

VI

Appendices



Frequency Spectrum

A.1. Frequency Spectra run 1

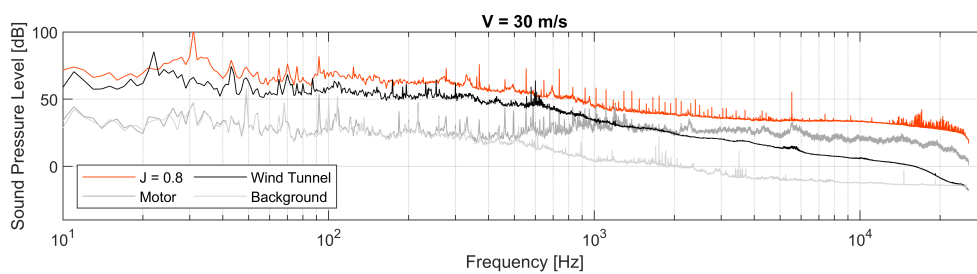


Figure A.1: Frequency spectrum of run 1 test 2, wind tunnel noise, motor noise, and background noise averaged over all microphones ($\Delta f = 1$ Hz).

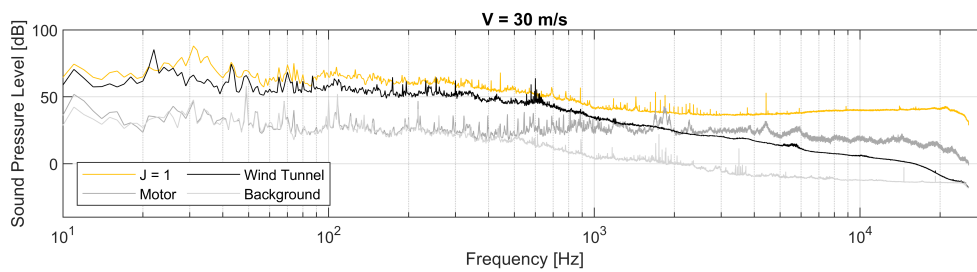


Figure A.2: Frequency spectrum of run 1 test 3, wind tunnel noise, motor noise, and background noise averaged over all microphones ($\Delta f = 1$ Hz).

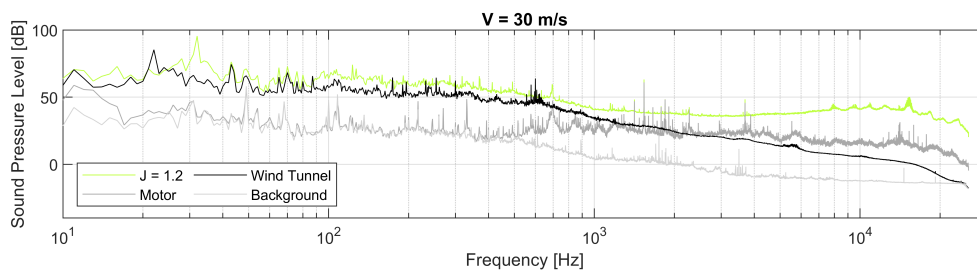


Figure A.3: Frequency spectrum of run 1 test 4, wind tunnel noise, motor noise, and background noise averaged over all microphones ($\Delta f = 1$ Hz).

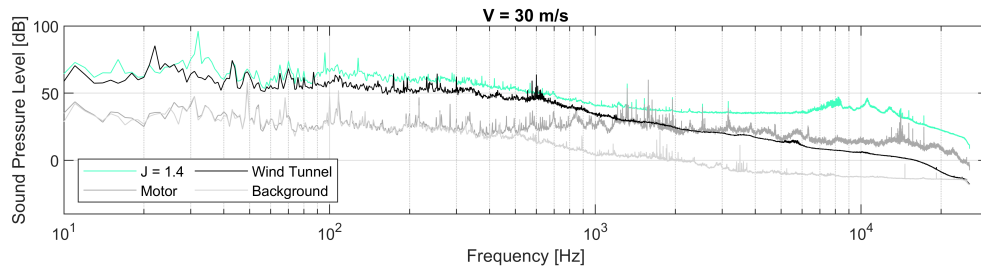


Figure A.4: Frequency spectrum of run 1 test 5, wind tunnel noise, motor noise, and background noise averaged over all microphones ($\Delta f = 1$ Hz).

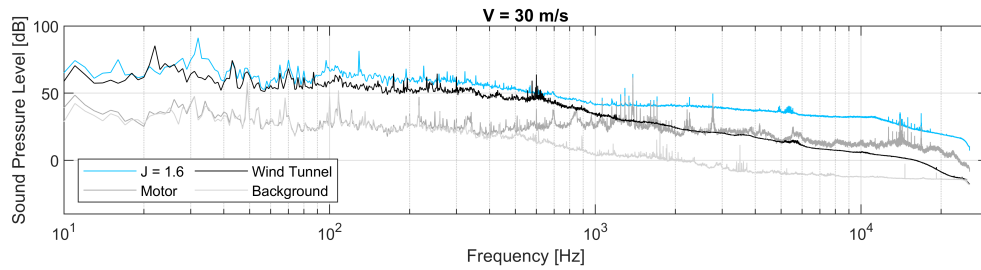


Figure A.5: Frequency spectrum of run 1 test 6, wind tunnel noise, motor noise, and background noise averaged over all microphones ($\Delta f = 1$ Hz).

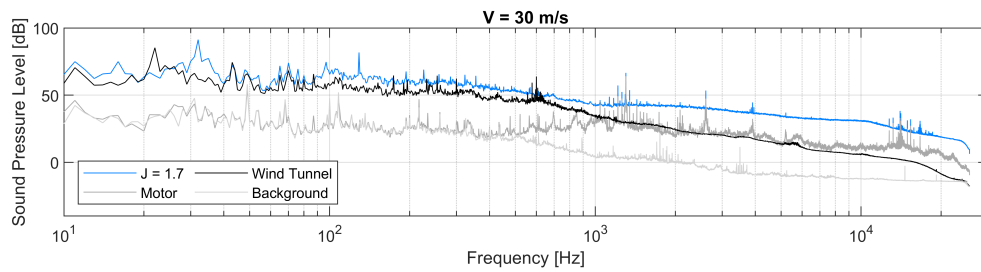


Figure A.6: Frequency spectrum of run 1 test 7, wind tunnel noise, motor noise, and background noise averaged over all microphones ($\Delta f = 1$ Hz).

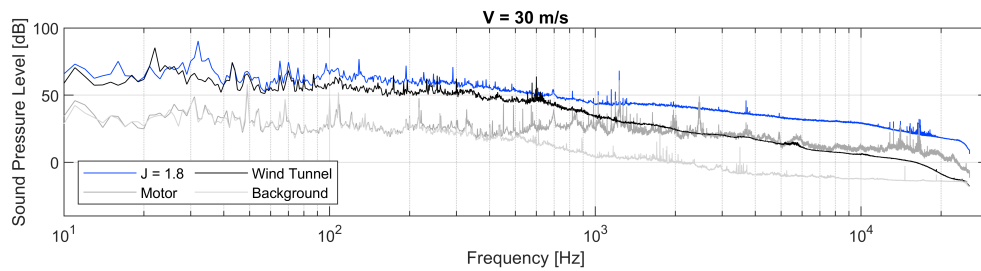


Figure A.7: Frequency spectrum of run 1 test 8, wind tunnel noise, motor noise, and background noise averaged over all microphones ($\Delta f = 1$ Hz).

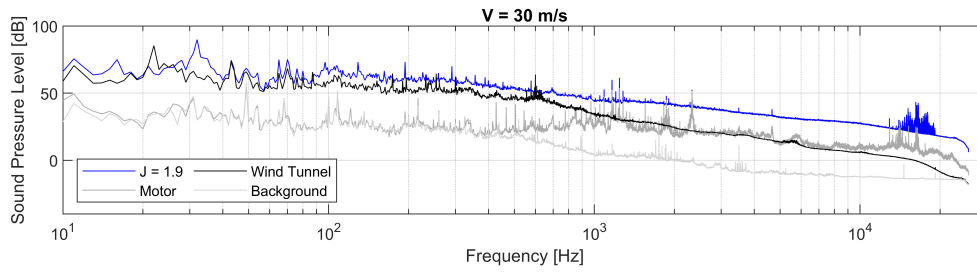


Figure A.8: Frequency spectrum of run 1 test 9, wind tunnel noise, motor noise, and background noise averaged over all microphones ($\Delta f = 1$ Hz).

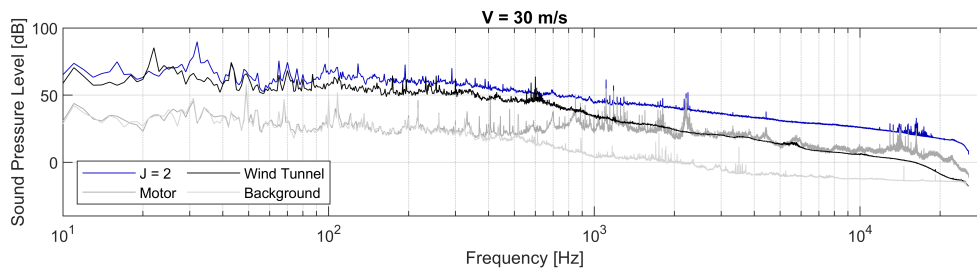


Figure A.9: Frequency spectrum of run 1 test 10, wind tunnel noise, motor noise, and background noise averaged over all microphones ($\Delta f = 1$ Hz).

A.2. Frequency Spectra run 2

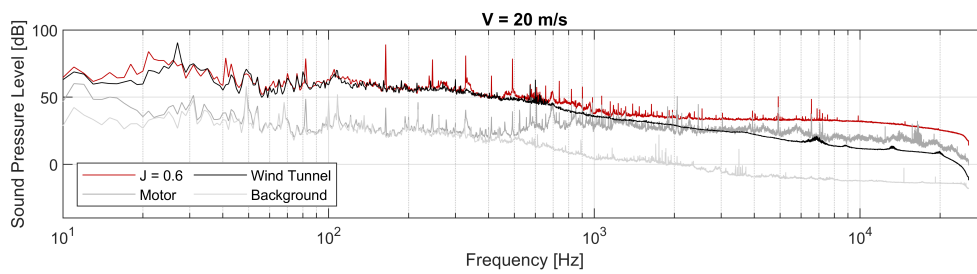


Figure A.10: Frequency spectrum of run 2 test 1, wind tunnel noise, motor noise, and background noise averaged over all microphones ($\Delta f = 1$ Hz).

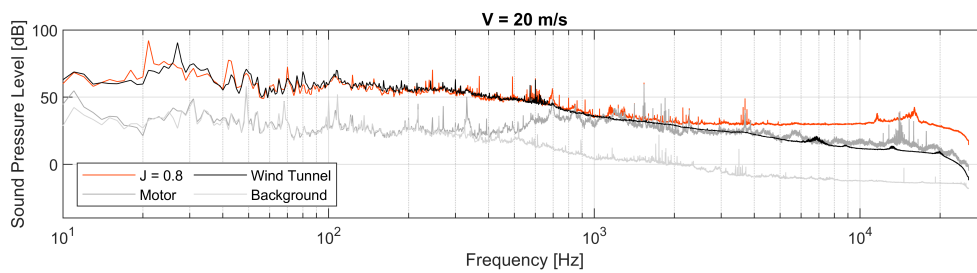


Figure A.11: Frequency spectrum of run 2 test 2, wind tunnel noise, motor noise, and background noise averaged over all microphones ($\Delta f = 1$ Hz).

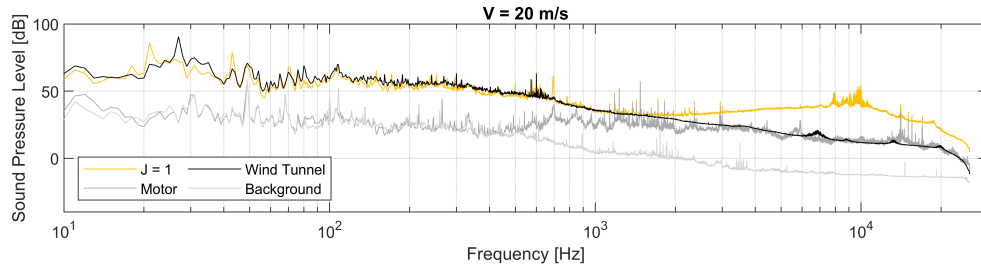


Figure A.12: Frequency spectrum of run 2 test 3, wind tunnel noise, motor noise, and background noise averaged over all microphones ($\Delta f = 1$ Hz).

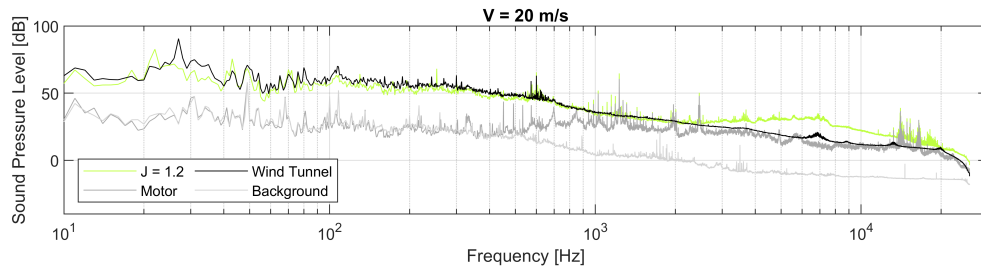


Figure A.13: Frequency spectrum of run 2 test 4, wind tunnel noise, motor noise, and background noise averaged over all microphones ($\Delta f = 1$ Hz).

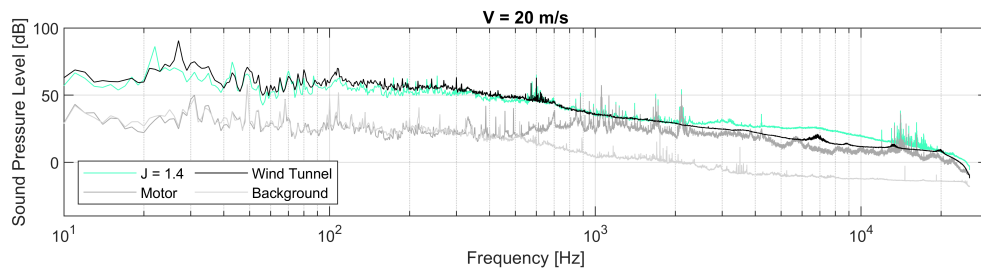


Figure A.14: Frequency spectrum of run 2 test 5, wind tunnel noise, motor noise, and background noise averaged over all microphones ($\Delta f = 1$ Hz).

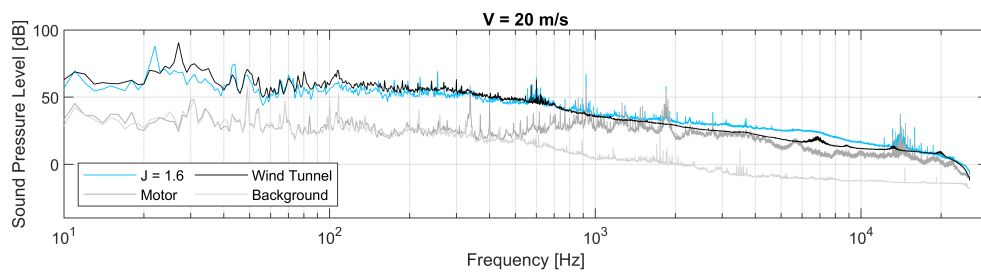


Figure A.15: Frequency spectrum of run 2 test 6, wind tunnel noise, motor noise, and background noise averaged over all microphones ($\Delta f = 1$ Hz).

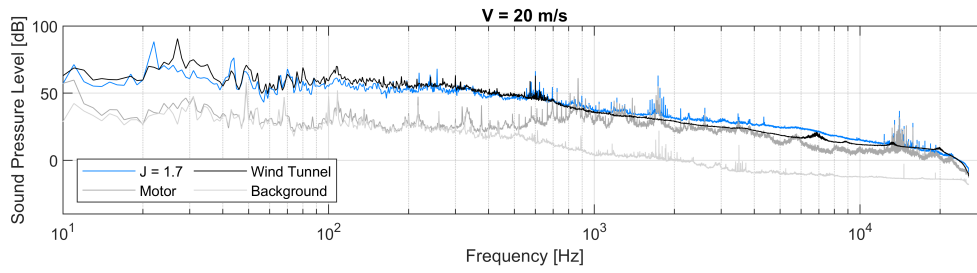


Figure A.16: Frequency spectrum of run 2 test 7, wind tunnel noise, motor noise, and background noise averaged over all microphones ($\Delta f = 1$ Hz).

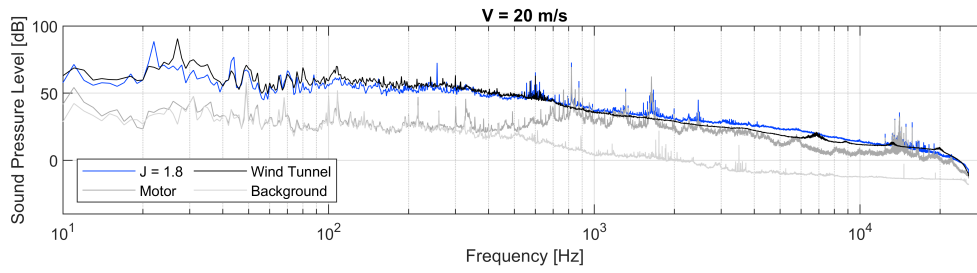


Figure A.17: Frequency spectrum of run 2 test 8, wind tunnel noise, motor noise, and background noise averaged over all microphones ($\Delta f = 1$ Hz).

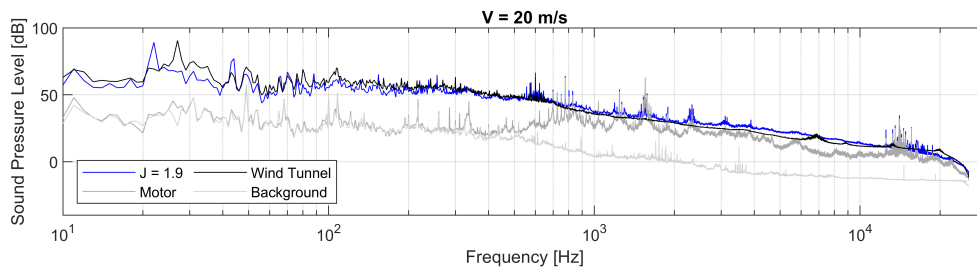


Figure A.18: Frequency spectrum of run 2 test 9, wind tunnel noise, motor noise, and background noise averaged over all microphones ($\Delta f = 1$ Hz).

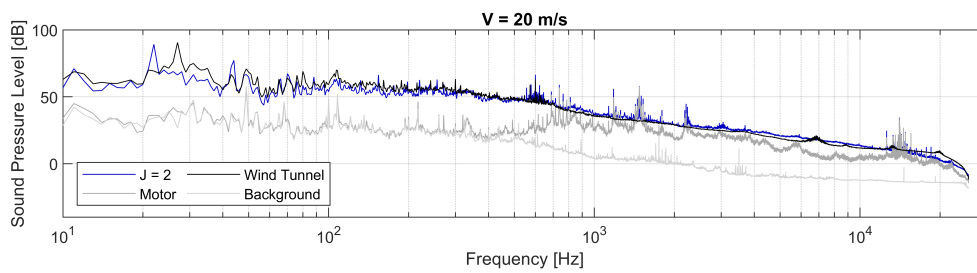


Figure A.19: Frequency spectrum of run 2 test 10, wind tunnel noise, motor noise, and background noise averaged over all microphones ($\Delta f = 1$ Hz).

B

Phase Average

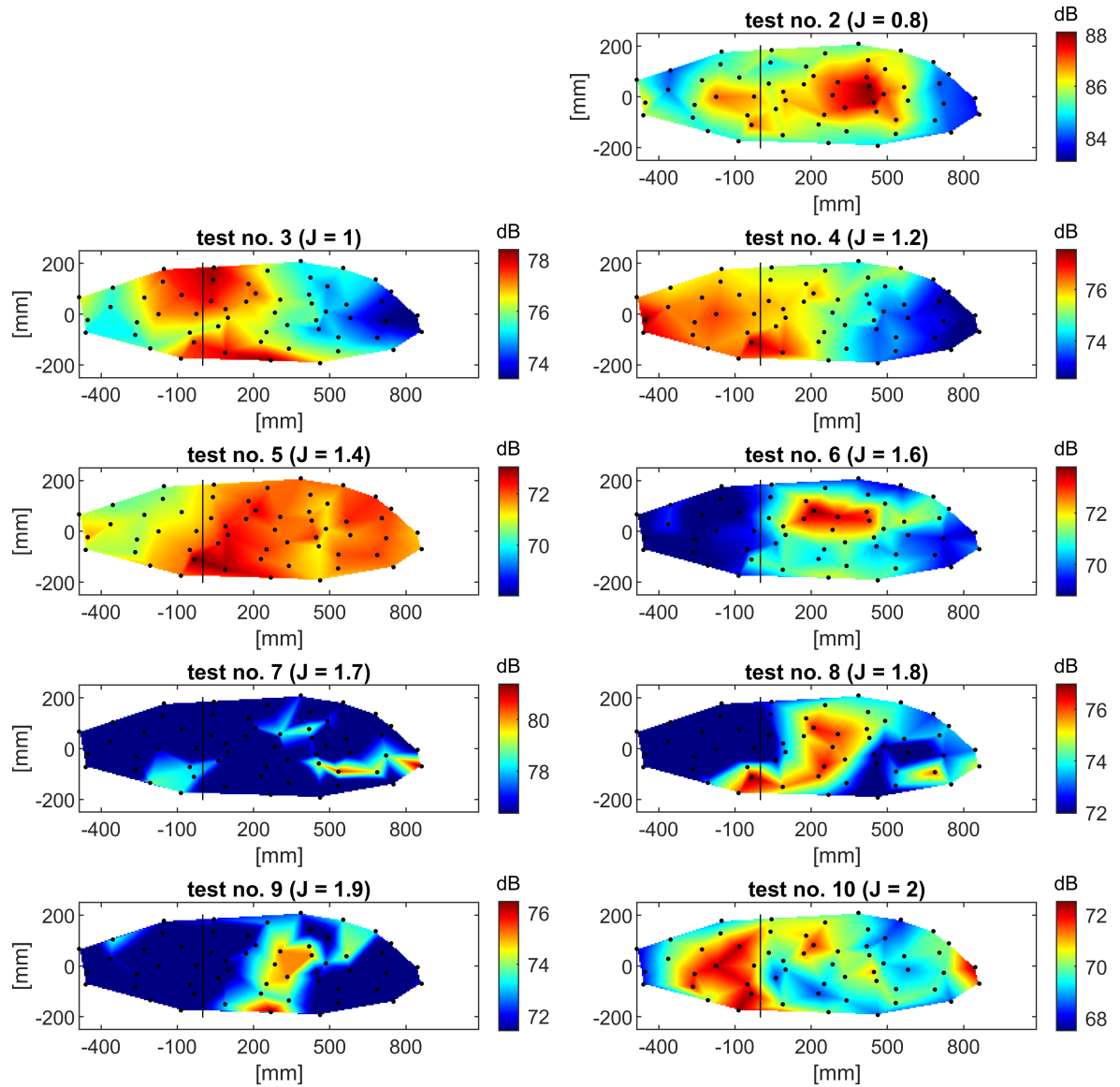
Phase Averaged Noise Levels ($V = 30$ m/s, 5 dB range)

Figure B.1: Phase averaged sound pressure levels for run 1.

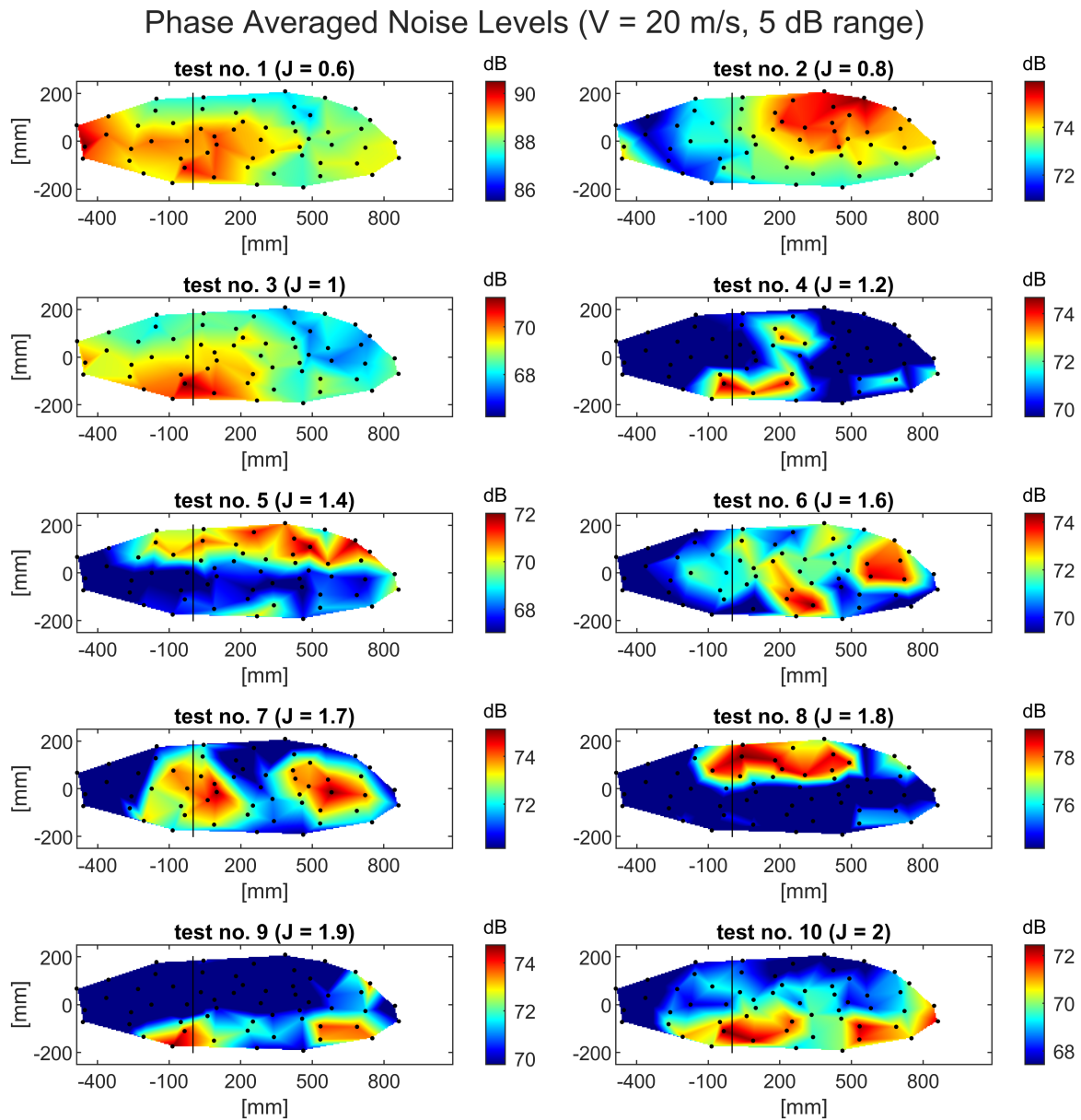
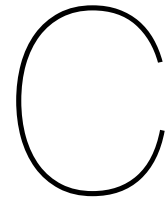


Figure B.2: Phase averaged sound pressure levels for run 2.



Beamforming

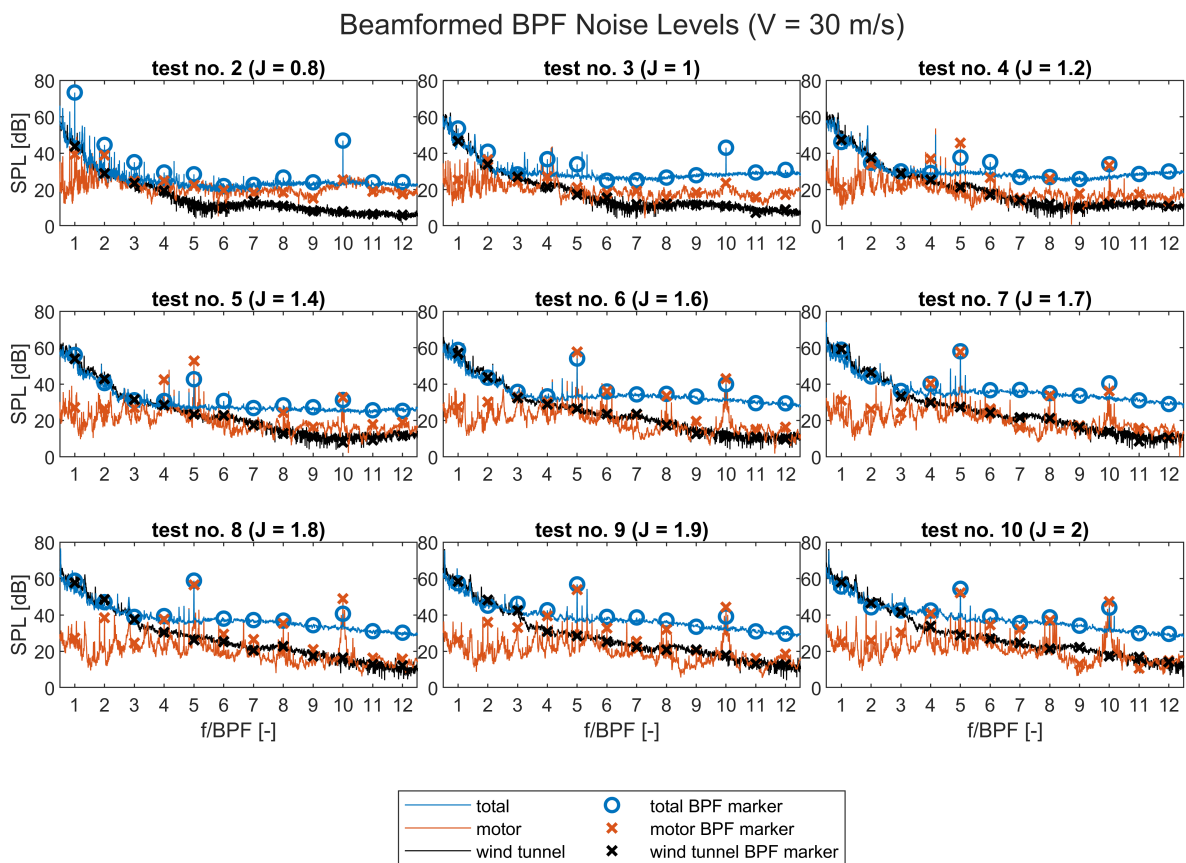
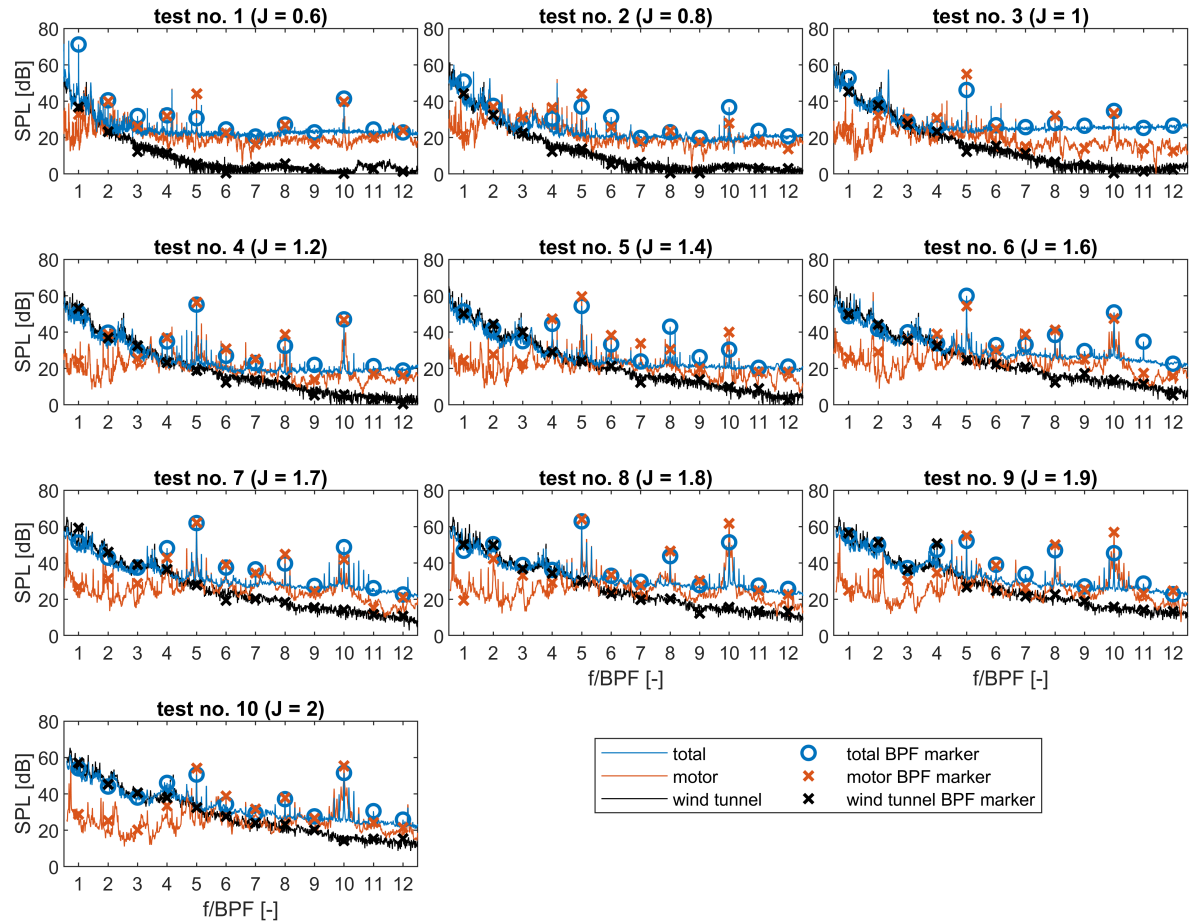


Figure C.1: 12 BPF harmonics of beamformed spectra for each test case of run 1 ($\Delta f = 1$ Hz).

Beamformed BPF Noise Levels ($V = 20$ m/s)Figure C.2: 12 BPF harmonics of beamformed spectra for each test case of run 2 ($\Delta f = 1$ Hz).

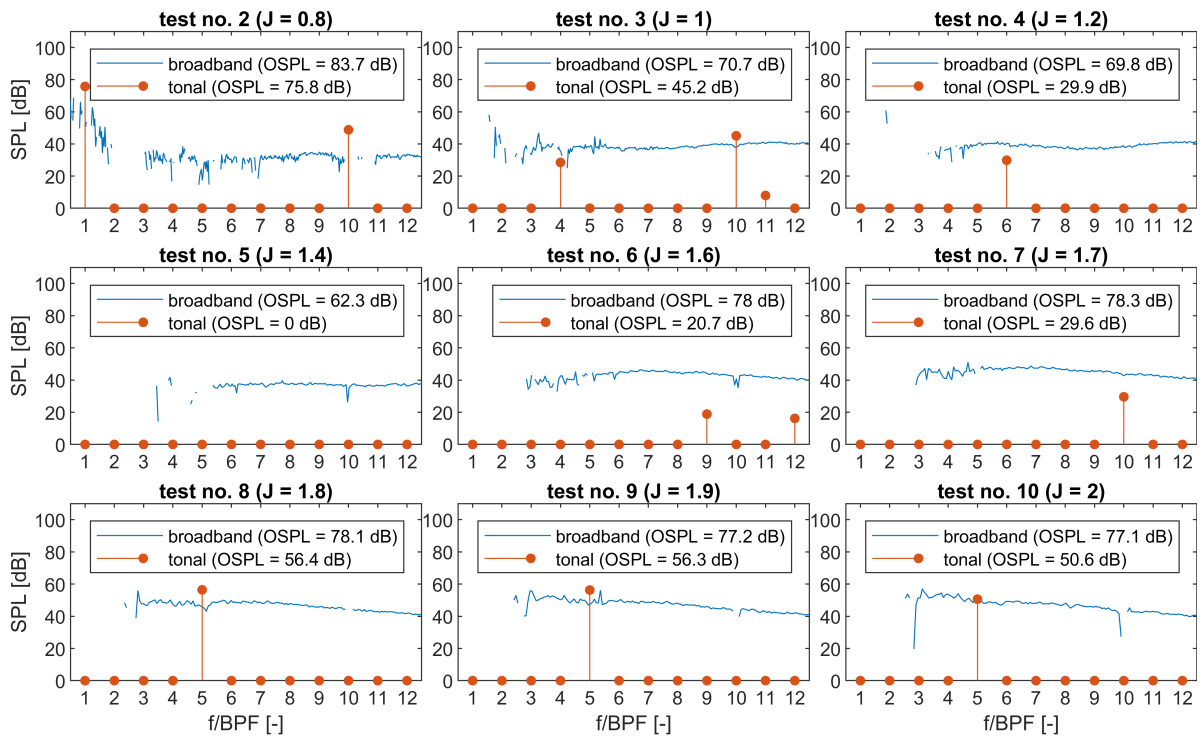
Tonal and Broadband Propeller Noise ($V = 30$ m/s)

Figure C.3: Resulting broadband and tonal propeller noise components after subtraction of wind tunnel noise and motor noise for run 1 ($\Delta f = 16$ Hz).

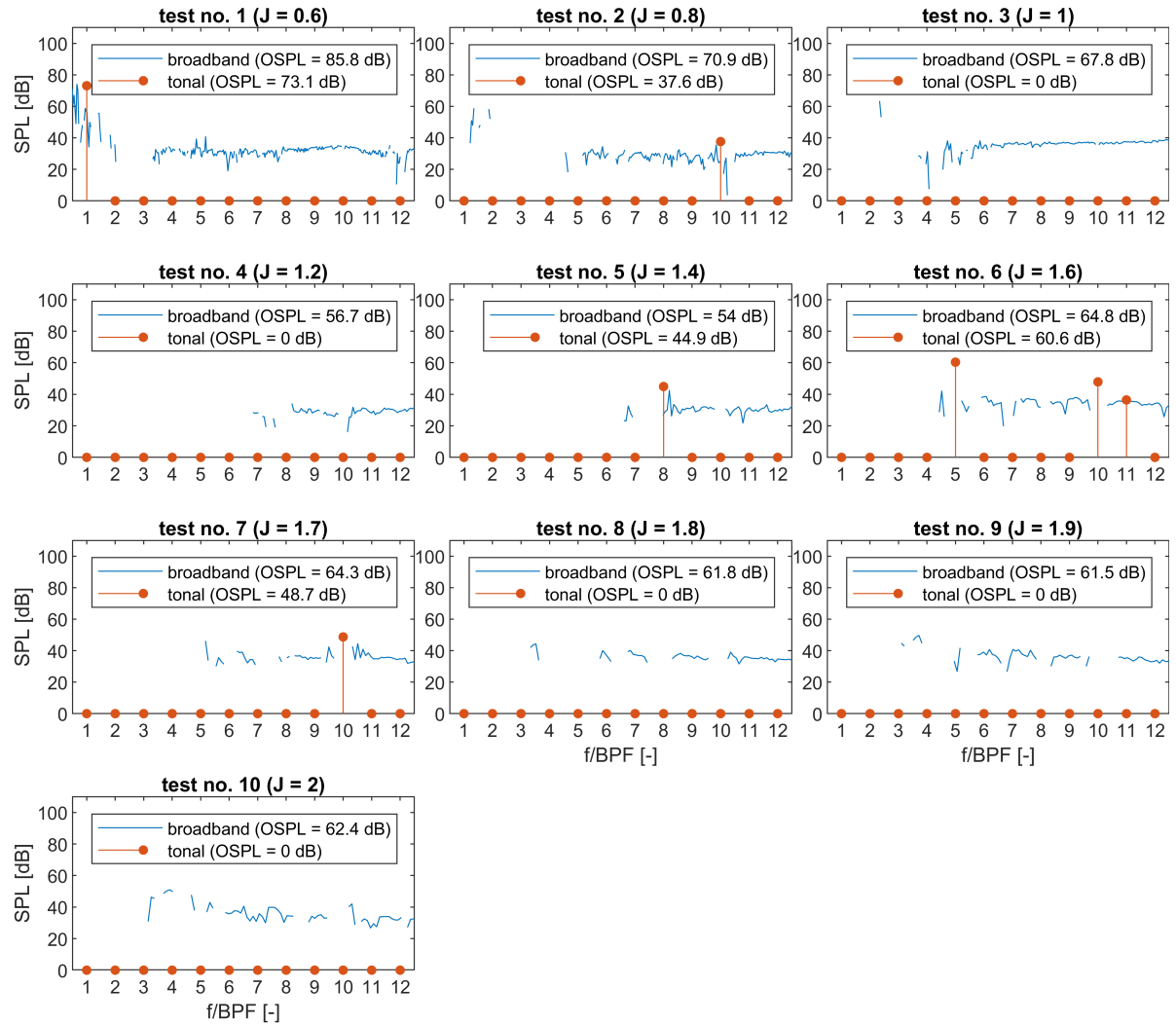
Tonal and Broadband Propeller Noise ($V = 20$ m/s)

Figure C.4: Resulting broadband and tonal propeller noise components after subtraction of wind tunnel noise and motor noise for run 2 ($\Delta f = 16$ Hz).

Figure C.3 Figure C.4 show the broadband spectra and the tonal components at each BPF for $V = 30$ m/s and $V = 20$ m/s. The broadband levels are generally lower for $V = 20$ m/s than $V = 30$ m/s, and less broadband propeller noise was measured, resulting in more gaps in the data. The dominant wind tunnel noise reached higher frequencies. Also, there is fewer data available for the propeller's tonal components. The wind tunnel and motor noise were very dominant. Therefore, there are multiple thrust settings for which no tonal noise could be measured.